UNIVERSITY OF OKLAHOMA

GRADUATE COLLEGE

A BALLOON-BORNE PARTICLE SIZE, IMAGING, AND VELOCITY PROBE FOR IN SITU MICROPHYSICAL MEASUREMENTS

A DISSERTATION

SUBMITTED TO THE GRADUATE FACULTY

in partial fulfillment of the requirements for the

Degree of

DOCTOR OF PHILOSOPHY

By

SEAN MICHAEL WAUGH
Norman, Oklahoma
2016

A BALLOON-BORNE PARTICLE SIZE, IMAGING, AND VELOCITY PROBE FOR IN SITU MICROPHYSICAL MEASUREMENTS

A DISSERTATION APPROVED FOR THE
SCHOOL OF METEOROLOGY

BY

_____
Dr. Michael Biggerstaff, Chair

_____
Dr. Kirsten de Beurs

_____
Dr. Donald MacGorman

_____
Dr. Susan Postawko

_____
Dr. Guifu Zhang

_____
Dr. Conrad Ziegler

© Copyright by SEAN MICHAEL WAUGH 2016
All Rights Reserved.

Acknowledgements

The author would like to take this opportunity to thank Dr. Erik Rasmussen for his involvement and council in this project. While Dr. Rasmussen wrote the core processing code that was used for the data collected, his involvement went so much further than that. Without his patience and assistance in identifying, debugging, and correcting several changes to the core code, the processing steps would not be where they are today. I owe you a great deal more than simple gratitude and an acknowledgement can convey.

I would also like to thank the multitude of students that have helped out with balloon launches over the years. There are too many to name, but their participation, often times at odd hours in less than ideal conditions, is what makes projects like this possible. Without their involvement, launching an instrument of this caliber would be nothing more than a pipe dream.

Dr Kim Elmore, your contribution to this work is also invaluable. Not only did you save me a tremendous amount of stress, you helped me to dig into the statistical importance of several aspects of my analysis and demonstrate how robust my results truly are. This work will be a huge step going forward and you have helped me to solidify the ground work. I cannot thank you enough.

Finally I would like to thank my committee. The guidance and wisdom that you have all conveyed along the way is what makes this process so rewarding. The experience that I have gained throughout this endeavor will serve me for years to come. I appreciate the patience and understanding that you gave me as I worked through this research.

Support for this research was provided by NSF grants AGS 10145102 and AGS-1063945 and by the National Severe Storms Laboratory (NSSL), the latter including federal funding for Rasmussen Systems LLC to develop the Particle Analyzer program. Funding was also provided by NOAA/Office of Oceanic and Atmospheric Research under NOAA-University of Oklahoma Cooperative Agreement #NA11OAR4320072, U.S. Department of Commerce.

Table of Contents

ACKNOWLEDGEMENTS ..... **IV**

TABLE OF CONTENTS ..... **VI**

LIST OF TABLES ..... **X**

LIST OF FIGURES ..... **XI**

ABSTRACT ..... **XXV**

CHAPTER 1 ..... **1**

INTRODUCTION **1**

1.1. MOTIVATION 1

1.2. PREVIOUS WORK 3

CHAPTER 2 ..... **11**

PASIV INSTRUMENT PACKAGE **11**

2.1. OVERVIEW 11

2.2. DESIGN 14

2.2.1. Camera *15*

2.2.2. Parsivel *18*

2.3. OPERATIONAL CONSIDERATIONS 20

CHAPTER 3 ..... **23**

DATA PROCESSING **23**

3.1. CAMERA 23

3.1.1. Particle Analyzer (PA) program in IDL *24*

3.1.2. Overview of the Particle Analyzer algorithm *27*

3.1.3. MTS_PNG algorithm *30*

3.1.4. Brightness algorithms *34*

3.1.5. Post-processing with Matlab *36*

3.2. PARSIVEL 38

3.2.1. Identifying launch *39*

3.2.2. Merging with radiosonde data *40*

CHAPTER 4 42

PARTICLE DATA VALIDATION AND INTEGRATION 42

4.1. SIZING ACCURACY AND CORRECTION 42

4.2. DETECTION ACCURACY AND SAMPLING CORRECTION 45

4.3. COMPUTATION OF THE PARTICLE SIZE COUNT AND PARTICLE SIZE DISTRIBUTION 48

CHAPTER 5 50

COMBINED DATA ANALYSIS 50

5.1. MAIN PROGRAM: PARSIVEL 50

5.2. MAIN PROGRAM: EFM 51

5.3. MAIN PROGRAM: CAMERA 53

5.3.1. Size correction *53*

5.3.2. Particle distribution filter *54*

5.3.3. Particle classification *56*

5.3.3.1. Precipitation particle categories 57

5.3.3.2. Random Forest classification method 61

5.3.3.3. Classification cleanup 65

5.3.4. Precipitation concentration, reflectivity, and mixing ratio *69*

5.3.4.1. Particle size distribution 69

5.3.4.2. Radar reflectivity 72

5.3.4.3. Mixing ratio 73

5.4. MAIN PROGRAM: TRAVERSE 74

CHAPTER 6 77

21 JUNE 2012 – DC3 77

6.1. OVERVIEW 77

6.2. PARSIVEL OBSERVATIONS 79

6.2.1. Total particle size count 79

6.2.2. Particle velocity distribution 81

6.3. CAMERA OBSERVATIONS 89

6.3.1. Total and habit-discriminated particle size count 89

6.3.2 PSD profiles and parametric functional fitting 93

6.3.3. Radar reflectivity comparison 101

6.3.4. Precipitation mixing ratio 107

6.3.5. Particle velocity distribution 109

6.3.6. Electric field profile in the context of observed precipitation 112

6.4 CASE SUMMARY 115

CHAPTER 7 116

29 MAY 2012 – DC3 116

7.1 OVERVIEW 116

7.2. CAMERA OBSERVATIONS 118

7.2.1 Total and habit-discriminated particle size count 118

7.2.2. PSD profiles and parametric functional fitting 121

7.2.3. Radar reflectivity comparison 127

7.2.4. Precipitation mixing ratio 130

7.2.5. Particle velocity distribution 135

7.2.6. Electric field profile in the context of observed microphysics 139

CHAPTER 8 144

INTEGRATION AND DISCUSSION OF FIELD OBSERVATIONS 144

8.1 PARTICLE SIZE DISTRIBUTIONS AND CONCENTRATIONS 144

8.2 RADAR COMPARISONS 148

8.3 BULK MICROPHYSICS COMPARISONS 150

8.3.1. Fitted distribution parameters in the rain region (T > 0 °C).....*150*

8.4 ELECTRIC FIELD PROFILES IN THE CONTEXT OF PRECIPITATION MICROPHYSICS 155

CHAPTER 9 158

CONCLUSIONS.....158

9.1 PRECIPITATION MICROPHYSICS 158

9.2 AMBIENT MICROPHYSICAL PROPERTIES IN STRONGLY ELECTRIFIED STORM ENVIRONMENTS.....160

9.3 RANDOM FOREST TRAINING DATASET 161

9.4 FUTURE WORK 164

REFERENCES 167

APPENDIX: PARTICLE GLOSSARY.....178

A1: RAIN 178

A2: GRAUPEL/HAIL.....182

A3: IRREGULAR ICE CRYSTALS 186

A4: REGULAR ICE CRYSTALS 188

List of Tables

Table 1. Bin diameter, size class spread, and error of the Parsivel disdrometer. 18

Table 2. Output parameters and descriptions from the PA program. 26

Table 3. Parsivel Output Variables, in order 38

Table 4. Classification Metrics 63

Table 5. Contingency table for the random forest classification. Columns are observed while rows are predicted. 64

List of Figures

Figure 1. The configuration of the PArticle Size, Image, and Velocity (PASIV) probe. (a) The light-weight body constructed of residential-grade Styrofoam, with locations indicated for the camera mount, the PARSIVEL box, and the LED batteries; (b) detail of the viewing chamber portion of the PASIV probe, with the locations of the particle intake and deflection fins marked; (c) Viewing chamber seen from above (with LED lights on), where the HD camera is directed into the chamber from the top of the image. The high intensity lights cause the exterior of the chamber in this image to appear black, while the white floor is visible in the center of the image looking through the particle exhaust. The black background panel inside the chamber at bottom of the image increases the contrast of the illuminated precipitation particles in the HD camera images. 12

Figure 2. Image of PASIV launch on 1 August 2013 during DARPA project shows large polyethylene balloon rising with parachute, radiosonde, and PASIV trailing behind. Several crew members are required to assist in holding the instrument train prior to launch. 13

Figure 3. Sample particle images (cropped) from the videosonde instrument in the PASIV probe. (a) raindrop; (b) lump graupel particle; (c) snow assemblage. The Particle Analyzer program determines particle sizes in post-analysis as described in the text. The derived major axis lengths are 4.5 mm (raindrop), 6.2 mm (lump graupel), and 6.7 mm (snow assemblage) respectively. All particles are falling from left to right, with the

illumination sources at the top and bottom of each image. The bright lobes in the raindrop image in panel (a) are internal refractions of the left and right LED arrays. ... 17

Figure 4. Parsivel disdrometer housing as adapted for PASIV. Panel (a) shows an open view of the interior circuits and laser assembly, while panel (b) shows the complete unit with covers attached. The dimensions of the reconfigured Parsivel disdrometer unit are 50.8 x 17.8 x 3.8 cm. 20

Figure 5. Output graphical user interface (GUI) of the PA program used to peruse and analyze camera image data from the PASIV. The upper panel (red outline) shows the image area and detected particle(s) for that image. The lower-left panel (green outline) is the image selection box that manages which images are analyzed. The lower-right panel is the histogram area that displays the distributions of the output statistics. 24

Figure 6. PA detection image. White pixels are associated with the identified object, while the red ellipse around the object shows the PA code's fit to the particle from which the measurements of size and shape are based. 25

Figure 7. PA program window showing control panel options for processing algorithm 28

Figure 8. Processing figure of GPS altitude (m) vs time (s) for identifying launch in the radiosonde data for the PASIV. Data from June 21st, 2012 case shown, launch was at 3654 seconds. Data points along the top of the figure are missing data values from the sonde. 37

Figure 9. Parsivel processing plot for identifying launch time. Left shows signal amplitude, middle shows battery voltage, and right shows the number of detected particles per time step. The launch record is identified by the small downward spike in the signal amplitude near 350 s. 40

Figure 10. Processing figure for identifying launch in the radiosonde data. Top is GPS altitude (m) bottom is vertical velocity (m s^{-1}). A combination of increasing altitude and sudden positive vertical motions indicates launch. This figure shows data from June 21st, 2012, launch was approximately 3600 seconds. 41

Figure 11. Sample camera-imaged (left column) and analyzed (right column) images of test particles with known size and physical characteristics. The upper panels (a) correspond to a 4.76 mm acrylic test sphere (upper-left panel) to simulate rain, while the lower panels (b) correspond to a 3 mm opaque white delrin test sphere (lower-left panel) to simulate graupel. The PA-analyzed particles (right-column) are indicated by contiguous white pixels, while the background is masked with black pixels. The fitted elliptical outlines of the test spheres are depicted by the red curves. 42

Figure 12. Summary of sizing test conducted on the camera and Parsivel sensor components of the PASIV. The one-to-one line (light gray) and power-law regression line for the Parsivel steel (blue) and Camera steel (green) are also shown. The Delrin spheres are not shown but showed similar offsets as the acrylic spheres. 43

Figure 13. Detection efficiency (100 x ε, %) derived from Eq. (2) in the text (blue line), scaled by 100 (e.g. efficiency in percent), and assuming a 5 mm particle diameter. The red line is an experimentally determined curve by dropping 500, 5 mm steel ball

bearings repeatedly from varying heights. The relative velocity is the particle velocity with respect to the PASIV frame of reference. 47

Figure 14. Plot of the vertical component of the vector electric field vs pressure. Values are averaged at a 60 second interval to reduce noise. 53

Figure 15. Example image of clustered ice crystals (bottom) and the PA grouped object (top). The clustered object measured 1.32 mm (non-corrected) and had a maximum irregularity of 102.6 54

Figure 16. Example of an edge detection. Raw image (bottom) shows a small ice crystal while the PA detection (top) shows the fitted ellipse which touches the edge. The bottom of the ellipse has a sharp line marking the image edge. 56

Figure 17. Example image of a raindrop, 6.7 mm equivalent diameter. Particle was observed in the May 29th, 2012 case. 57

Figure 18. Example image of a conical graupel particle, 1.45 mm equivalent spherical diameter. Particle was observed in the May 29th, 2012 case. 58

Figure 19. Example image of an irregular ice crystal, 6.73 mm equivalent spherical diameter. Particle was observed in the June 21st, 2012 case. 60

Figure 20. Example image of regular ice crystals. Particles were observed in the June 21st, 2012 case. 60

Figure 21. Brightness histogram for a raindrop (left) and a graupel (right) particle. Both particles taken from the May 29th, 2012 case. The raindrop shows a single peak

structure (graph type 0) while the graupel particle has a double peak structure (graph type 1). 63

Figure 22. PASIV sounding at 1704 UTC on 21 June 2012. 77

Figure 23. KTLX radar base scan (0.5 deg elevation) at 1703 UTC during the 21 June 2012 DC3 weak pulse storm case. The radar data is displayed using the Gibson Ridge (GR) Level 2 Analyst program. The approximate launch location of the PASIV at the time of the radar scan is marked by a red dot. 78

Figure 24. Histograms of total particle size count (PSC) versus height on 21 June 2012 using the Parsivel data. Large tail in the distribution occurs near 8 km, with a secondary maximum near 5 km. The melting layer (0°C isotherm) is indicated by a heavy red line. Color indicates the number of particles (on a logarithmic scale) per size bin, for 10 s layers. 79

Figure 25. In-storm sounding for 21 June 2012 as recorded from the PASIV flight. Air temperature (red) and dew point (blue) are shown. Profile indicates a nearly saturated environment for most of the profile. 80

Figure 26. Parsivel measured velocities for the rain layer (sfc - 4km) in 21 June 2012. The color filled scale depicts the number of particles in a given size-velocity bin on a log scale. Also shown are theoretical relations from Beard (1977) and Gunn & Kinzer (1949) that have been adjusted upwards according to the assumed rise rate of 4 m/s. .. 82

Figure 27. Measured Parsivel velocities for the 7-8 km ice layer with multiple velocity relations adjusted for the assumed balloon ascent rate (4 m/s). The color filled scale depicts the number of particles in a given size-velocity bin on a log scale..... 85

Figure 28. Measured Parsivel velocities for the 9-10 km ice layer with multiple velocity relations adjusted for the assumed balloon ascent rate (4 m/s). The color filled scale depicts the number of particles in a given size-velocity bin on a log scale..... 87

Figure 29. Measured Parsivel velocities for the 8-9 km ice layer with multiple velocity relations adjusted for the assumed balloon ascent rate (4 m/s). The color filled scale depicts the number of particles in a given size-velocity bin on a log scale..... 87

Figure 30. Measured Parsivel velocities for the 10-12 km ice layer with multiple velocity relations adjusted for the assumed balloon ascent rate (4 m/s). The color filled scale depicts the number of particles in a given size-velocity bin on a log scale..... 88

Figure 31. Histograms of total particle size count (PSC) versus height from the camera on 21 June 2012. Color fill indicates particle counts (on a logarithmic scale), per size bin, per analysis layer (50 m). The melting layer (0°C isotherm) indicated by heavy red line. 89

Figure 32. Histograms of individual particle size count (PSC) from the camera on 21 June 2012 showing particle size distribution as a function of altitude, temperature, and pressure according to particle type (rain, graupel, irregular, and regular). Color fill shows number of detected particles, per size bin, per analysis layer (50 m). 92

Figure 33. Individual particle size distributions (PSDs) from the camera on 21 June 2012 as a function of altitude, temperature, and pressure according to particle type (rain, graupel, irregular, and regular). Color fill indicates concentration (m^{-3} mm^{-1}) in each 50 m deep analysis layer..... 93

Figure 34. PSD over an approximately 500 m deep layer centered on 0.45 km from 21 June. The distribution shows the total particle concentration in each size bin for all particles (black), rain (dark blue), irregular ice (green), graupel (light blue), and regular ice (red). Also shown are the fitted distributions for the MP (dashed line), exponential (dotted line), and gamma (magenta line) functions. A 95% confidence interval is indicated for the total DSD..... 94

Figure 35. PSD over an approximately 500 m deep layer centered on 4.6 km from 21 June. The distribution shows the total particle concentration in each size bin for all particles (black), rain (dark blue), irregular ice (green), graupel (light blue), and regular ice (red). Also shown are the fitted distributions for the MP (dashed line), exponential (dotted line), and gamma (magenta line) functions. A 95% confidence interval is indicated for the total DSD..... 97

Figure 36. PSD over an approximately 500 m deep layer centered on 8.25 km from 21 June. The distribution shows the total particle concentration in each size bin for all particles (black), rain (dark blue), irregular ice (green), graupel (light blue), and regular ice (red). Also shown are the fitted distributions for the MP (dashed line), exponential (dotted line), and gamma (magenta line) functions. A 95% confidence interval is indicated for the total DSD..... 98

Figure 37. Calculated parameters for the gamma (blue), exponential (red), and MP (yellow) functional fits across 500 m deep layers throughout the 21 June sounding. Parameters were found using the MoM technique. 99

Figure 38. Individual particle size distributions (PSDs) from the camera for each particle type on 21 June 2012 versus altitude, temperature, and pressure as calculated in 500 m deep analysis layers. 101

Figure 39. Histograms of individual particle size count (PSC) from the camera for each particle type on 21 June 2012 versus altitude, temperature, and pressure as calculated in 500 m deep analysis layers. 102

Figure 40. PSDs (m^{-3} mm^{-1}) on 21 June for each particle type with calculated and observed radar reflectivity overlaid. Color fill indicates particle concentration (log scale, m^{-3} mm^{-1}). The orange line indicates the observed radar reflectivity from SR2 during DC3, while the heavy black line is the calculated total reflectivity from the sum of the individual reflectivities of the measured PSDs. The various colored lines in each subplot indicate the reflectivity from that particle classification. Left – rain, left center – graupel, right center – irregular, right – regular. 104

Figure 41. Calculated radar reflectivity from the measured particle distribution on 21 June 2012 showing reflectivity variations due to particle density for the different particle types. Red - regular crystals, green - irregular crystals, light blue - graupel, dark blue – rain. 106

Figure 42. Particle mixing ratios for 21 June 2012 by as a function of altitude. Mixing ratios are shown as dark blue for rain, cyan for graupel, green for irregular ice, red for regular ice, and light blue for combined snow. Analysis was done for 500 m integration layers..... 108

Figure 43. Camera size distribution and calculated velocities for the rain layer (sfc - 4km) in 21 June 2012. The color filled scale depicts the number of particle in a given size-velocity bin on a log scale. Also shown are theoretical relations from Beard (1977) and Gunn & Kinzer (1949) that have been adjusted upwards according to the assumed rise rate of 4 m/s. Velocity was calculated using Gunn & Kinzer (1949)..... 110

Figure 44. Camera size distribution and calculated velocities for the 8-9 km ice layer with multiple velocity relations adjusted for the assumed balloon ascent rate (4 m/s). The color filled scale depicts the number of particle in a given size-velocity bin on a log scale. Regular crystal velocity was calculated using the "P1e" relation, while irregular crystal velocity was calculated using the "Agg_{Du}" relation..... 111

Figure 45. Total electric field profile for 21 June 2012, broken down in to x (red dots), y (blue dots) and z (black dots) components. 113

Figure 46. Camera data from 21 June 2012 showing particle concentration as a function of altitude, temperature, and pressure according to particle type (rain - left, graupel – left middle, irregular – right middle, and crystal - right) with charge density (C/m^3) overlaid. Color fill shows number of detected particles, per size bin, per analysis layer (50 m). Charge density (red line) shown on second axis. 114

Figure 47. Mobile environmental storm-following sounding at 0020 UTC on 30 May 2012 during the DC3 field campaign operations. Sounding was taken from a NSSL mobile sounding unit in the far field environment of the severe weather outbreak. 116

Figure 48. Triple-Doppler analysis at 0.2 km AGL and 2324 UTC for the 29 May 2012. Reflectivity (dBZ) is color-filled while synthesized horizontal wind vectors are scaled to 1 km = 20 m s^{-1}. The launch site at 2323 for the PASIV is indicated by the NS3 location. 117

Figure 49. Histograms of total particle size count (PSC) versus height from the camera on 29 May 2012. Color fill indicates particle counts (on a logarithmic scale), per size bin, per analysis layer (50 m). The melting layer (0°C isotherm) is indicated by heavy red line. 119

Figure 50. Histograms of individual particle size count (PSC) from the camera on 29 May 2012 as a function of altitude, temperature, and pressure according to particle type (rain, graupel, irregular, and regular). Color fill shows number of detected particles, per size bin, per analysis layer (50 m). 120

Figure 51. Hailstone observed in the PASIV on 29 May 2012. Diameter was 18.1 mm and the air temperature was 15.5°C..... 121

Figure 52. PSD over an approximately 500 m deep layer centered on 2.5 km from 29 May. The distribution shows the total particle concentration in each size bin for all particles (black), rain (dark blue), irregular ice (green), graupel (light blue), and regular ice (red). Also shown are the fitted distributions for the MP (dashed line), exponential

(dotted line), and gamma (magenta line) functions. A 95% confidence interval is indicated for the total DSD. 122

Figure 53. PSD over an approximately 500 m deep layer centered on 5.75 km from 29 May. The distribution shows the total particle concentration in each size bin for all particles (black), rain (dark blue), irregular ice (green), graupel (light blue), and regular ice (red). Also shown are the fitted distributions for the MP (dashed line), exponential (dotted line), and gamma (magenta line) functions. A 95% confidence interval is indicated for the total DSD. 123

Figure 54. PSD over an approximately 500 m deep layer centered on 6.6 km from 29 May. The distribution shows the total particle concentration in each size bin for all particles (black), rain (dark blue), irregular ice (green), graupel (light blue), and regular ice (red). Also shown are the fitted distributions for the MP (dashed line), exponential (dotted line), and gamma (magenta line) functions. A 95% confidence interval is indicated for the total DSD. .....**Error! Bookmark not defined.**

Figure 54. PSD over an approximately 500 m deep layer centered on 6.6 km from 29 May. The distribution shows the total particle concentration in each size bin for all particles (black), rain (dark blue), irregular ice (green), graupel (light blue), and regular ice (red). Also shown are the fitted distributions for the MP (dashed line), exponential (dotted line), and gamma (magenta line) functions. A 95% confidence interval is indicated for the total DSD. 125

Figure 55. Calculated parameters for the gamma (blue), exponential (red), and MP (yellow) functional fits across 500 m deep layers throughout the 29 May sounding. Parameters were found using the MoM technique. 126

Figure 56. 29 May particle concentrations versus altitude per particle type with calculated and observed radar reflectivity overlaid. Color fill indicates # m^{-3} mm^{-1} per analysis layer (500 m). The orange line indicates the observed radar reflectivity from the triple-Doppler analysis, while the heavy black line is the calculated reflectivity from the measured PSD. The various colored lines in each subplot indicate the reflectivity from that particle classification. Left – rain, left center – graupel, right center – irregular, right – regular. 128

Figure 57. Calculated radar reflectivity from the measured particle distribution on 29 May 2012 showing reflectivity variations due to particle density for the different particle types. Red - regular crystals, green - irregular crystals, light blue - graupel, dark blue – rain. 129

Figure 58. Particle mixing ratios for 29 May 2012 by type (rain - left, graupel/hail - middle, snow - right) as a function of altitude. The orange line in each subplot shows the retrieved mixing ratio for that particle type from the DLA. The PASIV mixing ratios are shown as dark blue for rain, cyan for graupel, green for irregular ice, red for regular ice, and light blue for combined snow. Analysis was done for 500 m integration layers. 132

Figure 59. Camera size distribution and calculated velocities for the rain layer (sfc - 4km) in 29 May 2012. The color filled scale depicts the number of particles in a given

size-velocity bin on a log scale. Also shown are theoretical relations from Beard (1977) , Gunn & Kinzer (1949), and Heymsfield and Wright (2014). The latter two have been adjusted upwards according to the assumed rise rate of 4 m s^{-1}. Velocity was calculated using Gunn & Kinzer (1949) for rain and Heymsfield and Wright (2014) for hail. The large hailstone depicted in Figure 51 is denoted with a star. 137

Figure 60. Camera size distribution and calculated velocities for the ice layer above 5 km on 29 May 2012 with multiple velocity relations adjusted for the assumed balloon ascent rate (4 m/s). The color filled scale depicts the number of particles in a given size-velocity bin on a log scale. Regular crystal velocity was calculated using the "P1e" relation, irregular crystal velocity was calculated using the "Agg_{Du}" relation, and graupel was calculated using the 300 kg/m^3 Bohm (1989). 138

Figure 61. Total electric field profile for 29 May 2012, broken down in to x (red dots), y (blue dots) and z (black dots) components. 139

Figure 62. Camera data from 29 May 2012 showing particle concentration as a function of altitude, temperature, and pressure according to particle type (rain -left, graupel – left middle, irregular –right middle, and crystal - right) with charge density (C/m^3) overlaid. Color fill shows number of detected particles, per size bin, per analysis layer (50 m). Charge density (red line) shown on second axis. 140

Figure 63. DLA at 5.7 km AGL and 2342 UTC for 29 May. Color fill shows cloud water mixing ratio (g kg^{-1}), synthesized wind vectors are scaled to 1 km = 20 m s^{-1}, and contours indicate vertical veloctiy at 5 m s^{-1}. Updrafts are solid, downdrafts are dashed. Balloon location at 23:41 UTC and 5.75 km indicated. 141

Figure 64. DLA at 6.7 km AGL and 2345 UTC for 29 May. Color fill shows cloud water mixing ratio (g kg^{-1}), synthesized wind vectors are scaled to 1 km = 20 m s^{-1}, and contours indicate vertical veloctiy at 5 m s^{-1}. Updrafts are solid, downdrafts are dashed. Balloon location at 23:41 UTC and 6.6 km indicated. 142

Figure 65. Triple-Doppler analysis at 8.7 km AGL and 2348 UTC for 29 May. Color fill shows cloud water mixing ratio (g kg^{-1}), synthesized wind vectors are scaled to 1 km = 20 m s^{-1}, and contours indicate vertical veloctiy at 5 m s^{-1}. Updrafts are solid, downdrafts are dashed. Black dotted line indicates cross section 146

Figure 66. Triple-Doppler analysis 2348 UTC for 29 May. Cross section indicated in Figure 65. Color fill shows cloud water mixing ratio (g kg^{-1}), synthesized wind vectors are scaled to 1 km = 20 m s^{-1}, and contours indicate vertical veloctiy at 5 m s^{-1}. Updrafts are solid, downdrafts are dashed. Balloon location at 2348 UTC marked. 147

Figure 67. Distribution plot showing the population data (1) and the training data (2) for each of the predictor variables listed in Table 4 (excluding the binary graph type predictor). Each box represents the 25th and 75th percentile of the distribution, while the whiskers extend to +/-2.7 standard deviations. 162

Figure 68. Peirce Skill Scores for the random forest classifications of rain (dark blue), irregular (red), graupel (green), and regular (cyan) particles. The 95% confidence interval of each skill score is shown, and the figure is zoomed to show these limits. . 164

Abstract

A balloon-borne instrument known as the PArticle Size, Image, and Velocity (PASIV) probe has been developed at the National Severe Storms Laboratory to provide in situ microphysical measurements in storms. These observations represent a critical need of microphysical observations for use in lightning studies, cloud microphysics simulations, and dual-polarization radar validation. The instrument weighs approximately 2.72 kg and consists of an HD video camera, a camera viewing chamber, and a modified Parsivel laser disdrometer mounted above the camera viewing chamber. Precipitation particles fall through the Parsivel sampling area and then into the camera viewing chamber, effectively allowing both devices to sample the same particle stream. The data are collected onboard for analysis after retrieval. Taken together, these two instruments are capable of providing a vertical profile of the size, shape, velocity, orientation, and composition of particles along the balloon path within severe weather.

The PASIV probe has been deployed across several types of weather environments including thunderstorms, supercells, and winter storms. Initial results from two cases in the Deep Convective Clouds and Chemistry Experiment are shown that demonstrate the ability of the instrument to obtain high temporal and spatial resolution observations of the particle size distributions (PSD) within convection. The ability to resolve the PSD into different particle habits and compare to observed radar and model analysis values is also demonstrated.

Chapter 1

Introduction

In situ microphysics are a key source of storm data, but are difficult to obtain. With potential applications to dual-polarization radar validation, the dynamics and microphysics of storms, cloud modeling, and lightning research, it is important that measurements accurately represent a wide range of spatially- and temporally-varying internal storm conditions. In fact, several of these areas have unique challenges that have made validation and advancement difficult, providing motivation for this study.

1.1. Motivation

With the advancement of the polarimetric upgrade of the Weather Surveillance Radar-1988 Doppler (WSR-88D) Network, extensive use of a hydrometeor classification algorithm (HCA; Straka et al. 2000; Park et al. 2009) and a melting layer detection algorithm (MLDA; Giangrande, et al. 2008) have become increasingly useful. The HCA and MLDA serve to distinguish between various particle types using a fuzzy logic approach based on polarimetric radar variables. While the approaches work reasonably well for warm-season deep moist convection, their evaluations suffer from a lack of validating observations. Heinselman and Ryzhkov (2006) reported on the validation of hail detection by the NWS operational HCA during the Joint Polarimetric Experiment, but observations of particle types other than hail at ground level are more difficult to obtain. It should be noted that, although the operational HCA was designed to be used for warm season convection, it is typically applied year-round in all seasons. The temptation to apply the operational HCA for winter precipitation events is high,

although the operational HCA has been shown to exhibit statistically insignificant skill in distinguishing frozen hydrometeors at the surface (Elmore 2011). Thompson et al. (2014) expanded on the operational HCA to make it more applicable to winter precipitation events, but still required the use of external temperature information to function. Validation of the HCA classifications is needed, but is difficult to obtain due to the location of the observations within convection. Limited in situ observations have been made to validate HCAs (Kouketsu et al. 2015). Surface and aircraft observations can provide some estimates, but more direct observations of particle types and locations are still lacking.

In addition to HCA validation, microphysics observations are particularly useful to lightning and charge generation studies. It is generally accepted that the non-inductive charging mechanism is the major contributor to storm electrification through the collision of graupel and ice in the presence of supercooled water (Takahashi 1978; Saunders and Peck 1998; Saunders 2008; Emersic and Saunders 2010; Reinhart et al. 2014). While this mechanism is reasonably well understood, the locations of these particles can currently only be inferred from polarimetric radar observations or limited aircraft data. Having more in situ observations of particle types and their locations within convective storms would add significantly to the understanding of charge generation and lightning production.

Given the lack of observations, modeling studies of processes such as cloud electrification have proven useful (Mansell et al. 2010). Doing so however requires the use of microphysical parameterization schemes to represent modeled cloud and precipitation particles. Bin microphysical schemes are physically very detailed, but are

computationally expensive (Johnson et al. 2016). The more commonly used alternative bulk microphysics schemes simplify the microphysics via single, double, or triple moment prediction equation approximations of microphysical processes that act to form the various hydrometeor size distributions. One-moment schemes predict hydrometeor mixing ratio, while two-moment schemes additionally predict number concentration. Three-moment schemes move one step further by predicting concentration, mixing ratio, and radar reflectivity (Milbrandt and Yau, 2005).

While there has been recent focus on the improvements resulting from using higher-moment schemes over the simpler one-moment schemes, questions remain regarding which schemes are more representative (Morrison et al. 2009; Morrison and Milbrandt 2011; Weverberg et al. 2012; Johnson et al. 2016). Specifically, many of these studies have found that how individual schemes represent graupel and hail can have a major impact on simulated airflow through impacts on total buoyancy from diabatic heating and cooling and precipitation loading. These in turn impact the overall production of cloud and precipitation. Given the sensitivity of cloud models to these parameterizations, it is imperative that a scheme which accurately represents the true in-storm microphysical state be chosen. However, direct observations of microphysics in key portions of deep convective storms are severely lacking. Additional in situ observations are needed to determine which model microphysics schemes are able to realistically predict actual hydrometeor distributions of various particle types.

1.2. Previous Work

Given the need for in situ microphysics observations, the simplest approach is to examine surface observations. As an example, surface disdrometers such as the Parsivel

(Loffler-Mang and Joss 2000; Friedrich et al. 2013; Yuter et al. 2006; Loffler-Mang and Blahak 2001) and the 2D Video disdrometer (2DVD) (Schuur et al. 2001; Cao et al. 2008, 2010) have been used to examine the drop size distribution (DSD) in precipitation.

Although these observations provide valuable comparisons to radar data, they also suffer somewhat from a separation of sampling volumes in which the radar provides a volumetric estimate at altitude while the disdrometer provides a fixed-point measurement at the surface. Comparisons between these two observations are complicated as large changes in DSDs can occur between the two altitudes of measurements. Advection, evaporation, sedimentation with accompanying size sorting, various microphysical processes (e.g., collision, coalescence, shedding, and breakup) and sampling differences may all or individually act to modify the DSD that the radar sees before reaching the surface (Schuur et al. 2001; Kalina et al. 2014). In general, because the exposed area of surface disdrometers is small, they may somewhat incompletely sample the local instantaneous particle size distribution (PSD) or "particle spectrum" (i.e., where PSD or alternatively “particle spectrum” is defined by the number of particles per unit volume per unit size interval, and "DSD" is the rain drop PSD or drop spectrum) and the precipitation rate of either rain (Schuur et al. 2001) or snow (Battalgia et al. 2010). With this knowledge in mind, several assumptions about spatio-temporal homogeneity and evaporation must be made prior to using these data (Schuur et al. 2001). While useful, this limits the applicability of the comparison and a more efficient approach would be to compare estimates of the DSD within the same volume.

To obtain a more direct comparison between radar observations and measured DSDs, the particle samples must be obtained within the radar volume itself at altitude. This requires that the measurement device be mounted on a mobile platform that is capable of penetrating into potentially deep convective storm environments. The most conventional approach to this problem is through the use of instrumented storm penetration aircraft (SPA). Many previous projects with access to SPAs have employed wing-mounted particle probes such as the Particle Measuring Systems (PMS) Optical Array Probe (2D-OAP) models 2D-C and 2D-P and the PMS Forward Scattering Spectrometer Probe (FSSP). These in situ hydrometeor measurement sensors have been used extensively in a variety of projects to collect microphysics measurements at altitude in various types of deep convection and convective systems (e.g., Musil et al. 1973; Heymsfield 1978; Heymsfield et al. 1978; Heymsfield and Musil 1982; Jorgensen and Willis 1982; Musil et al. 1986; Heymsfield et al. 2004; McFarquhar et al. 2007; Smith et al. 2009; Heymsfield et al. 2013). This data collection strategy has the advantage of being able to take PSD measurements over large areas; although a degree of spatial homogeneity must be assumed to interpret the large samples that are normally required to obtain statistically representative data sets. Particle shattering and flow trajectories caused by the aircraft itself can cause errors in the measured PSD (Norment 1988). Additionally, ceiling limits on altitude and safety factors often prevent aircraft from sampling certain areas of storms (including hail, strong vertical velocity cores and shear zones, proximity to lightning, or active icing zones).

Given the limitations of aircraft observations, not the least of which is being able to make measurements in conditions considered too hostile for aircraft, an alternative

approach to in situ particle measurements is warranted. To address these issues and provide a relatively inexpensive, light-weight instrument for collecting in situ particle data, balloon-borne devices known as "videosondes" and other microphysics probes have been developed. Such balloon-borne instruments can be flown in a variety of conditions, including those generally too hostile or unreachable by more conventional measurement platforms (e.g., via surface instruments or aircraft). Miloshevich and Heymsfield (1997) used a Formvar replicator on a balloon-borne device to measure ice crystal habits and structures of particles smaller than 100 µm. Others have used video cameras to observe precipitation particles (e.g. Murakami et al. 1987, hereafter referred to as M87 and Takahashi 1990, hereafter referred to as T90) inside convection and retrieve PSD information from the video images.

The M87 videosonde utilizes a film strip to physically record the impressions of impacting particles between 7 µm and 2 cm. The film strip is then imaged with a non-HD camera, and the recording is transmitted to a ground station using a 1.6 GHz microwave antenna link. M87 have carefully documented the particle sampling efficiency of their videosondes, which varies from about 0.12 to 0.77 as a function of increasing particle diameter.

The T90 videosonde is similar to the M87 instrument, in that it uses a film strip to capture the sizes of smaller particles whose imprints are then imaged by a camera. However for particles larger than 0.5 mm diameter, a flash is triggered that illuminates the particle for direct video capture from a second camera. These flashes occur at a rate less than 2 Hz due to the lag time required to recharge the strobe lamp. As with the M87 videosonde, the T90 videosonde is not recovered since it likely lands in the nearby

ocean. Hence, the non-HD images from the T90 videosonde are also transmitted to a ground receiving station for processing. Due to the limitations of the transmitter, the T90 videosonde is only capable of transmitting one type of image at a time. This requires a choice be made between the illuminated image of particles larger than 0.5 mm in diameter, and the film strip image. While preference is given to the larger particle image, this would affect any concentrations that were calculated from the observed particles.

Boussaton et al. (2004, hereafter referred to as B04) have expanded videosonde capabilities using a camera-based system similar to M87 and T90 combined with particle charge measurements (which was also added to the T90 videosonde later, see Takahashi 2010). The B04 videosonde measures particle diameter from 0.5 mm to 2 cm and includes an induction ring to measure particle charge in the range of +/- 1 to 400 pC. As an alternative to direct video imaging of particles, B04 employ a shadowing technique to determine particle size. Two lights near the camera illuminate each particle, which cast two shadows on the back plane toward either side of the object. Knowing the distance between the induced shadows on the back plane, the distance of each particle from the camera and thus its original size can be determined. The B04 videosonde design assumes that all images contain a single particle to uniquely relate particle charge to size, a valid approximation given their small sampling volume and balloon ascent rate. The shutter speed of the camera used for particle capture is not fixed, and varies with illumination. As with the M87 and T90 videosondes, the image data is transmitted to the ground since the instrument is lost after launch.

A different approach to measuring PSDs on a balloon-borne device was utilized by Mahlke et al. (2008) via their development of the so-called "Flying Parsivel". The authors modified the standard Parsivel disdrometer unit as created by Loffler-Mang and Joss (2000) to fit within a balloon-borne package. The Parsivel device is capable of measuring particle size and velocity through the use of a laser diode (more details in 2.2.2. Parsivel). One advantage of the Parsivel system, aside from the size and velocity measurements, is the fast scanning rate of the laser which allows the unit to sample a large number of particles in a short amount of time. The Parsivel system thus possibly allows the measurement of nearly every particle that passes through the sensing area at typical precipitation rates.

Although the M87, T90, and B04 videosondes and the "Flying Parsivel" have pioneered a novel approach for collecting unique in situ particle data at altitude, they all suffer from a number of operational drawbacks. The large cost associated with the fabrication of the videosondes can be prohibitive in more extensive field campaigns since each instrument is lost after launch. Additionally, because the instrument is lost the data must be transmitted to the ground via a radio link. This requirement reduces the quality of the data transmitted, as it is difficult to attain the large required bandwidths to move large quantities of data quickly over a radio link. Thus lower resolution images are used, and a slower frame rate is required to be able to complete the transmission between frames, both of which in turn reduce the sensitivity of the instrument.

A drawback of the "Flying Parsivel" system is that the laser cannot determine either particle habit or its possible departures from the assumed spherical drop form

(e.g. Battaglia et al. 2010). For example, highly elliptical ice particles that fall through the horizontal laser beam at an angle could potentially account for variable and possibly large biases of inferred particle size and velocity (Battaglia et al. 2010). Hence, Parsivel measurement errors may be introduced via the required simplifying assumptions regarding the particle size, velocity, and habit. Mahlke et al. (2008) assumed that all particles were rain drops, which in turn leads to large discrepancies between the radar reflectivity as calculated from the measured DSD and that measured by radar when ice was present. Furthermore, Mahlke et al. (2008) did not account for the balloon rise rate with respect to still air in their displayed results, leading to some uncertainty in their conclusions.

Advances in technology during roughly the past decade have made it possible to develop an improved balloon-borne videosonde. Light-weight, high-definition (HD) commercially available video cameras now record their data on small flash drives and provide high-resolution imagery. Furthermore, the availability of low cost, low power, light-weight GPS tracking technology greatly increases the feasibility of retrieving deployed instruments, at least in operations over land. The retrieval and reuse of instruments lowers the per-mission cost even if the individual instruments are somewhat more expensive, in turn making multiple flights in a field program more affordable. However, the greatest benefit of retrieving instruments is that it allows much more data to be recorded on board than could be readily transmitted during balloon flights. Thus, video can be recorded with much improved temporal and spatial (pixel) resolution.

The progression of balloon-borne precipitation particle sensing technology has helped provide a basis to develop an updated videosonde that provides more detailed

particle measurements at altitude in deep convective storm precipitation and for a lower cost. The present dissertation reports the development, testing, and utilization of a retrievable, multisensor HD-camera-Parsivel hybrid, balloon-borne instrument which is known as the National Severe Storms Laboratory (NSSL) PArticle Size, Image, and Velocity (PASIV) probe. The primary objectives of developing the balloon-borne PASIV probe are to obtain detailed storm observations of liquid and ice precipitation particle sizes and concentrations, determine particle habits, and estimate the PSDs in storms.

Chapters 2-5 will focus on the instrument itself, detailing not only the physical design of the instrument, but also the processing steps required to quality-control and process the recorded data to produce reliable measurements for scientific analysis of storm microphysics. Chapters 6 and 7 will then discuss specific applications of the PASIV instrument by analyzing two deployments of the instrument during the Deep Convective Clouds and Chemistry (DC3) experiment. Chapter 8 will tie these observations together through comparisons of the distinctly different environments sampled, while Chapter 9 will review the methods, results, and conclusions and provide some direction for the plans for improving and applying this instrument for ongoing storm microphysics research. Finally, an Appendix provides extensive examples and documentation of various particle habits and sizes that were encountered throughout the reported observations (Appendix: Particle Glossary).

Chapter 2

PASIV Instrument Package

2.1. Overview

To obtain in situ microphysics measurements in storms, a balloon-borne instrument known as the PASIV probe has been developed at NSSL following the work of Boussaton et al. (2004), Murakami and Matsuo (1990), Murakami et al. (1987), and Takahashi (2010). The United States Federal Aviation Administration (FAA) regulation Part 101 requires that a free-flying balloon package weigh no more than 2.72 kg. It also states that the entire instrument train cannot weigh more than 5.44 kg, with no single instrument weighing more than 1.81 kg with a weight-to-area ratio of 85.05 g per 6.45 cm^2 on any side of the instrument.

To comply with these regulations, the main support structure of the PASIV is composed of parts made from residential grade R-4 extruded sheet Styrofoam and assembled by hand with a combination of Monokote film, packing tape, and glue. This lightweight, rigid structure allows room within the weight limit for sampling instruments, while providing a durable structure capable of being carried on a balloon through severe weather. The current version of PASIV is approximately 1.5 m long, 0.3 m wide, and 0.3 m tall (Figure 1). Each piece within the structure is cut from varying thicknesses of sheet Styrofoam (ranging from 12.7-25.4 mm) using a computer numerical control router. The diamond shape of the body has been chosen to provide a rigid structure that reduces drag as the instrument is pulled through the ambient environment. The opening on the top of the instrument where the particles fall through

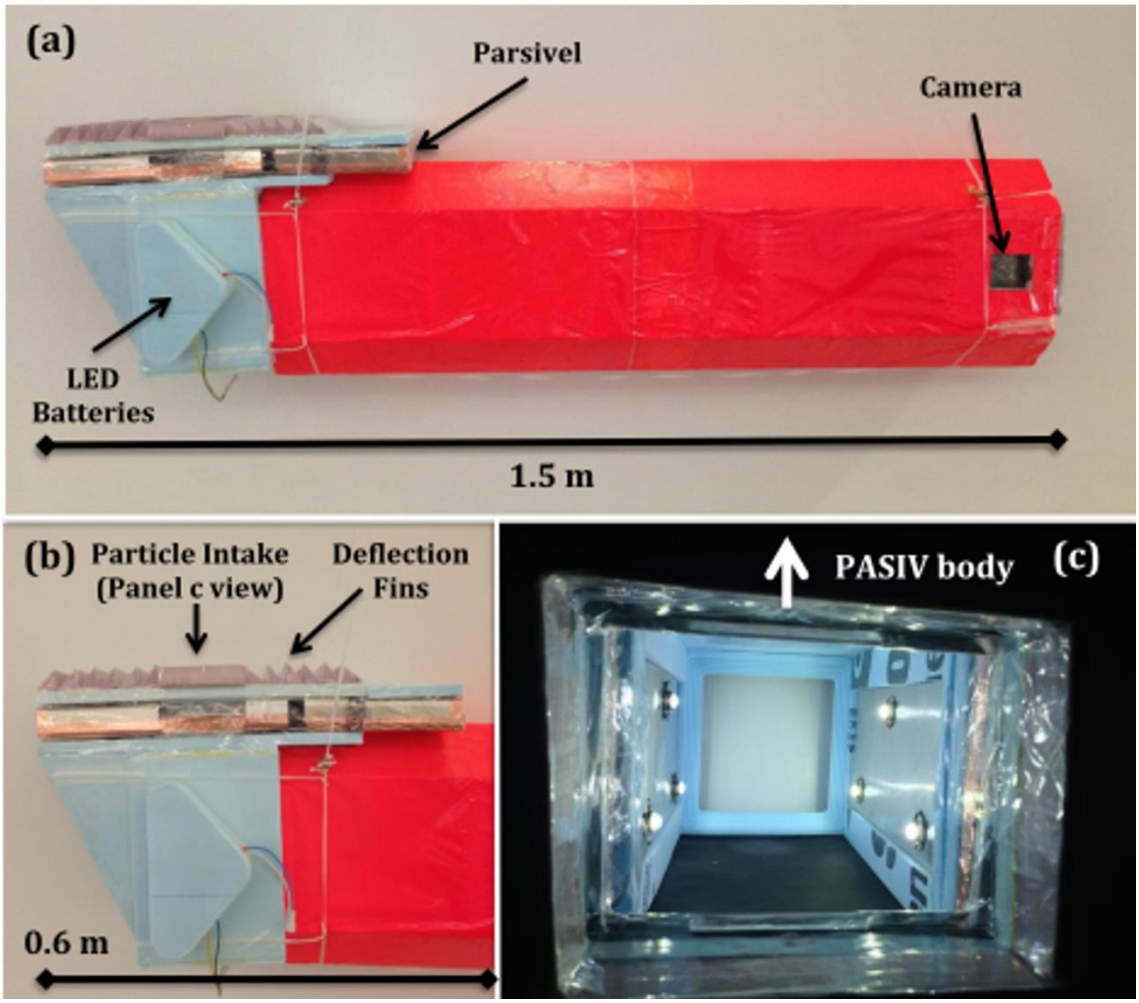

Figure 1. The configuration of the PArticle Size, Image, and Velocity (PASIV) probe. (a) The light-weight body constructed of residential-grade Styrofoam, with locations indicated for the camera mount, the PARSIVEL box, and the LED batteries; (b) detail of the viewing chamber portion of the PASIV probe, with the locations of the particle intake and deflection fins marked; (c) Viewing chamber seen from above (with LED lights on), where the HD camera is directed into the chamber from the top of the image. The high intensity lights cause the exterior of the chamber in this image to appear black, while the white floor is visible in the center of the image looking through the particle exhaust. The black background panel inside the chamber at bottom of the image increases the contrast of the illuminated precipitation particles in the HD camera images.

to be measured is surrounded by small angled fins. The angled fins are intended to suppress particle splashing and rebounds that are of significant concern when making PSD measurements (Grossklaus et al. 1998; Habib et al. 2001; Kruger and Krajewski 2002), as such events can artificially modify the sampled PSD by creating an abundance of small particles. The angled fins are used to deflect low trajectory particles away from the opening, minimizing the opportunity for these disturbed particles to enter the

instrument. Bright colors were chosen for all materials to increase the visibility of the instrument for help in the retrieval process.

Figure 2. Image of PASIV launch on 1 August 2013 during DARPA project shows large polyethylene balloon rising with parachute, radiosonde, and PASIV trailing behind. Several crew members are required to assist in holding the instrument train prior to launch.

The instrument is flown on either a 105.7 m^3 Aerostar Stratofilm balloon or a 1500-g latex balloon, and supported using waxed nylon line rated at 18.14 kg of strength. In operations, the entire instrument train consists of the PASIV, a radiosonde to provide location and thermodynamic data, and a parachute to slow the descent of the unit once the balloon bursts. To reduce the likelihood of a situation in which the balloon actively alters or shadows the particles from the sampling instrument, a let-down reel is used with 30 m of line that a delayed timer releases to unspool approximately 1 min after launch. The let-down reel is needed to keep the instrument

train short enough (3 meters) to launch the balloon during high winds (Figure 2). To further aid in the launch process, a launch tube is used to hold the balloon during inflation and instrument preparation (Rust and Marshall 1989).

2.2. Design

The PASIV is a hybrid instrument system that provides redundant in situ measurements of the particle distribution. The upper portion of the PASIV system consists of a largely modified and repackaged Parsivel (Particle Size and Velocity) laser disdrometer (Loffler-Mang and Joss 2000). The Parsivel provides particle counts as well as size and velocity distributions of the particles that pass through the intake portion of the instrument. This is similar to the Mahlke et al. (2008) 'Flying Parsivel'. Below the Parsivel is an imaging chamber through which the particles subsequently fall to be imaged by a standard, hand-held style HD video camcorder. The images obtained are digitally analyzed to identify particles and measure their properties. Together, these measurements provide information about the size, shape, orientation, and composition (e.g., habit) of sampled particles. It should be noted that these measurements are two dimensional at best. The camera is only capable of viewing particles on a single two dimensional plane, and the Parsivel gives only a maximum diameter (making it a one dimensional measurement). Although each instrument in theory is capable of estimating the PSD (subject to certain measurement constraints to be discussed), their synthesized data can combine the strengths of the individual sensors to yield increased confidence in the resulting analyses. As an example, the velocity measurements from the Parsivel can be used in conjunction with the particle data from the camera to verify

particle velocity relations. Furthermore, the two systems are independent, providing a check against one another when available.

2.2.1. Camera

The video camera is a Panasonic Model HDC-SD9P, charge-coupled device (commonly known as CCD) high-resolution camera sampling an array of 1920 x 1080 pixels (2.07 x 10^6 total pixels) at 24 non-interlaced frames per second (fps), with a user selectable maximum shutter speed of 1/8000 s. The camera is mounted on one end of the PASIV, approximately 1 m from the viewing chamber (Figure 1, a-b), and is rotated so that the long axis of the image is in the vertical plane of the PASIV. The imaged portion of the viewing chamber (Fig. 1c) measures 108 x 183 x 150 mm (width x height x depth). The opening to the top of the viewing chamber is located in the center of the upper viewing chamber face, and measures 110 x 130 mm (depth x width). The area of this opening, combined with the depth of the imaged viewing chamber, results in an effective videosonde sampling volume of 2.17 x 10^{-3} m^3 per image. The resulting physical image dimensions are 108 x 183 mm, which leads to a pixel size of 0.01 mm^2 in an HD image having 1920 x 1080 pixels. For comparison, if a VGA resolution of 640 x 480 is assumed, the pixel size increases to 0.064 mm^2 which demonstrates the importance of using an HD camera. The HD images also provide a much clearer picture than VGA, thereby allowing the end user to better identify particle size, shape, and composition. However, pixel size does not equate to identifiable object size. A better quantification for the resolving capability of the camera is given by lines per inch. This tests the ability of the camera to identify increasingly smaller lines as distinct lines rather than blurring them together. Through testing, it has been determined that the

camera is capable of resolving 100 lines per inch (each line would be 0.01 in or 0.254 mm thick). This provides a minimum size resolution for the camera. Given the balloon's maximum relative ascent rate of about 5 m s^{-1}, the 24 fps frame rate, and the vertical dimension of the viewing chamber, the successive sampling volumes during a typical flight are closely stacked, though non-overlapping, in height. Using these values, there is approximately 15 mm of vertical space between each image. Hence, the videosonde particle samples obtained from successive images may be considered statistically independent.

An aspect of camera optics known as “forced perspective” causes an object close to the camera to appear larger than the same-sized object further away. In the PASIV instrument, this would lead to errors in the apparent size of a particle in the viewing chamber if the camera is close to the particle. The apparent size of a particle depends on the angle of rays from the top and bottom of the particle relative to the lens. The larger the angle subtended by the particle, the larger its apparent size. Therefore a particle in the front of the viewing chamber would appear larger than a same-sized particle at the back of the chamber. In general, there is an inverse relationship between a particle's apparent size and its distance to the lens. Two objects of equal size with a 1:2 ratio of distance from a camera lens would have a 2:1 ratio in apparent size. To reduce this issue, the separation distance of 1.22 m between the center of the viewing chamber and the camera is employed in estimating particle size. This separation distance decreases the forced perspective effect of particles in the front or back of the viewing chamber by reducing the average subtended particle angle, thus minimizing the apparent size difference resulting from a particle's distance from the camera lens. At

this separation distance, a particle in the PASIV will have an apparent size difference in the range of 3-10 % (experimentally measured) between the front and the back of the viewing chamber. With no particle depth information available in actual particle samples and assuming a random particle position relative to the center of the viewing chamber, the expected value of uncertainty in the particle size measurement from this effect is about 7 %.

Due to the camera settings, the viewing chamber must be well illuminated to avoid dark images wherein particles are hard to discriminate from the dark background. Six high-intensity LED lights are located on the sides of the viewing chamber to provide adequate particle illumination (Figure 1, c), and are powered by a set of eight lithium CR123 batteries on each side of the viewing chamber (Fig. 1a-b). The video data is recorded on a standard eight or sixteen GB SD card. The LED lights and the rechargeable camera battery last approximately 1.5 hr. The camera, when combined with an image analysis program, is capable of resolving the size, shape, orientation, and composition of precipitation particles in the form of raindrops, graupel, small hail, and both pristine and assemblages of snow particles (e.g., Figure 3).

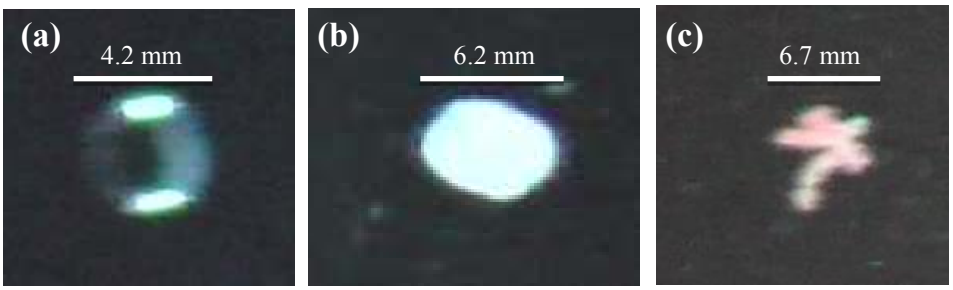

Figure 3. Sample particle images (cropped) from the videosonde instrument in the PASIV probe. (a) raindrop; (b) lump graupel particle; (c) snow assemblage. The Particle Analyzer program determines particle sizes in post-analysis as described in the text. The derived major axis lengths are 4.5 mm (raindrop), 6.2 mm (lump graupel), and 6.7 mm (snow assemblage) respectively. All particles are falling from left to right, with the illumination sources at the top and bottom of each image. The bright lobes in the raindrop image in panel (a) are internal refractions of the left and right LED arrays.

2.2.2. Parsivel

The Parsivel disdrometer is an optical sensor manufactured by OTT Hydromet (Loffler-Mang and Joss 2000). The system uses a 780 nm wavelength, 30-mm wide, approximately 1 mm thick laser beam to detect particles as they pass through the sensing area. The amount of light blocked by the particle passing through the beam is proportional to its time-varying linear dimension in the plane of the beam while the length of time the light is blocked provides information about the particle velocity (e.g., Battaglia et al. 2010). A proprietary algorithm by the manufacturer bins each detected particle according to its size and velocity, and the data output interval was set to 10 s, the minimum available. The 32 size bins are nonlinearly spaced between 0.062 mm and 24.5 mm diameter, with more bins located in the lower portion of the range (Table 1).

The velocity bins are similarly structured between 0.05 m s^{-1} and 20.8 m s^{-1}. The Parsivel unit presently does not utilize the smallest two diameter or velocity bins. The factory-designed, ground-based

Table 1. Bin diameter, size class spread, and error of the Parsivel disdrometer.

Diameter Bins (mm)	Class Spread (mm)	Bin Error (%)
0.062	0.125	201.6
0.187	0.125	66.8
0.312	0.125	40.1
0.437	0.125	28.6
0.562	0.125	22.2
0.687	0.125	18.2
0.812	0.125	15.4
0.937	0.125	13.3
1.062	0.125	11.8
1.187	0.125	10.5
1.375	0.25	18.2
1.625	0.25	15.4
1.875	0.25	13.3
2.125	0.25	11.8
2.375	0.25	10.5
2.75	0.5	18.2
3.25	0.5	15.4
3.75	0.5	13.3
4.25	0.5	11.8
4.75	0.5	10.5
5.5	1	18.2
6.5	1	15.4
7.5	1	13.3
8.5	1	11.8
9.5	1	10.5
11	2	18.2
13	2	15.4
15	2	13.3
17	2	11.8
19	2	10.5
21.5	3	14
24.5	3	12.2

Parsivel unit has been used in a number of studies to examine drop size distributions at ground level (Friedrich et al. 2013; Yuter et al. 2006; Loffler-Mang and Blahak 2001). The Parsivel measures the number of drops falling into an area in a set amount of time. To convert this size distribution to a volumetric size distribution, the particle velocity through the laser must be taken into account to determine sample volume and consequently particle concentrations for each particle size.

The factory-configured Parsivel unit is too heavy for the requirements of mobile ballooning (i.e., weighing nearly 6.35 kg in its original metal casing). To use this instrument on a balloon-borne system, the optics and electronics have been removed, condensed, and repackaged into a small aluminum box dimensioned 50.8 x 17.8 x 3.8 cm (Figure 4, a). The completed assembly is capable of running for approximately eight hours using four lithium CR123 batteries housed within the box. The Parsivel's raw ASCII particle data stream is output as a RS-485 signal that is converted into a 3.3V TTL signal and recorded on a small micro-SD data logger as ASCII text. This process bypasses the need for computer software to drive the Parsivel and turns the completed unit into a standalone instrument requiring no user interaction once initially reconfigured. The final weight of the covered Parsivel box assembly (Figure 4, b) is approximately 0.91 kg. The Parsivel box is mounted above the viewing chamber on the assembled PASIV (Figure 1, a-b). The aluminum housing effectively serves as a Faraday Cage to shield the internal Parsivel electronics from high electric fields. Although the Parsivel 1 was originally used, the current PASIV version has recently been upgraded to the Parsivel 2 (i.e., as in Figure 4, with all subsequent discussion referring to the Parsivel 2).

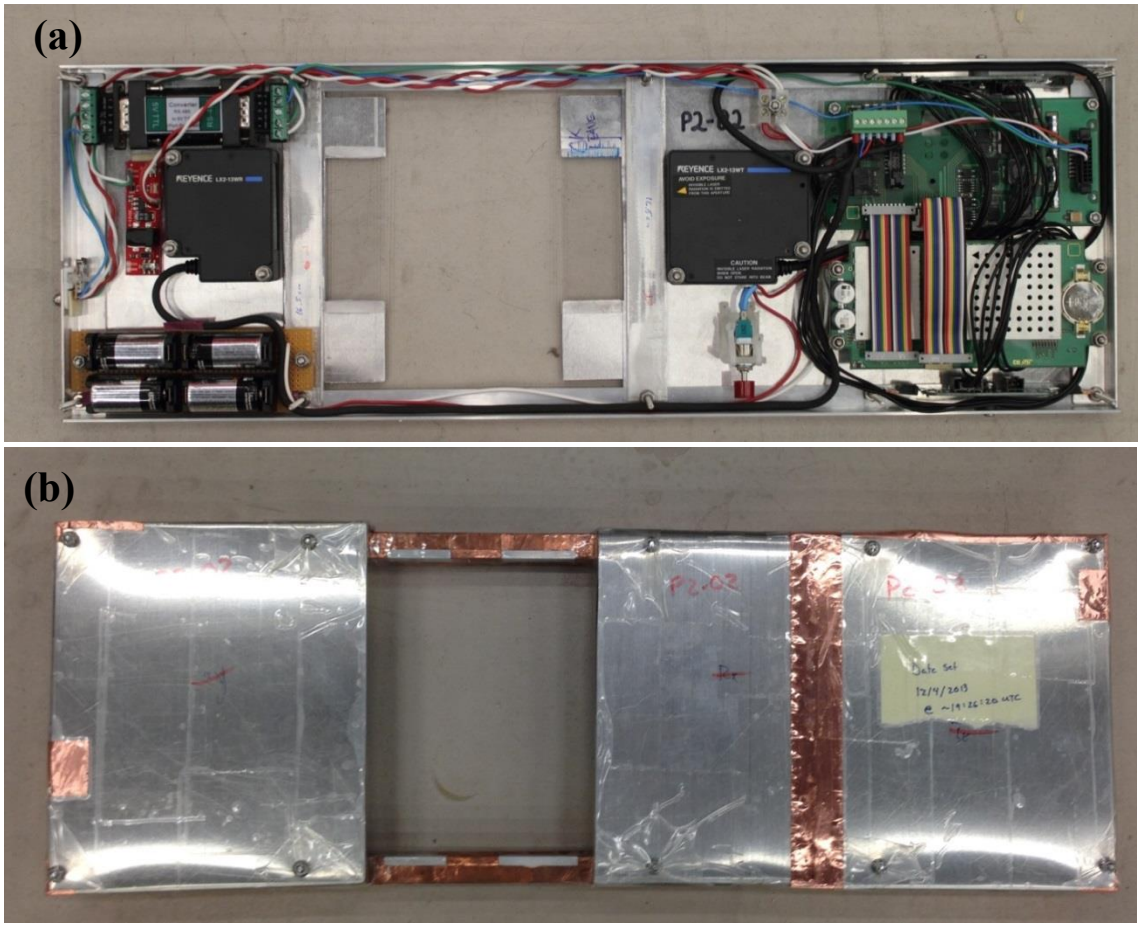

Figure 4. Parsivel disdrometer housing as adapted for PASIV. Panel (a) shows an open view of the interior circuits and laser assembly, while panel (b) shows the complete unit with covers attached. The dimensions of the reconfigured Parsivel disdrometer unit are 50.8 x 17.8 x 3.8 cm.

2.3. Operational Considerations

Certain caveats have been carefully considered during the PASIV design process to increase the accuracy and overall scientific utility of the PASIV measurements. Chief among these caveats is that the Parsivel is somewhat limited in providing only a 1-D estimate of the equivalent volume diameter within the plane of the flattened laser beam. As will be discussed in Chapter 4, the result is that the equivalent-volume diameter of non-spherical particles will likely be underestimated by the Parsivel. Hence, care must be taken when comparing the Parsivel observations to those of the videosonde system. The Parsivel also does not allow for observations of single

particles; rather, it effects bulk observations over a time period while making no distinction between potentially liquid and solid particles of varying habits.

The PASIV is presently not capable of streaming data back to a ground receiving station. Transmitting data increases the cost, weight, and power requirements of an instrument, and exposes the system to potentially destructive electrical interference in thunderstorms. Line-of-sight requirements for signal strength and data compression/conversion issues are also limiting factors. Instead, the launched instrument must be retrieved to obtain the recorded data. This considerably reduces the overall cost of the instrument by allowing it to be reused with minimal refurbishment, and reduces the design complexity.

To recover the instruments however, a GPS tracker is required to relay the landing coordinates to a retrieval team. A SPOT[1] device reliably accomplishes this goal. The uniqueness of this device is its ability to relay its location every ten min to the Globalstar satellite constellation, which in turn relays that data through the internet to a user in near real time. With this device, the instrument may be located easily via the internet-accessible location page, and typically driving and walking directly to the device with minimal searching. This retrieval is particularly feasible in the central United States with large areas of open land and relatively small bodies of water. To limit situations where the instrument is destroyed or otherwise separated from its SPOT device, two SPOT trackers are flown with one on each end of the PASIV.

This procedure has been successfully employed during ballooning operations in Oklahoma, Texas, and Florida within the United States. Out of nearly two dozen

[1] The SPOT device (www.findmespot.com) was first employed during a 2008 field experiment.

launches, on only one occasion has the SPOT tracker become separated from the instruments resulting in lost data collection systems. In fact, during one launch in Florida the PASIV landed in the middle of the St. John's river in downtown Jacksonville, and was still able to relay its location and allow recovery. The SPOT tracker has therefore provided an extremely reliable recovery method.

Another limitation of the Parsivel unit is the cost associated with each unit. This is found both in monetary costs, as well as the weight the Parsivel accounts for out of the total weight allowed by the FAA. Because of the limited number of available Parsivel units, the full PASIV instrument was flown in only a handful of cases where its success was deemed more probable. The added weight provided some reluctance to include the Parsivel unit on the PASIV in environments where downward motions were possible which would act to slow or even stall the balloon's ascent. Furthermore, extremely hostile environments were avoided as recovery of the expensive Parsivel unit was more questionable. In these situations, a camera-only version of the PASIV was flown and is often referred to as a videosonde. As described in detail in the results to follow, the only significant drawback of a camera-only system is the lack of direct velocity observations of sampled particles.

Chapter 3

Data Processing

After the PASIV is deployed via an in-storm sounding and the instrument is retrieved, the data must be processed to pair the particle data with the in-storm sounding information to provide particle size counts and distributions with associated thermodynamic and location information. This data integration process involves a series of unique steps that have been developed for the PASIV instrument. As the camera and the Parsivel produce considerably different data streams, data from each source must be processed independently and the results combined later for comparison. The following is an in-depth discussion of the steps involved, with particular focus on the challenges that each sensing system poses.

3.1. Camera

As discussed in Chapter 2, the camera records a video file at 24 frames per second and a resolution of 1920 x 1080 pixels. To automatically process these data, the video files must first be broken down into individual images. To reduce the amount of data loss through compression, PNG image types are used. At this point the measurement of particle concentration and size from the videosonde camera requires intensive and complex image processing following general digital processing techniques that are increasingly being employed in physical science studies (e.g., Erik Rasmussen, personal communication, 2010; Ogliore et al. 2012; Liu et al. 2014). To facilitate this processing need, a custom image processing program was written in IDL by Dr. Erik Rasmussen under contract to the NSSL, and is known as the "Particle

Analyzer". Used in tandem with the Particle Analyzer program, a custom Matlab script was created to merge the particle data with thermodynamic and location information from the radiosonde, as well as provide some additional data processing steps.

3.1.1. Particle Analyzer (PA) program in IDL

The Particle Analyzer (PA) program has evolved to changes throughout the course of the present research project, and as a result has become an even more powerful image processing tool than the original PA code. To begin the processing steps, an image data set is loaded into the PA program where several choices become available. The PA program is broken down into three main areas: the image area, the image selection, and the histogram area (Figure 5).

The image area shows the analyzed image currently selected after the analysis program is run, and any identified particles are displayed in the image area. The image is displayed in Boolean form, with black representing non-object pixels and pixels associated with detected particles as pure white (Figure 6). Any

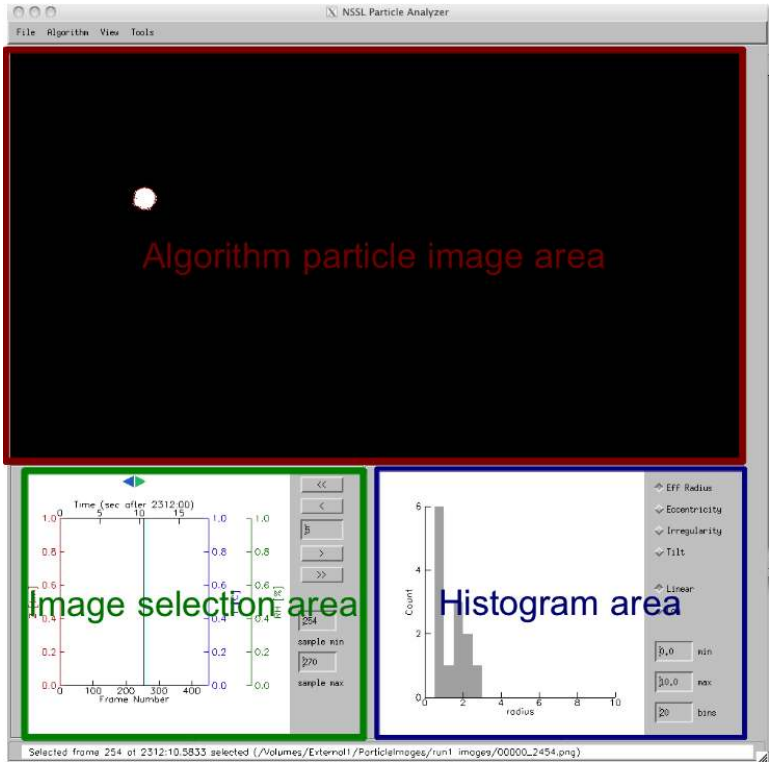

Figure 5. Output graphical user interface (GUI) of the PA program used to peruse and analyze camera image data from the PASIV. The upper panel (red outline) shows the image area and detected particle(s) for that image. The lower-left panel (green outline) is the image selection box that manages which images are analyzed. The lower-right panel is the histogram area that displays the distributions of the output statistics.

identified objects are enclosed by an ellipse fitted around the object and some basic information regarding the particle is displayed in the banner along the bottom of the program when the mouse is hovered over the object. This allows the analyst to peruse a sequence of analyzed images to examine individual detected objects as desired to help develop the necessary a priori holistic understanding of the data set before commencing interpretive scientific analysis. This can be particularly useful when examining particularly large or otherwise interesting objects, or when looking at objects in data sparse regions.

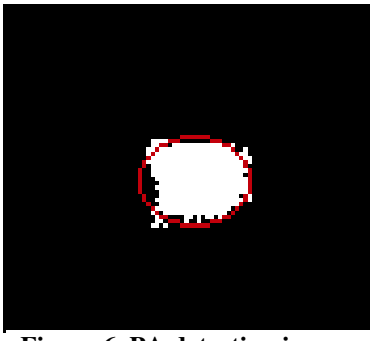

Figure 6. PA detection image. White pixels are associated with the identified object, while the red ellipse around the object shows the PA code's fit to the particle from which the measurements of size and shape are based.

The image selection area allows the user to select which images are to be processed. This is done with a simple selection box where a range of images can either be chosen graphically or using numeric values entered into a text box. The program was originally created with the intention of also incorporating sounding information to aid in the image selection. If this functionality is used, plots of temperature, dew point, and relative humidity from the radiosonde are displayed over the image selection. At this time, this feature is not used, as the required format of the sounding is different than the format of the Vaisala RS92-SGP radiosonde which was used exclusively during the research to be described. Attempts to reformat the data into the format required by the PA program have thus far proved unsuccessful, and it was deemed more time-efficient to create a follow-up program in Matlab to facilitate the merging of this data and will be discussed later in this chapter.

The final section is the histogram area and displays some basic summary plots of the analyzed data. This includes plots of the particle counts sorted by effective radius, particle eccentricity, particle irregularity, or tilt. This gives the user a quick summary of the range of particles found during analysis. Once the user is done examining any particles or summaries, the particle information can be saved to a fixed-width text file containing all of the measured variables for each particle. A complete description of the output variables from the PA program is listed in Table 2.

Table 2. Output parameters and descriptions from the PA program.

Parameter (units)	Description
image	Image number in the particle image collection
z (m MSL)	Sounding-derived height of the instrument at image time (only if sounding loaded)
T (C)	Sounding-derived temperature at image time (only if sounding loaded)
RH (percent)	Sounding-derived relative humidity at image time (only if sounding loaded)
x, y	Pixel coordinates of the imaged particle (x increasing to right, y increasing up)
r (mm)	Effective (equivalent-spherical) particle radius
maj, min (mm)	Semi-major and semi-minor axis lengths of the fitted ellipse
eccentricity	Varies from 0 (circle) to 1 (parabola)
irregularity	Average deviation of pixels comprising the edge of the detected particle from the fitted ellipse
maxIrreg[2]	The maximum irregularity value measured over the entire particle

[2] Particle parameter values only output in MTS_BRIGHTNESS and MTS_BRIGHTNESS_NOBACKGROUND algorithms.

minIrreg[2]	The minimum irregularity value measured over the entire particle
tilt (deg)	Tilt of major axis of imaged particle from the horizontal image plane
Bright_avg[2]	A measure of the average brightness value (from the luminance channel) of the identified particle. Values from 0-1, with 0 being black and 1 being white.
Bright_max[2]	A measure of the maximum brightness value (from the luminance channel) of the identified particle. Values from 0-1, with 0 being black and 1 being white.
Bright_median[2]	A measure of the meidan brightness value (from the luminance channel) of the identified particle. Values from 0-1, with 0 being black and 1 being white.
BrightHist[1-10][2]	A binned count of the number of pixels in each of 10 bins from 0 to 1 for the particle brightness. This is the histogram of the particle brightness
Bright_count[2]	The total number of pixels counted for the particle

To begin processing a data set, a set of images must first be selected. Because the PA program tracks all detected objects throughout the entire image analysis, large quantities of images are not available for a single analysis. If too large a data set is chosen, the program will eventually run out of available memory and IDL will develop an error condition and abort. Thus large data sets should be broken down into smaller segments and processed individually either in sequence or via parallel processing. Once a selection of images is chosen in the image selection pane, the appropriate processing algorithm is selected. Currently, there are four algorithms available: MTS_GIF, MTS_PNG, MTS_BRIGHTNESS, and MTS_BRIGHTNESS_NOBACKGROUND.

3.1.2. Overview of the Particle Analyzer algorithm

The program as originally written contained only the MTS_GIF and MTS_PNG algorithms. The basic process of the algorithms are similar, with the exception that they were built to handle the different image formats contained in the name. As all of the images produced from the videosonde are in the PNG format, the former algorithm is

never used and will not be discussed here. Once an algorithm is selected, a control panel window is opened and several inputs become available to the user (Figure 7).

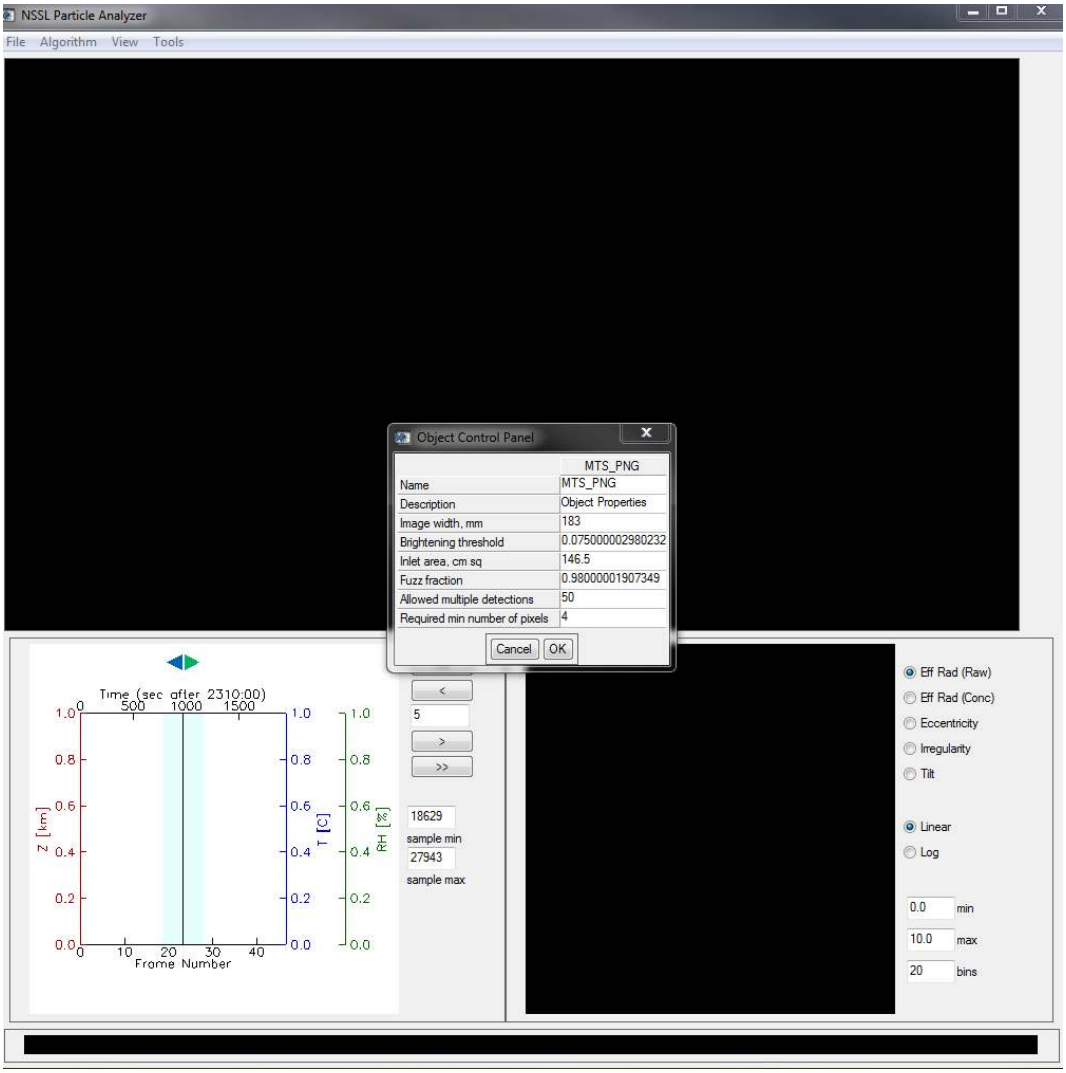

Figure 7. PA program window showing control panel options for processing algorithm

The "image width, mm" option asks for the width of the image (mm) along the widest image dimension. This value is used to scale the pixels to a physical size (mm) and its accurate entry is critically important to the subsequent proper operation of the program. The "Brightening threshold" value corresponds to how much one pixel must brighten from one frame to another to be considered for inclusion in a particle. With values ranging from zero (black) to unity (white), it represents a fractional change in

luminance. Values closer to zero would allow more detections and inclusion of background pixels while values closer to unity would severely restrict identified pixels to only the brightest values. The “Inlet area, cm sq” refers to the area of the opening on the top of the PASIV which is used to calculate concentrations when viewing them in the PA program. The “Fuzz fraction” parameter controls how many of the pixels around an identified object to include. Values for this range from zero to unity and allow the program to compare surrounding pixels to the value normally associated with background noise. A value of 0.9 for example, would require that a pixel brighten more than 90% of the value normally associated with background noise to be included in a particle identification.

The “Allowed multiple detections” parameter was originally intended to remove stationary non-particle artifacts that sometimes develops on the background of the camera viewing chamber (**Error! Reference source not found.**, c). The program would examine a pixel and if that single pixel was brightened more than the number of times input for this parameter for a given sized object, then those objects were removed. The main purpose of this parameter was to remove small detected fixed objects that scintillated on the background. However, this feature had the unfortunate drawback of sometimes removing real particles later in the flight, particularly large ice crystals that took up large areas. Given the rate at which ice crystals are often encountered in processed cases, even large values of this parameter would be reached very quickly. This problem was only discovered after several cases were run through the analysis program and examined in detail, as particle rates and sizes for actual cases were somewhat unknown during the program development phase of the research. Given the

discussion in Chapter 2 regarding the camera's sensitivity and detectable range, it was decided that any object less than a 0.5 mm diameter would not be adequately resolved to distinguish a real particle from noise. In post processing, these detections are removed from the final data set, which consequently renders this parameter obsolete. It has therefore been "turned off" by setting it to an extremely large value on input (e.g., 10,000).

The final parameter of "Required min number of pixels" sets the minimum number of contiguous pixels in any direction that must be reached before a cluster of brightened pixels could be considered an object. Given the pixel size in mm of the image frame and the resolution of the camera described in section 2.2.1. Camera, a value of four pixels is typically used to exclude objects with a diameter along its largest dimension less than 0.4 mm. Once an algorithm is chosen and the parameters input, a sequence of processing steps is completed to identify objects within each image frame and their properties measured.

3.1.3. MTS_PNG algorithm

The original algorithm written for the PA program is the MTS_PNG algorithm. In its simplest form, the MTS_PNG algorithm works by examining a difference image created by subtracting the current image from the previous image to determine what pixels have changed substantially in the current frame and could thus be considered as a particle candidate. When the algorithm is run, the first image in the selection is set as the background image, called the previousIntensityImage, to which the next image in the selection is compared. This means that in any image selection, the first image is unavailable for processing.

The MTS_PNG algorithm also examines the image and uses the user input fuzz faction to determine the noise threshold called the fuzzthreshold. This is only done once, at the beginning of the analysis, and is only calculated off the first image in the data set. Moving forward one image at a time, a difference image is created by subtracting the previousIntensityImage from the current image. The image is then smoothed, and pixels that are brightened above the Brightening Threshold are identified. Pixels are clustered together by looking for brightened pixels that continuously touch one another, ignoring pixels along a 5-pixel wide band around the image edge. False brightening of individual pixels often occur in the outer band due to portions of the PASIV frame being visible and moving slightly from one frame to the next due to vibrations of the PASIV frame (**Error! Reference source not found.**, a).

These clusters of brightened pixels are then filtered by comparing the pixel values against the fuzzthreshold value and removing non-sufficiently brightened pixels from the list. A final filter is applied to the object list to remove clusters of brightened pixels that show up repeatedly in sequential frames. Periodically with large, bright objects, ghost images can appear where an object shows up repeatedly in several frames following the first imaging, and appears to slowly decrease in brightness with each frame. This is likely caused by a saturation of the camera pixels which takes a finite amount of time to degrade, giving the appearance of a ghostlike image of a particle. These repeated detections are removed from the analysis so that only the original particle detection remains. Before proceeding to the next image in the analysis, the previousIntensityImage is set to the current image so that the background is allowed to dynamically change with the data set.

The program stores the objects that remain after these steps, and moves on to the next image to repeat the process. As was mentioned earlier, because the program is storing all of these detected objects in memory until all images are analyzed, if too many objects are detected the program will abort due to insufficient memory. This becomes more of a problem in real cases with very high objects densities. To combat this issue, each data set must be processed in smaller sub-sections. Once all images in the selection are analyzed, each identified object is then run through a subroutine that fits an ellipsoid to the object. The subroutine was built following the work of David Fanning (Fanning 2003) and uses Eigenvectors and Eigenvalues of a tensor built on the pixel locations relative to the center of each object to determine the object's fitted values of semi-major and semi-minor axis, tilt, and eccentricity. This effectively identifies the fitted ellipse that contains the object. The effective radius of the circle with the same area as the fitted ellipse is then calculated. The particle lengths are given in terms of pixels, so a unit conversion from pixels to millimeters is applied before the values are output from the program. To measure the irregularity, the distance of each pixel to a point on the fitted ellipse along the same radial as the pixel from the center of the object is measured. The average value of these deviations is reported as the irregularity.

The result of this process is a series of images where objects are identified and sized according to the dimensions of the image. While the program works reasonably well, there are some subtle yet critical problems with this analysis method that caused the program to fail to identify some objects. The largest problem resides with the fuzzthreshold and its single calculation. Because the fuzzthreshold is only calculated once using the first image in the selection, this makes the program highly sensitive to

changes in brightness from that image. If a selection of images is run with a different starting image, then a given image will be processed differently as the fuzzthreshold value can change significantly. As an example, if the starting image is abnormally bright compared to the current image being analyzed, identified objects can be removed as they may fall below the now too high fuzzthreshold. Conversely, if the starting image is abnormally dark, pixels associated with the background will be included in identified objects making their measurements larger than the actual object. If the object does survive, the measured size can change appreciably due to the inclusion or removal of pixels surrounding the object based on this changing noise threshold.

This becomes more problematic due to the fact that the data set must be analyzed in segments, which means that later in the flight the starting image likely contains numerous precipitation particles seen as bright objects. These bright pixels shifts the histogram of brightness values across the entire image higher, and consequently raises the background noise threshold, thereby removing more identified objects from the image analysis. As a result, the PA program produced inconsistent results for identified objects and their measured sizes, highly dependent on which starting image was chosen.

An additional shortcoming of the MTS_PNG algorithm was identified as the particle data was examined for applications after processing. A key aspect of the post processing and analysis for individual cases to be discussed in Chapter 5 is the ability to automatically classify particles into different particle habits. It was found that a critical parameter in determining particle habits was how bright the actual object is, and what the histogram of the brightness values looked like. These measurements were not

included in the original algorithm and thus made automated classification of the detected particles difficult if not impossible. Given the inconsistent results and shortcomings of the MTS_PNG algorithm, two additional algorithms were created to address these issues moving forward with the PA analysis, MTS_BRIGHTNESS and MTS_BRIGHTNESS_NOBACKGROUND.

3.1.4. Brightness algorithms

The purpose of the brightness algorithms is to address two key problems. The first is to fix the inconsistency issue associated with the fuzzthreshold calculation. The second is to expand on the measurements already being made to include some measure of the particle brightness for use in particle habit classification. Both the MTS_BRIGHTNESS and the MTS_BRIGHTNESS_NOBACKGROUND algorithm are largely copies of the MTS_PNG algorithm but with some modifications and additions. The calculation of the fuzzthreshold was first moved inside the image loop so that it is now calculated with each new image. As the program progresses through the analysis, each previousIntensityImage is used to find the fuzzthreshold value that will be used on the current image. Given that this image may contain brightened objects which could skew the background noise level, the fuzzthreshold is only calculated using the lowest 50 % of a histogram of brightness values ranging from zero to unity. This effectively excludes any pixels that would be associated with bright objects and allows the noise threshold to be calculated based on actual background values.

By calculating the fuzzthreshold this way, the noise parameter is allowed to vary with the dynamically changing conditions of the camera. This is particularly relevant as

the lighting conditions of the camera change throughout the course of a flight. As the LED batteries drain, the intensity of the lights will decrease, resulting in a darker image, but these intensity changes are also somewhat sensitive to temperature changes (colder temperatures reduce power faster). Ambient light can also act to brighten an image, particularly near the tops of storms as sunlight begins to penetrate the cloud layer.

After fixing the repeatability issue with the PA code, it was desired for a few additional measurements to be made regarding each particle, to aid particle classification efforts once the data set is processed. The first addition was to include particle brightness. Once the pixels are identified for a given object, the mean (Bright_avg), median (Bright_median), and maximum (Bright_max) values of brightness for all the pixels of that object are measured and recorded. This information is pulled directly off the luminance channel from the current image. Additionally, a ten bin histogram of brightness values (BrightHist) ranging from 0 to unity of those pixels as well as the total number of pixels counted (Bright_count) is recorded. This provides information about how bright the actual object was. The final addition was to measure the maximum and minimum irregularity, rather than simply the average value. It was felt that information about these maximum and minimum deviations could be useful in particle type discriminations. These changes were made to both algorithms.

The only difference between the MTS_BRIGHTNESS and MTS_BRIGHTNESS_NOBACKGROUND algorithms is the image used for the previousIntensityImage. In MTS_BRIGHTNESS_NOBACKGROUND, the previousIntensityImage is the image preceding the current frame (identical to the MTS_PNG algorithm), whereas in MTS_BRIGHTNESS it is a 50-image composite is

used. In originally trying to fix the MTS_PNG algorithm to track with changes in the average brightness of the current image as the flight progressed, it was thought that using a single image could expose the PA code to influences by abnormally bright images. A pixel by pixel composite image over the previous 50 images was constructed which reduced the influence of any singly bright image or any particles present in the images.

While this processes produced a very clean background image to be used for the current image analysis, the composite process took a considerable amount of time and made the PA program rather inefficient for processing images in a timely manner. Additionally, it provided no significant improvement over using a single image, and so was not worth the considerable increase in computing time and is no longer used.

3.1.5. Post-processing with Matlab

Once the PA code has been run for the entire data set, the results from individual processed segments are merged together into a single comprehensive data file. The typical procedure for processing a data set is to divide the total image set into smaller subsections, often of roughly 20,000 images per section. When running the analysis on each section, the start of each subsequent section slightly overlaps the previous section (by roughly 50 images), so that all images are analyzed. This procedure accounts for any spin up time the program requires such as the first image not being included in the analysis. Once all images are analyzed, the individual sections are combined into a single record, and any repeated detections due to analyzing an image more than once are removed. This file contains a single record for each particle detected by the PA program. To place these particle detections in the context of the storm environment, it

must first be paired with the radiosonde data from that flight. As noted previously the PA code functionality for soundings cannot be used with the cases we obtained, so a Matlab program called Combine_PA_with_sonde_v5.m was written.

The program first asks the user to identify the launch point in the radiosonde data, using a plot of GPS altitude (Figure 8). The user is asked to identify the point at which the altitude begins to increase due to launch. The radiosonde data is then trimmed using this information so that any data collected at the surface prior to launch is removed. This allows the first record of the radiosonde data to be matched with the first image of the particle data. Before moving forward, the radiosonde data is examined for any missing data points in the temperature, dew point, pressure, relative humidity, and altitude fields, and any missing records are filled in using linearly interpolation between the good records.

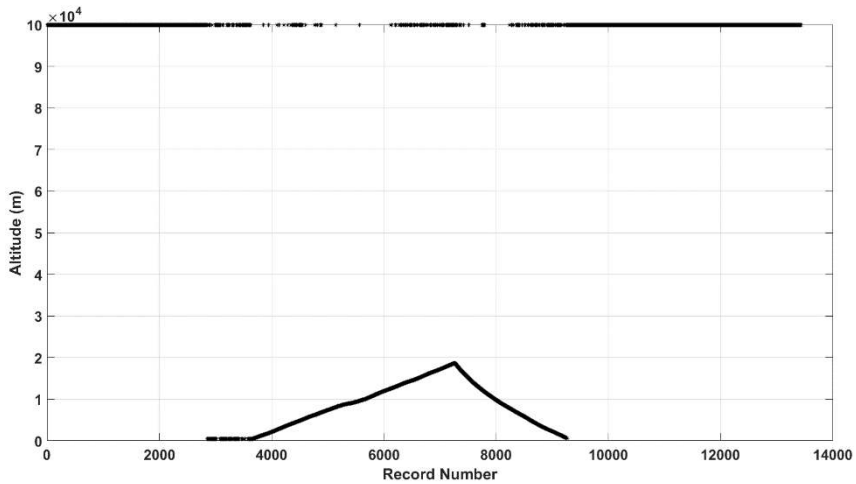

Figure 8. Processing figure of GPS altitude (m) vs time (s) for identifying launch in the radiosonde data for the PASIV. Data from June 21st, 2012 case shown, launch was at 3654 seconds. Data points along the top of the figure are missing data values from the sonde.

To match the particle records to radiosonde records, the elapsed time based on the camera frame number (rounded down to the nearest whole second) is compared to the run time variable of the radiosonde data, and the camera frame is paired with the matching radiosonde record. Because the frame number is included in the data for each

particle, the matching radiosonde record can then be assigned to each particle. The result is a complete data table that has thermodynamic and location information for each particle detected by the PA program where radiosonde data are available. It is assumed during this process that the particle information contains only detected particles during the ascent portion of the flight (i.e. that the descent portion was not analyzed). It will also only fill in information where records are available, hence it is possible that the latter portions of the particle table could have no identifying information if the radiosonde data were incomplete. The data table is saved under an appropriate filename and the processing of the particle data is now complete.

3.2. Parsivel

The Parsivel unit as manufactured by OTT produces a data stream of particles binned over a set period of time. Before deployment, the data output structure of the Parsivel can be set to a user defined ASCII string, and the output rate can be set (as discussed in section 2.2.2. Parsivel). To provide the most comprehensive and flexible data possible, the user defined string is set to output the variables listed in Table 3, in that order. Most of the variables output by the Parsivel are for diagnostic purposes and setup; however the Raw Data variable contains the unprocessed particle data that are used to produce size spectra and velocity distributions. The raw data are output as a semicolon delimited string of 1024 particle bins corresponding to each size and velocity combination. Before these data can be used however, several

Table 3. Parsivel Output Variables, in order

Serial Number
Rain Intensity
Rain Accumulation
Radar Reflectivity
Sample Interval
Signal Amplitude
Number of Particles
Sensor Temperature
Battery Voltage
Date/Time
Raw Data

processing steps are required to identify the records associated with the actual flight and then to merge these data with the thermodynamic and location information from the radiosonde.

3.2.1. Identifying launch

The first step in processing the Parsivel data is to trim the record to reflect only the time in which the PASIV is actually deployed in a storm. This requires identifying when launch occurs in the Parsivel data stream. This step is necessary as the Parsivel, like the camera, is turned on prior to the actual launch of the PASIV instrument. The result is that several records of data exist in which the PASIV is sitting on the ground, potentially being contaminated by surface vegetation and/or human interaction as the unit is moved in preparation for launch. Since the Parsivel has no visual component, it can be difficult to determine at what record this actually occurs. The date/time of the Parsivel itself have been known to drift, sometimes substantially, and therefore cannot be trusted to identify launch time. Thus to facilitate identification of the actual launch, for several records prior to launch the laser path is intentionally blocked by either a folded piece of paper or the hand of the crew member launching the PASIV. The result is that the signal amplitude is significantly reduced, often to near zero.

Once launch occurs, the following record shows a sudden increase in the signal amplitude back to full strength. A custom Matlab script, Process_Parsivel_Data_v3.m, was written to identify this feature and use its location in the data to remove the records prior to this point. The program creates a plot of the signal amplitude, battery voltage, and number of detected particles vs time, and prompts the user to identify the point at which launch occurs (Figure 9). Following this, the trimmed data are saved with an

appropriate filename and the next step of merging the data with the radiosonde information can begin.

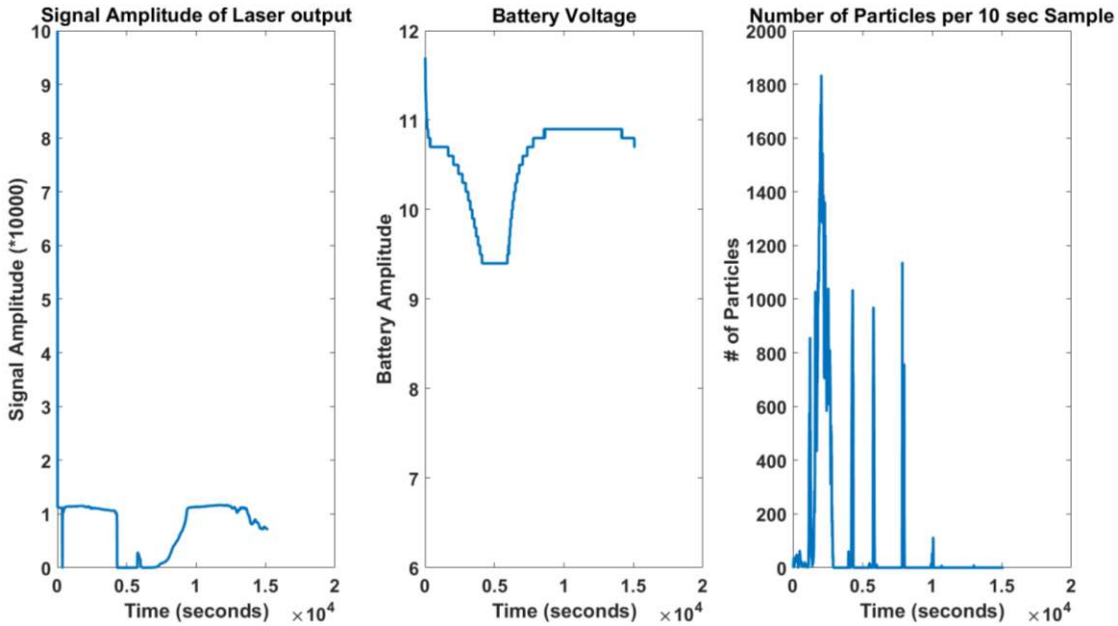

Figure 9. Parsivel processing plot for identifying launch time. Left shows signal amplitude, middle shows battery voltage, and right shows the number of detected particles per time step. The launch record is identified by the small downward spike in the signal amplitude near 350 s.

3.2.2. Merging with radiosonde data

Once the Parsivel record has been trimmed to exclude any data on the ground prior to launch, the data can be merged with the radiosonde information. A second program was written to perform this function, Combine_Parsivel_Sonde_Only_v2.m. To complete this process, the launch times in each data stream must be aligned correctly. As the Parsivel outputs data every ten seconds, the rest of the information can be easily matched to the correct record once the start points are matched. At this point in the processing, the first record of the Parsivel is the launch time, so the radiosonde data must be trimmed to include only the data during flight. Similar to the previous step, a plot of the GPS altitude is created and the user is prompted to enter the

start time (Figure 10). This process is nearly an identical to that used for the camera data processing.

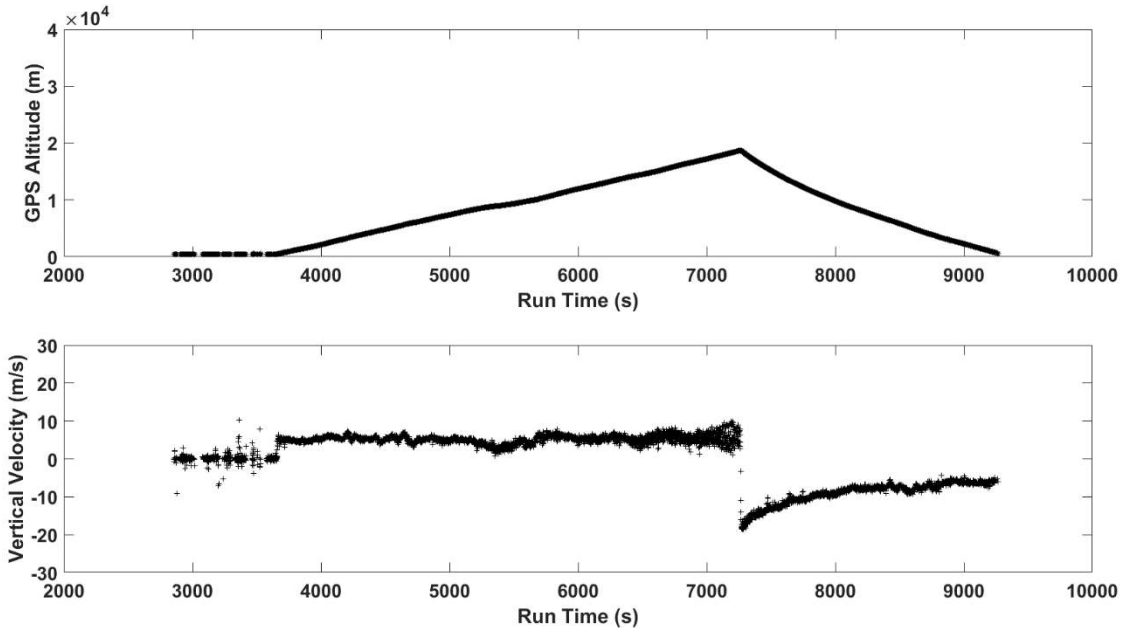

Figure 10. Processing figure for identifying launch in the radiosonde data. Top is GPS altitude (m) bottom is vertical velocity (m s^{-1}). A combination of increasing altitude and sudden positive vertical motions indicates launch. This figure shows data from June 21st, 2012, launch was approximately 3600 seconds.

Before merging the data streams however, the radiosonde data must be averaged to match the output frequency of the Parsivel data (set to ten sec). A ten second, non-overlapping average of the radiosonde temperature, relative humidity, pressure, wind speed/direction, vertical velocity, latitude, longitude, and altitude fields are computed and matched with each corresponding Parsivel record. Because the fact that the Parsivel and the radiosonde operate independently, it is almost a certainty that the data streams will not be the same length. The program takes this into account by continuing the matching process until the end of the shorter record is reached. The resulting merged data are then saved as a comma-delimited ASCII text file with an appropriate name that can be input into the final analysis program discussed in Chapter 5.

Chapter 4

Particle Data Validation and Integration

Before deploying the PASIV on an actual storm for data collection, the instrument was first extensively tested to determine its ability to accurately size and detect particle objects. A formula for computing the PSD was developed that incorporated objective correction procedures to mitigate estimated sampling biases.

4.1. Sizing accuracy and correction

A series of tests were conducted in which conditions surrounding the PASIV could be controlled and its response characterized. However, first a test of the ability of the PA code to accurately represent the particles detected was necessary. A series of spheres of known diameter were dropped through the PASIV and the raw images compared with the PA processed images (Figure 11). To simulate real particles, two types of spheres were used, an acrylic sphere and a delrin sphere. An acrylic sphere closely resembles a visual image of a raindrop when viewed by the camera[3] (i.e., including external reflection and internal refraction of

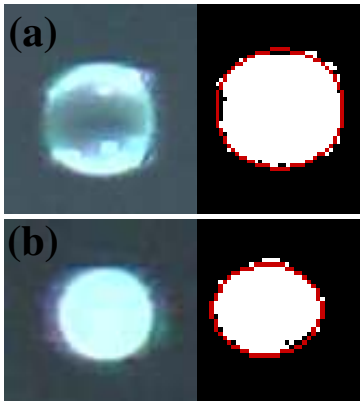

Figure 11. Sample camera-imaged (left column) and analyzed (right column) images of test particles with known size and physical characteristics. The upper panels (a) correspond to a 4.76 mm acrylic test sphere (upper-left panel) to simulate rain, while the lower panels (b) correspond to a 3 mm opaque white delrin test sphere (lower-left panel) to simulate graupel. The PA-analyzed particles (right-column) are indicated by contiguous white pixels, while the background is masked with black pixels. The fitted elliptical outlines of the test spheres are depicted by the red curves.

[3] Alternatively, Liu et al. (2014) employed glass spheres to simulate raindrops in their drop tests.

incident light), while a delrin sphere closely resembles a graupel particle in dry-growth mode.

A comparison of the raw images to the PA identified images in Figure 11 shows that the identified whitened pixels and the fitted ellipse are similar to the observed particles in the raw images. This provides confidence that the PA code is correctly identifying the edges of detected objects and accurately fitting an ellipse to the brightened pixels.

To determine the sizing accuracy of the PASIV, an expansion of the previous test was performed where a range of objects of known diameters were dropped through the instrument. By comparing the measured sizes to the actual sizes, any biases in the PASIV could be identified and potentially corrected. For the purposes of this test, three types of spheres were used: steel, acrylic, and delrin. As mentioned previously, the acrylic and delrin spheres resemble rain drops and graupel particles respectively, and so were chosen based on their similarity to actual objects. However, only a limited diameter range of these spheres was available. To compliment these sizes, a set of steel ball bearings was also used to increase the size range sampled during this test.

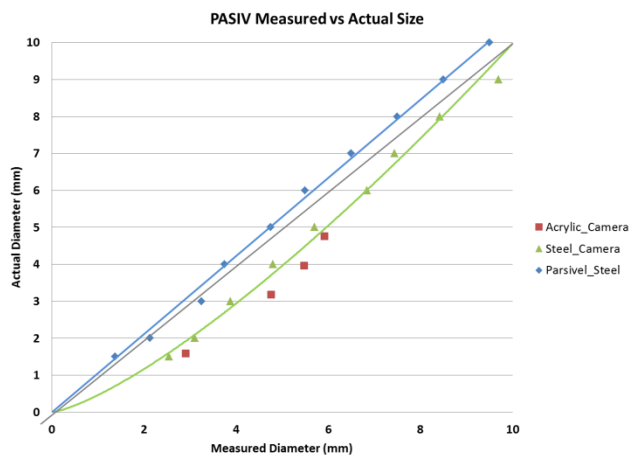

Figure 12. Summary of sizing test conducted on the camera and Parsivel sensor components of the PASIV. The one-to-one line (light gray) and power-law regression line for the Parsivel steel (blue) and Camera steel (green) are also shown. The Delrin spheres are not shown but showed similar offsets as the acrylic spheres.

For the purposes of this test, a single sphere of each type at each available size was dropped through the PASIV from a height immediately above the intake. Each particle was dropped in the center of the intake to ensure that it passed through the Parsivel laser and the video chamber. The data were then analyzed using the methods outlined in Chapter 3 and the results examined (Figure 12). In the figure, the detected steel ball bearings are plotted in blue for the Parsivel and green for the camera-PA system. The red points show the acrylic spheres for the camera, and the delrin spheres are not shown. There was no appreciable difference between the acrylic, delrin, and steel spheres in either the camera or the Parsivel, so only the acrylic spheres for the camera are shown for reference. The one-to-one line is shown in light gray to give an indication of over- versus under-sizing.

The results of this test indicate that the camera-PA system had a tendency to systematically oversize objects below 10 mm by up to 20% at 5 mm diameter. As the objects became larger, the oversizing behavior decreased to zero by 10 mm. Given the smooth behavior of the offset, a power-law function was fit to the PA-analyzed steel drop test data using a Levenburg-Marquardt nonlinear least squares algorithm and takes the form

$$D_{cor} = 0.4514 \times {D_{PA}}^{1.3264}, \tag{1}$$

where D_{cor} is the corrected diameter (mm) and D_{PA} is the PA-derived equivalent spherical volume diameter (mm). A bounded linear relation would also be appropriate for the data, but would result in an unrealistic intercept parameter. Since the trend should go through the origin based on physical constraints, a power-law fit is more appropriate for smaller-diameter objects.

The Parsivel data in Figure 12 shows an average tendency to underestimate the size of the steel test spheres, though the deviation is typically only around 5 %. This is largely caused by the size of the bins used to separate the detected spherical objects (i.e., the object size is reported as the center of each bin), and results in a maximum size difference of approximately ± 8 %. It is noted that the PASIV flights in storms (e.g., as discussed in Chapter 6 and Chapter 7) have revealed a tendency for many PA-analyzed precipitation particles to be significantly elliptical in shape (e.g., long, narrow, needle-shaped ice crystals in the 2-D image plane). As the plane of the major axis (as viewed by the camera) is often not parallel to the flattened Parsivel laser beam, the Parsivel observations are thus often characterized by smaller measured particle diameters than the equivalent-spherical PA-analyzed particle diameters. A regression relationship similar to Eq. (1) could be fitted to the Parsivel data from the drop tests using the same power law form as the PA data analysis (though is not presently). A regression line was not fit as it is hypothesized that the ellipticity shape errors could locally dominate in storm observations and represent an uncertainty that cannot be corrected using the Parsivel data alone. Instead, the overall Parsivel error of each size bin is simply estimated according to the class spread of that particular bin (Table 1).

4.2. Detection accuracy and sampling correction

Given the frame rate of the camera and the viewing chamber size, it is possible that faster-moving particles may be missed between frames of the camera whereas slower moving particles could be counted multiple times. Each image of the viewing chamber is taken in 1.25×10^{-4} s (i.e., the shutter speed of the camera), and there is a period of 4.17×10^{-2} s between successive images (i.e., the frame rate). If an average

balloon ascent rate of 5 m s^{-1} is assumed, a particle falling at 2 m s^{-1} relative to ground travels through the viewing chamber at 7 m s^{-1} and has a residence time of only 0.026 s in the viewing chamber. A particle at this speed is therefore capable of traveling through the viewing chamber entirely between frames without being imaged.

It is noted that blurring of moving particles is fortunately very unlikely (and at any rate is not observed) during the frame capture despite the finite shutter speed and relative particle motion, since an imaged particle is actually captured by successive scans that take only a small fraction of the total image time in proportion to the ratio of particle diameter to image dimension. For example, if it is assumed that the camera scans each vertical line of the pixel array sequentially (there are 1920 vertical lines), then each vertical pixel band (horizontal bands relative to the mounted camera orientation) takes only 6.5×10^{-8} s to scan. A 5 mm diameter object would encompass 50 pixel arrays, and would therefore be scanned entirely in 3.3×10^{-6} s. At a 7 m s^{-1} fall speed this would result in a movement of only 0.02 mm, a displacement well below the detectable limit of the camera itself. If the camera scans the horizontal lines (i.e. the vertical lines relative to the mounted camera orientation) of the pixel array (there are 1080 horizontal lines) the particle would move 0.04 mm while being scanned. While larger, this is still well below the detectable limit of the camera. However, relatively large particles could potentially be slightly distorted with respect to the vertical image dimension due to a particle's proper motion between successive image scans. As the camera is a commercial product, specific details about the pixel scanning strategy and inner workings of the actual optics of the camera are not available. This thought

experiment and actual observations nevertheless demonstrate that particle motion during frame capture is not of significant concern.

Aside from the consideration of particle motion on image sharpness, it is still of interest to determine how likely a particle is to be imaged given that it passes through the PASIV. A theoretical expression for the particle detection efficiency (ε) has been derived following the work of Liu et al (2014) and takes the form

.

$$\varepsilon = \frac{[H - (D_{cor})]}{V_P R_{fps}}. \tag{2}$$

Here H is the height of the viewing chamber (mm), D_{COR} is the corrected diameter of a given object (mm) from Eq. (1), V_P is the velocity of the precipitation particle (m s^{-1}), R_{fps} is the frame rate of the camera (s^{-1}), and a perfect detection corresponds to an ε value of unity. The term D_{COR} is used to ensure that the imaged particle is completely contained within the viewing chamber, and taken with the input values of H and V_P represents the particle residence time in the imaging volume. The quantity R_{fps} can be conceptualized as the sample time, hence Eq. (2) is effectively the ratio of the residence time to the sample time. The theoretical ε

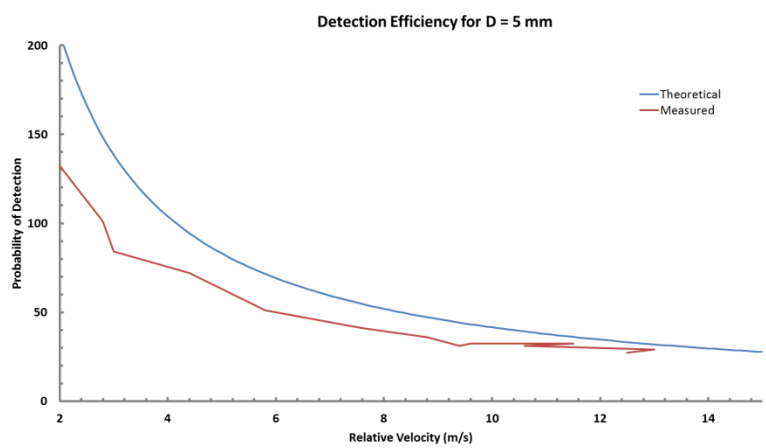

Figure 13. Detection efficiency (100 x ε, %) derived from Eq. (2) in the text (blue line), scaled by 100 (e.g. efficiency in percent), and assuming a 5 mm particle diameter. The red line is an experimentally determined curve by dropping 500, 5 mm steel ball bearings repeatedly from varying heights. The relative velocity is the particle velocity with respect to the PASIV frame of reference.

value as expressed by Eq. (2) is a function of particle diameter and can be calculated either for a given size over a range of velocities (Figure 13) or a range of sizes assuming terminal velocity. The latter case would produce a similar curve as the theoretical line shown in Figure 13.

To approximately gauge the validity of Eq. (2), an experiment was designed where steel ball bearings with a diameter of 5 mm in diameter were dropped 500 times from various altitudes through the PASIV. To vary the velocity of the ball bearings, a series of sequentially higher pipes were constructed in the northwest stairwell of the multi-story National Weather Center (NWC) in Norman, OK. By dropping the ball bearings from increasing heights, larger velocities could be attained just before the objects entered the PASIV imaging chamber. The pipes acted to contain the objects and ensure that they passed through the PASIV sensing area. The number of detected objects was compared against the known number of dropped objects at each release height (up to 24.4 m above PASIV level). The velocity of the objects at each release height was determined by the average velocity of all ball bearings that passed through the Parsivel. The resulting computed detection efficiency as a function of velocity (red line, Figure 13) conformed to a similar functional dependence to Eq. (2), though is offset by a small amount. This offset is likely caused by velocity averaging and under-sampling (not all the objects went through the Parsivel laser), causing the observation-derived curve to be shifted toward lower efficiencies.

4.3. Computation of the particle size count and particle size distribution

The particle size count (PSC) from either camera or Parsivel data is computed by assigning sized particles to the size bins listed in Table 1 and storing the total count

in each size bin. It should be reiterated that whereas the PSC is a simple histogram of particle counts per size bin through the specified layer depth, the particle size distribution (PSD) is the concentration (number per unit volume per size bin) through the specified layer depth. By applying the size correction to each particle following Eq. (1) and placing each size-corrected particle of diameter D_{cor} into its appropriate size bin, an estimate of the corrected particle size count $N_T^*(D_{cor})$ is obtained from the camera data by adding the raw size-corrected particle counts per frame in each bin over the total number of frames (n). The derivation of $N_T^*(D_{cor})$ from the Parsivel data is analogous to the procedure followed for the camera, except that the time period length of the binned Parsivel observations is equal to the product nR_{fps}, where n is the number of frames, from the camera.

Applying the detection efficiency ε for each particle size bin following Eq. (2), an estimate of the particle size distribution (PSD) or N(D) is obtained using

$$N(D) = \frac{N_T^*(D_{cor})}{n\Delta V\varepsilon}, \tag{3}$$

where $N_T^*(D_{cor})$ is the previously described size-corrected PSC for camera data and ΔV is the volume sampled per videosonde frame. The PSCs are not presently calculated from the Parsivel observations since individual particle diameters and fallspeeds are not recorded. Perhaps the Parsivel PSD could potentially be estimated in a future test by evaluating the theoretical detection efficiency via from Eq. (2) using the bin-averaged Parsivel-measured particle fallspeed.

Chapter 5

Combined Data Analysis

After collecting the data, archiving, and processing the individual data files as described in Chapter 3, corrections and analysis can proceed. Given the complexities of the individual data structures and processing requirements, it was deemed prudent to do the individual processing steps separately for the camera and the Parsivel. However the analysis of the data is better suited when working with all of the available data simultaneously. To accomplish this goal, a single Matlab program was created to handle all of the data mergers, corrections, and analysis. This program, PI_PARSIVEL_EFM_Sonde_Analysis_v9.m, has undergone several changes and iterations but represents the final step in the data processing. To begin, the program first prompts the user to select any of the input files available for a given case. These files can include the merged "Parsivel-Sonde" data file, the combined "Electric Field Meter (EFM)-Sonde" data file (MacGorman and Rust, 1998), the merged "Camera-Sonde" data file, and the observed radar file called the "Traverse" data file after its program name. The common connection between these data files is the radiosonde information which allows comparisons between the different instruments and measurements. Each file has its own section within the larger processing code and any applicable corrections or calculations are performed there.

5.1. Main program: Parsivel

By the beginning of this processing step in the analysis, the Parsivel data has already been merged with the radiosonde data and thus requires little further

modification. The results of testing in Chapter 4 indicated that the measured particle sizes need not be corrected, so no modifications to the original data are made. Once the data file is read in, the program first trims the data so that only the ascent portion of the sounding remains. An automated process is used to do this by looking for the first occurrence of five sequential records of negative vertical velocity. Occasionally there are missing records or the sounding is incomplete, in which case this automated process fails to detect the balloon burst point. In these situations the user is prompted to manually select the end of the ascent on a plot of the vertical velocity, similar to the procedure outlined in Chapter 3. The data are then trimmed to remove any records after this point.

Once the data have been trimmed for ascent only, the raw particle bin data are broken down into a PSC and a particle velocity distribution (PVD). The velocities measured by the Parsivel at this point include the ascent rate of the balloon itself, which is typically about 4-5 m/s. However, ice loading and underinflated balloons can act to reduce the vertical speed of the balloon. As such, an assumption must be made regarding the ascent rate of the balloon over a given layer, and that vertical velocity used to either adjust the measured velocities of the Parsivel downward or adjust any theoretical relations upward. Currently concentrations from the Parsivel are not computed as doing so requires taking into account the velocity of each particle to determine an effective sampling volume.

5.2. Main program: EFM

The balloon-borne EFM has its own set of processing steps which is not the focus of this work and is not covered here. For more detail on these, the reader is

referred to MacGorman and Rust (1998), who covered the history and operation of this instrument. The end result of these processing steps however is a merged data file containing the local electric field observations merged with radiosonde information. Once the merged file is read in, the end of the ascent portion of the flight must be determined. Like the Parsivel data, it is possible that records exist after balloon burst, but the focus is on the initial ascent only. Following a similar procedure to the Parsivel section, the user is provided a plot of the vertical velocity and asked to identify the balloon burst point. For simplicity, the automated detection of this feature was not implemented for the EFM data. The data are then trimmed to reflect this choice.

Once the ascent portion has been identified, the next step of the program is to identify charge layers. Gauss's law may be used with the electric field measurements from the EFM to infer charge layers using the relation

$$\rho = \varepsilon \nabla * \boldsymbol{E}, \tag{4}$$

where **E** is the vector electric field, $\varepsilon = 8.86 \times 10^{-12}$ F m^{-1} is the permittivity of air, and ρ is the space charge density. Due to the vertical nature of the sounding, no information is available regarding the horizontal changes in the vector electric field. To address this, the charge is assumed to form horizontally infinite layers of homogeneous charge distribution, which causes $\delta E_X/\delta x$ and $\delta E_Y/\delta y$ to be zero. A 1-D approximation to Gauss's law is made and only the vertical component is examined (Schuur et al., 1991, Bruning et al, 2007). The user is asked to identify the points at which the charge layers should be determined. This is done by plotting the vertical component of the electric field against pressure and prompting the user to select the appropriate points (Figure 14). To reduce noise on the plot and the calculation of charge density, the vertical

component of the electric field is averaged with a non-overlapping 60 second filter. The points selected are then used to define the charge layers, and the charge density for each layer calculated using Eq. (4).

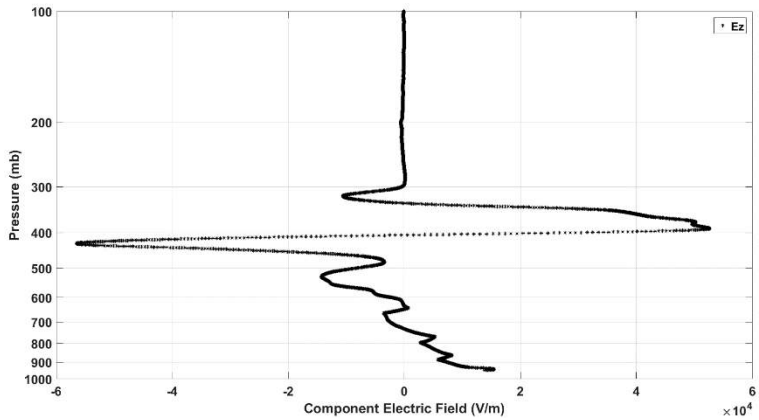

Figure 14. Plot of the vertical component of the vector electric field vs pressure. Values are averaged at a 60 second interval to reduce noise.

5.3. Main program: Camera

The camera section is by far the most intensive processing section of the PI_PARSIVEL_EFM_Sonde_Analysis_v9.m program. Before any analysis can be done the raw particle data must be size corrected as demonstrated in 4.1. Sizing accuracy and correction, noise removed from the PSC, each particle classified, the PSC binned and concentrations calculated, and finally radar reflectivity and mixing ratios for the measured concentrations determined.

5.3.1. Size correction

After loading the merged camera-sonde data file, the first task as previously described in 4.1. Sizing accuracy and correction is to correct the measured size distributions according to Eq. (1). This adjusts the detected particle diameters only, so the major and minor axis values must be recalculated using the original axis ratio. If the area of an ellipse and the area of an equivalent circle are equated, then the minor (a) and major (b) axes are

$$a = \sqrt{\gamma {r_{cor}}^2} \tag{5}$$

and

$$b = \sqrt{{r_{cor}}^2/\gamma}, \tag{6}$$

where r_{cor} is the size corrected radius and γ is the axis ratio. Following this adjustment, some filtering of the detected objects is in order.

5.3.2. Particle distribution filter

While the PA program does a remarkable job at detecting objects that pass through the viewing chamber, there are occasions where objects are detected that are non-physical and should not be include in any analysis. Anything with a diameter less than 0.5 mm is removed from the analysis. This is done using the corrected diameters as the cutoff was determined from the lines per inch test reported in Chapter 2. It was felt that below 0.5 mm which corresponds to 5 pixels (where each pixel = 0.1 mm on a side), the minimum resolution of the camera was being closely approached and the ability of the camera optics to accurately discern the particle edge was possibly compromised.

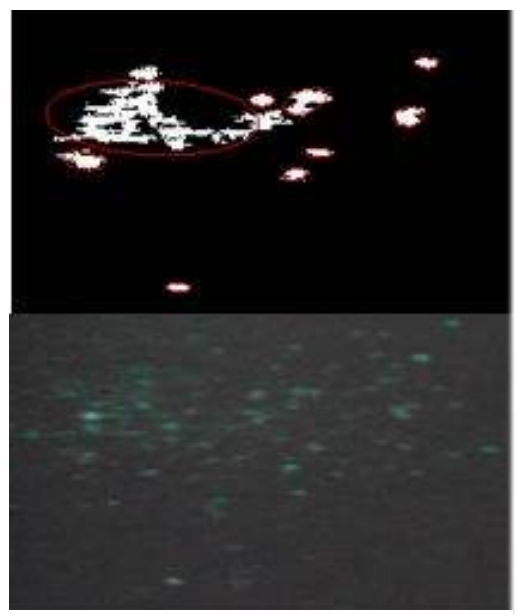

Figure 15. Example image of clustered ice crystals (bottom) and the PA grouped object (top). The clustered object measured 1.32 mm (non-corrected) and had a maximum irregularity of 102.6

Occasionally there are large groups of small detections that the PA program clusters together as a single particle (Figure 15). This occurs most often in the upper

regions of sampled storms where small ice crystals in high concentrations are present. It can also occur if a particle impacts the PASIV intake, causing it to shatter or break apart. Because the particles are so close in proximity, the PA program sometimes groups the small individual objects together and reports them as a single large object (Figure 15). These clustered objects however can have equivalent diameters that are within the range of actual objects, making them difficult to separate from real detections. To detect and remove them, two filters are used.

The first filter makes use of the irregularity of the object. Given the nature of the spacing between the individual objects within the cluster, the fitted ellipse around the cluster contains a large amount of non-brightened pixels. This behavior increases the measured average and maximum irregularity substantially, which can be used to identify these detections. By examining several cases of these types of clustered detections and comparing them with observed particles, a maximum irregularity value of 100 was chosen for a cutoff. Anything with a measured maximum irregularity above this is removed from the analysis. This filter is intended to catch the very clearly erroneous detections.

It is possible however that some large particles, particularly irregular ice crystals, could have real protrusions that result in large irregularity values. While not over 100, these objects can often have maximum irregularities on the range of 40-70, a range shared by some of the cluster objects. A significant difference between these irregular real objects and the cluster detections that have maximum irregularities less than 100, lies in their area ratios. The pixel area of each object can be found by multiplying the number of brightened pixels in that object by the area of each pixel.

This represents the area of the actual illuminated object via its set of brightened pixels. If a ratio of the ellipse area to this pixel area is determined, it is found that real particles tend to have area ratios less than 2 (the ellipse area is usually larger but not by much). The cluster detections have very large ellipse areas filled with numerous small objects and largely dark space, resulting in larger area ratios (the number of brightened pixels is small compared to the ellipse). The second filter looks for objects that have a maximum irregularity over 40 and an area ratio over 2, and removes them from the analysis.

With the construction of the PASIV, the viewing chamber is slightly larger than the actual imaged area. This allows for the possibility that particles could be imaged along the edge of the viewable space, but not completely contained within the viewing volume. The result would be an incomplete description of the particle's size and shape. To account for this, any particles whose radius touches the edge of the image frame are removed (Figure 16). The radius is converted to a pixel value which is then either added or subtracted from the particle origin to determine if the edge of the frame is encountered. Here the non-corrected radius is used as that is the value that relates directly to the pixels in the image frame.

Figure 16. Example of an edge detection. Raw image (bottom) shows a small ice crystal while the PA detection (top) shows the fitted ellipse which touches the edge. The bottom of the ellipse has a sharp line marking the image edge.

5.3.3. Particle classification

After size correcting the particles and removing noise or false detections from the analysis, each particle can be classified. The purpose of this classification is two-fold. First and foremost, it was deemed useful to be able to break the measured size

distributions into individual particle types to determine where various particles exist within a sampled environment. It is also relevant for the purposes of radar reflectivity calculations by allowing various ice particle densities for different types of particles to be used. After examining the camera data manually, four particle types were chosen: rain, graupel/hail, irregular ice crystals, and regular ice crystals. Distinctions between the particles were made by looking for systematic differences between commonly occurring particles, a process similar to what has been done for aircraft observations (Heymsfield and Musil 1982). The Appendix contains a library of various example particles of the different classification types and particularly noteworthy particles.

5.3.3.1. Precipitation particle categories

While the rain category is fairly obvious and straightforward (Figure 17), the illumination and depiction of raindrops within the viewing chamber bears some discussion. As rain drops pass through the viewing chamber, most of the particle will appear as a weakly illuminated sphere. However, the refractive nature of liquid water tends to produce two very bright "lenses" on either side of the drop (top and bottom of Figure 17) which represent the LED arrays within the viewing chamber. This makes visual identification of larger rain drops fairly straightforward. The brightness, size, shape, and relative positioning of the lenses changes depending on the location of the drop within the viewing volume and its proximity to any given light source. As the drop size decreases however, these lenses become closer together and eventually blur into a

Figure 17. Example image of a raindrop, 6.7 mm equivalent diameter. Particle was observed in the May 29th, 2012 case.

single bright illumination source. For the purposes of mixing ratio and reflectivity calculations, the water density value of 1000 kg m^{-3} is used.

Figure 18. Example image of a conical graupel particle, 1.45 mm equivalent spherical diameter. Particle was observed in the May 29th, 2012 case.

The graupel/hail category serves as a hybrid bulk category combining frozen drops, sleet, riming graupel, hail, and the more classical conical graupel (Figure 18). These particles all have a significantly higher ice density than the irregular and regular ice crystal class. The graupel/hail objects themselves are largely spherical, typically conforming to the fitted ellipse quite well. In addition, these objects are bright. The refractive nature of ice tends to scatter light evenly in all directions, resulting in uniformly bright objects within the viewing chamber. It is important to note that these categorizations of the graupel/hail and other particle habits make no direct attempt to describe the microphysical processes through which these particles formed, but rather is a grouping together of visually similar particles. For example, no inference concerning the riming or melting history of a graupel/hail particle can be made other than to note that melting hail typically exhibits sharply defined bright upper and lower edges due to reflection from the light sources by the surface meltwater layer. The bulk density of graupel is likely variable from case to case, and even within a single storm environment. Straka et al. (2000) reported bulk densities of graupel and small hail for their HCA definitions to range between 150 kg m^{-3} and 900 kg m^{-3}. For the purposes of mixing ratio and radar reflectivity calculations, a range of particle densities between 300-600 kg m^{-3} was chosen.

It should be noted that while hail is included in the graupel/hail category, the treatment of hailstones requires special attention where they are deemed to be likely. Specifically, the density of hail can be significantly higher than graupel, depending on the growth regime. In regions where accretion of water droplets onto hailstone surfaces results in the freezing of all drops (dry growth), relatively low density hailstones are produced. Conversely, higher or even solid-ice density hail is produced if the accretion rate is such that the stone enters a wet growth regime in which the surface remains wet (Knight and Knight 2005; Knight et al. 2008). Given the presence of hail in the sampled PSDs, this can have a significant effect on the calculated radar reflectivity. Assuming bulk densities as applied to graupel would be unrepresentative of the hailstones falling, and thus would produce an incorrect reflectivity. Unfortunately, the PASIV is not capable of making a distinction between the dry and wet growth regimes (or is capable of providing an estimate of the liquid water present on a melting surface), and thus an assumed bulk density for all hail must be used. Therefore, any instances of graupel classifications which occur at temperatures warmer than 0°C are considered hail. While the overall classification of a potential hailstone remains in the graupel/hail category, a bulk density of 900 kg m^{-3} is used for the purposes of reflectivity and mixing ratio calculations in the special case of ambient temperature $T > 0$ °C. Furthermore, for reflectivity calculations it is assumed that there is no liquid water present either inside or on the surface of the potential hailstone. The degree of melting cannot be determined with current observations. While this assumption is unlikely to be true and would result in smaller than actual reflectivity, the occurrence of hail is

relatively rare in the observations so the effect should be minimal. Instances of the occurrence of hail will be documented in the relevant discussions.

The irregular ice crystal classification serves to identify those ice crystals that have largely non-spherical shapes (Figure 19). These particles are typically large, usually over 2 mm in diameter, and often contain protrusions off the particle. These objects are similar to those shown in Heymsfield and Musil (1982) for crystals and aggregates, though no distinction can be made here regarding the degree of riming. Aggregates of rimed and unrimed assemblages from Pruppacher and Klett (1997) would also fall within this category. The density of ice crystals in general is highly variable (50-900 kg/m^3) and depends on not only the habit but the particle diameter as well (Straka et al. 2000). Given the non-spherical structure and the holes present within the larger ice structure, these particles are assumed to have lower density, which will be allowed to vary between 50-100 kg m^{-3} depending on the case. As with the graupel class, the refractive nature of ice tends to scatter light in all directions making these objects appear very bright in the camera image.

Figure 19. Example image of an irregular ice crystal, 6.73 mm equivalent spherical diameter. Particle was observed in the June 21st, 2012 case.

The final ice category is for regular ice crystals. The purpose of this category is two-fold, the first being to identify the highly concentrated, small spheroidal ice particles that tend to dominate the ice region of most sampled storms (Figure 20). These ice crystals are

Figure 20. Example image of regular ice crystals. Particles were observed in the June 21st, 2012 case.

typically less than 2 mm and have highly elliptical shapes. As with the other ice categories, the refractive nature of ice makes these objects appear very bright in the image frame. This can pose a problem when trying to distinguish between rain and regular ice crystals given the low probability that two small crystals in close proximity could resemble the bright, parallel lenses on a large rain drop. It is also easy to mistake a singular small ice crystal for a small rain drop. In these cases, the air temperature is a crucial factor in determining classification. This class also serves as a catch all for unclassifed ice to some degree. Particles that do not fall into the graupel or irregular ice categories are assigned to the regular ice category as it is clear that they are ice particles. Given the relatively focused particle shape and lack of branching structure, these particles are assumed to have higher ice densities compared to the irregular ice crystals. All particles in this category are assumed to have a density between 100-200 kg/m^3.

5.3.3.2. Random Forest classification method

Now that the potential particle classes are defined, an automated process must be used to evaluate each particle and determine its most likely class. Previous balloon-borne particle imagers that have attempted to classify objects have done so manually, which is possible given their relatively low amount of particle detections. However the PASIV measures upwards of 0.5 million particles on an average flight so an automated process is required. With the PA processing code, a suite of measurements are available for each particle. However, there is no knowledge regarding which metrics are important or where thresholds might exist to distinguish between the particle types. As such, a "random forest" approach was deemed appropriate given the large amount of data (Fernández-Delgado et al., 2014).

The statistical analysis method known as "Random Forest" is an ensemble learning technique that is used for regression and classification (Breiman, 2001). The approach begins by building a large number of decision trees (i.e., the forest) around a training data set of known classification. The decision trees are then applied to a known object to determine its classification. The first tree in the forest is constructed from a random bootstrap of the training data provided, with replacement. At each node in the tree, a random selection of available metrics is chosen on which to make a split in the data. Typically, the number of metrics chosen at each node is equal to the square root of the number of available metrics. The metric and value for each node is chosen in order to maximize the class spread. Each tree is then built by continuing to split the data until all data in the training data set have been classified. This process is then repeated for a specified number of trees using a new bootstrap of the training data for each tree. The result of the forest is a predictor for the most likely classification of an unknown object. Each tree essentially counts as one vote for the object classification, and the class with the most votes is thus objectively selected. The votes that each classification received can be related to a probability of that class (Williams, 2014). This sort of approach has been used for a number of applications in the severe weather community (Gagne et al., 2012, McGovern et al., 2013).

The training data set was comprised of a little more than 650 objects (selected from the 21 June 2012 and 29 May 2012 cases to be discussed in detail in Chapter 6 and Chapter 7), each hand classified into one of the four particle types and approximately evenly split between the classes to avoid the undesirable circumstance of imbalanced training data (Chen et al., 2004). The manual particle classification was effected by

examining the raw image and visually identifying the most appropriate particle category following the descriptions listed above. The metrics used for the classification process were chosen based on features examined when building the training data set by hand (Table 4). For example, the overall brightness of the particle was a useful tool in discriminating rain drops from ice particles, while irregularity was useful for separating the irregular ice crystals from regular ice crystals. The "graph type" metric was a way to ascertain the overall shape of the particle's brightness histogram. It was found that graupel and irregular ice crystals tended to have a double peak structure to their histogram, whereas rain and ice crystals tended to exhibit a single peak in their brightness histogram (Figure 21). By examining the histogram for a secondary maximum, the graph type was set to 1 (0) for the case of 2 maxima (a single maximum) respectively.

Table 4. Classification Metrics

Eccentricity
Irregularity
Max. Irregularity
Diameter
Avg. Brightness
Ellipse Area
Pixel Area
Maj. Axis
Min. Axis
Graph Type
Avg. Brightness/Pixel Area
Ellipse Area/Pixel Area
Ellipse Area/Maj. Axis
Pixel Area – Ellipse Area
Brightness Histogram
Avg. Brightness/Ellipse Area
Temperature

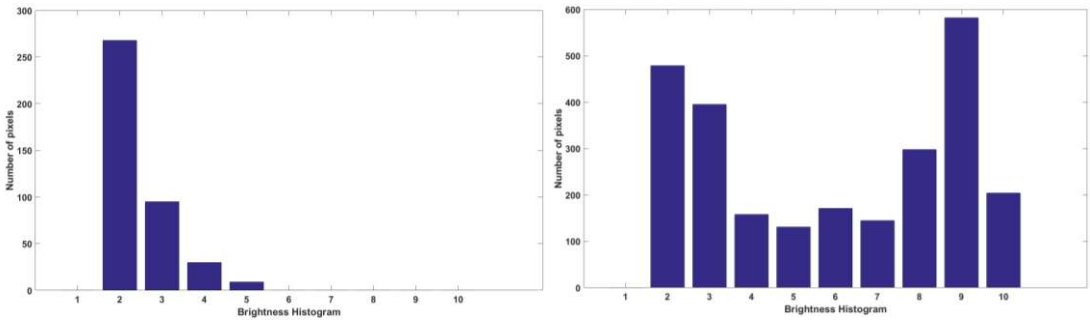

Figure 21. Brightness histogram for a raindrop (left) and a graupel (right) particle. Both particles taken from the May 29th, 2012 case. The raindrop shows a single peak structure (graph type 0) while the graupel particle has a double peak structure (graph type 1).

Once the training data was assembled, it was run through the random forest classification method to build the decision tree forest. The forest itself contained

10,000 trees and used five metrics (the square root of the number of total metrics available) at each node for decision making. Before building the forest, the training data was divided so that two-thirds of the data were used for training while one-third was reserved for testing the accuracy of the forest.

Table 5. Contingency table for the random forest classification. Columns are observed while rows are predicted.

	Rain	Irregular	Graupel	Crystal
Rain	55	0	0	0
Irregular	0	48	0	1
Graupel	2	0	29	1
Crystal	1	3	1	78

The overall accuracy of the random forest technique as applied to these PASIV camera observations was found to be 96%. A 4 x 4 contingency table shows that only a handful of cases were misclassified out of the 219 total testing events (Table 5). The Peirce Skill Score (PSS) of the total random forest approach was 0.9425. Breaking the classifications down into individual class performance allows a more in-depth look at each class. For rain, an overall accuracy of 95 % was obtained with only three events being misclassified and a PSS of 0.9483. The irregular ice crystal class had an accuracy of 94 % with only three misclassifications and a PSS of 0.9352. Graupel showed 97 % accuracy while regular ice crystals were correct 98 % of the time, with only one and two misclassifications and PSS values of 0.9508 and 0.9390 respectively. The excellent results of the classification validation is thus believed to confer a very high confidence in the objective automated process as applied to the entire observational data sets of the two analyzed storms. As will be discussed further in Chapter 6 and Chapter 7, preliminary tests of the automated classification on real data sets yielded results that were consistent

with visual identification and physical expectations. The decision tree forest is saved so that the same random forest may be applied to future data sets without the need for retraining.

5.3.3.3. Classification cleanup

When running a real data set, the main analysis program compiles a list of the metrics listed in Table 4 for each detected particle. The program then runs each object through the classification forest, and the resulting particle class along with the number of votes for each class is recorded. While the classification scheme does an excellent job overall, there are some specific cases where physical constraints needed to be placed on the classification to nudge it towards a more appropriate class.

It is difficult to discern the irregularity of ice crystals with diameters less than 2 mm. As such, any particle that is classified as an irregular ice crystal while having a diameter less than 2 mm is transferred to a regular ice crystal classification.

The other main concern was the classification of particles in and around the melting layer (ML). Given the largely visual aspects of the classification, it was conceivable that raindrops could be detected at altitudes well above the ML or that ice crystals could be found well below the ML. While this did not prove to be a significant problem for the present case studies, an HCA cutoff around the ML for rain and snow (Park et al., 2009) is adopted for these particle classifications to improve robustness in future applications. A size-weighted temperature cutoff was used to slowly nudge particles between the classes. To accomplish this, a trapezoid membership function was created for various particle diameters that essentially weights the likelihood of a particle

class between zero and unity (i.e., where unity corresponds to 100% confidence of the classification and zero indicating no confidence).

Below the ML, particles classified as regular ice crystals are nudged toward raindrops. Larger particles will tend to survive longer in a warm environment, but aircraft observations and HCA studies tend to indicate that ice particles become exceedingly rare by +5°C (Thompson et al., 2014). Therefore all regular crystals are given a membership weight of unity at 0°C, while the drop off to a weight of zero is changed for each of several diameter ranges. Regular crystals with diameters between 0.5 and 0.75 mm drop to a membership weight of zero by 1°C. Particles with diameters between 0.75 and 1 mm extend the drop off out to 2.5°C. For particles between 1 and 1.5 mm diameters the drop off to a membership weight of zero occurs at 4°C, while particles larger than 1.5 mm diameters are extended out to 5°C. The membership weight for rain would be the difference between unity and the membership weight of ice.

To allow some variability in this transition and avoid a sharp cutoff, the confidence of the rain versus ice classification is used. The number of votes the regular ice category received over the total number of votes for the regular and rain categories combined is the confidence that the particle is in fact ice. The confidence that the particle is rain is the number of rain votes over the total between the two categories. In this instance, all particles will have a higher confidence for regular ice as that was the category chosen for classification. For some objects, these confidence values will differ significantly. There are some particles where the classification algorithm put a large number of votes towards that particular class and it was felt that in these cases the

particle should be allowed to "survive" to a warmer temperature. However there are also a number of cases where the classification algorithm was nearly split between the two categories and the regular ice crystal category received only a small number of votes more. To allow for the variability in confidence, the membership weight is multiplied by the confidence value for each class. If the resulting weighted classification value for ice is less than that for rain, the particle classification is changed to rain.

As an example of the above weightings, the membership weighting function of a 1 mm diameter ice particle at 3°C would be 0.25 which corresponds to a 25 % likelihood that the particle is actually an ice crystal. If all of the random forest votes went toward either rain or ice, then the combined votes would be 10,000. It is further assumed that the classification is roughly split, with ice receiving 5020 votes (50.2%) and rain received 4980 votes (49.8%). Following the method outlined above, this would give an overall weighted classification for regular ice of 0.1255 (i.e., 0.502 x 0.25) and a rain weighted classification of 0.3735 (i.e., 0.498 x 0.75). The classification adjustment would therefore push this particle into a rain classification. However, the classification may remain as a regular ice crystal if the classification more strongly favored ice. If for example ice crystal received 8000 votes (80%) while rain only received 2000 (20%), the overall weighted classification for regular ice would be 0.2 and the rain weighted classification would be 0.15. This would lead to the classification adjustment leaving the ice classification. Thus as the temperature increases above 0°C for a given sized object, it requires more and more confidence from the classification trees in the form of decision tree votes for a particle to remain an ice crystal. Graupel

and irregular ice crystals are not evaluated for changing classifications at this time below the ML. Their relatively low concentrations, larger sizes, and physical reasons such as the occurrence of hail were deemed sufficient enough to leave their classifications unaltered.

A similar approach is used for raindrops that are detected at temperatures colder than 0°C. In this instance however, the size dependence is reversed, with smaller objects persisting longer than larger objects. All raindrops have a membership weight of unity at 0°C, but decreases to zero at -5°C, -4°C, -2.5°C, and -1°C for diameter ranges 0.5-0.75 mm, 0.75-1 mm, 1-1.5 mm, and over 1.5 mm respectively. As was the case before, the -5°C cutoff was adopted from previous HCA studies and limited observations (Thompson et al., 2014). Considering the visual characteristics of raindrops, it is possible that the classifier could misclassify either graupel or ice crystals as liquid water depending on the size, shape, and overall brightness of the objects. Therefore, the classification adjustment looks at whether a classified rain drop should be moved to either the graupel/hail or the regular ice crystal class. The membership function for graupel and ice crystals are the difference between unity and the rain membership function. Here the membership function is serving to discriminate rain from ice (regardless of what type of ice), hence the graupel and ice crystal share the same membership weight in this example. Once the membership function is found for each class, the confidence of the classification for rain drops, graupel, and ice crystals are found by dividing the votes for each class respectively over the total between the three classes. As before, the weighted classification is found by multiplying the

membership function for each class by the classification confidence. Whichever weighted classification is higher between the three is the chosen classification.

5.3.4. Precipitation concentration, reflectivity, and mixing ratio

The classification of camera-detected particles forms the basis to undertake the process of computing concentrations and finding radar variables. The particles must first be binned according to some specified sounding layer height increment (depth). This is an important consideration as the concentration requires a defined volume over which to count particles. Choosing too large an integration volume results in overly smoothing the observed data, while too small a volume would increase the likelihood of statistical under-sampling and an over-sensitivity to rare large-particle events that carry too much weight. A typical circular-cylindrical radar pulse volume in the present case studies is on the order of 500 m in diameter, and a similar depth should be used when comparing to radar observations. The user is required to input the integration depth (in m) at the beginning of the program. The altitude from the GPS is then used to build a sequence of layers that correspond to the specified integration depth. The total PSC as well as the major axis and minor axis for each individual particle classification are all binned over this specified layer by adding up the number of particles that fall into each of the 32 size bins. For simplicity and ease in comparisons, the Parsivel bins sizes are adopted for camera data analysis (Table 1). The average pressure, altitude, temperature, dewpoint, and area ratios for each particle type at each binned level are also calculated.

5.3.4.1. Particle size distribution

To determine the PSD over the specified layer, the measured PSC must be transformed via Eq. (3). To do this, either velocity measurements must be provided or

size relations must be used. As there is currently no way to tie velocity observations from the Parsivel to individual particles on the camera, velocity relations are used here. For rain, an air density corrected relation from Gunn & Kinser (1949) is used. For graupel, irregular ice crystals, and regular ice crystals, relations from Böhm (1989) are used (and will be discussed further in 6.2.2. Particle velocity distribution). These relations make use of the class-specific bulk particle densities described earlier to determine the fall speed for each bin of particles. These velocities are then adjusted for the balloon ascent rate and the probability ε is determined following Eq. (2). The PSD is then obtained using the calculated ε and Eq. (3).

Before the PSD can be used to determine radar variables such as radar reflectivity, it must first be filtered. Due to the sampling nature of the PASIV camera, the instrument is sensitive to "rare" events. Large particles that occur only sporadically in the atmosphere that are occasionally sampled by the PASIV can have their concentrations misrepresented. If these abnormal concentrations are allowed to proceed into the radar reflectivity calculations, the resulting values may not be representative of the true environment. To reduce this effect, a noise filter is used to identify and remove outlying bins that have no detected concentrations in any of the surrounding bins. This is done by looking at the previous and next size bins, and the current size bin on the previous and next observation levels. In addition to removing these rare occurrences, a gradient filter is applied assuming that the distribution should steadily trend toward zero after the maximum concentration as particle size increases. Statistically under-sampled concentrations can manifest themselves as larger apparent values, and would produce secondary peaks towards the tail of the distribution. To account for this, the maximum

concentration is found and a value of 25% of that maximum is used as a threshold. Once the concentrations at that analysis level drop below this 25% threshold, any remaining concentrations are forced to zero if their concentration is higher than the previous bin. This effectively removes from analysis any abnormally high concentrations due to under-sampled large particles towards the upper tail of the distributions. Comparisons between unfiltered and filtered concentrations were used to objectively determine where the gradient threshold should be applied.

In performing the calculations for particle concentrations, some measure of uncertainty is useful for determining how accurate the adjusted concentrations are. The largest source of uncertainty in Eq. (3) resides in the velocity assumptions for the binned particles. While the relations used for the various particle classes are widely used and largely considered robust, deviations from this due to changes in density or errors in the size of the particle could lead to variations in the assumed particle fall speed. This would translate into changes in the calculated concentration as the particle fall speed is used to correct the measured number of particles in a given layer.

To demonstrate this uncertainty, a Monte Carlo approach was used where the concentration over a specified layer was repeatedly calculated using a random velocity perturbation. In the simulation, a random, uniformly distributed perturbation of the velocity between +/- 20% was chosen, and the resulting concentration calculated. The perturbation to the assumed particle velocity was applied to each particle concentration equally (all particles received the same perturbation). Using a velocity uncertainty range of +/- 20% represents a “worst-case” scenario and is likely an overestimate for several of the particle types and sizes. Böhm (1989) discussed the uncertainty of their

various particles and only graupel on rare occasions showed a potential uncertainty in the range of +/-20%. The other particle classes such as aggregates were on the order of 5%. This process was then repeated 5000 times with a new random velocity perturbation chosen each time.

The results of the Monte Carlo simulation were then sorted into ascending order for each size bin, and the 95% confidence intervals identified. This range represents the uncertainty in the particle concentrations due to potential errors in the assumed particle velocity. Whenever particle concentrations over specific layers are show, these confidence intervals will be plotted. While this demonstrates the uncertainty present in a single layer, if bootstraps of the mean difference are performed, the results indicate that the average deviation is nearly imperceptible (typical errors of less than 1 m^{-3} per size bin) from the mean concentration.

5.3.4.2. Radar reflectivity

Once the filtered PSDs have been obtained, the radar reflectivity can be calculated from the camera observations. Originally, a simplistic approach using the water-equivalent diameter of each particle was followed. While this method provided reasonable results, some large deviations between the observed and calculated radar reflectivities were noted. Several of the observed particles in the PSD are well within the Mie regime of the radar and thus this approach provided too large of an oversimplification. Instead, a T-matrix approach was used (Vivekanandan et al., 1991, Zhang et al., 2001, Jung et al., 2008, Cao et al., 2010, Jung et al., 2010). The T-matrix calculations provide the scattering amplitude at a given radar wavelength for particles of rain, hail, graupel, or snow types for various assumed bulk densities. Axis ratios of 0.75

are assumed for all ice particles. The calculations include an option to specify the degree of melting for hail and snow at 5% increments between 0% and 100%. While this would provide a more accurate depiction of the particles in and below the ML for radar analysis, it is presently not possible to determine the liquid water fraction of melting ice particles from the PASIV camera observations. Therefore the possible liquid water fraction is presently neglected for all ice particles. To determine the horizontal radar reflectivity we employ the expression

$$Z_h = \frac{4\lambda^4}{\pi^4 |K_w|^2} \sum |f_a|^2 N_D dD, \tag{7}$$

where Z_h is the horizontal radar reflectivity, λ is the radar wavelength, $|K_w|^2$ is the dielectric factor for water (0.93), f_a is the horizontal backscattering amplitude provided by the T-matrix calculations, N_D is the concentration of particles (m^{-3} mm^{-1}), dD is the bin spacing, and the summation is taken over all available particle sizes. To obtain the reflectivity for regular and irregular ice particles separately, the T-matrix calculations for snow were run using the assumed bulk densities described earlier in 5.3.3.1. Precipitation particle categories. A combination of these two categories was also done to provide a single "snow" category. Each classification category has its own reflectivity calculated, as well as the total reflectivity of all particle types combined.

5.3.4.3. Mixing ratio

As a final step in the camera analysis section, the total mixing ratio of each precipitation particle type is obtained according to the following procedure. The product of the volume of a particle in each given size category multiplied by the assumed bulk density of that particle type determines the particle mass. By multiplying the mass per particle by the number of particles of each type in each bin and summing

the individual masses, the total mass for each particle type in each analysis layer is determined. The total particle mass for each particle type divided by the mass of dry air sampled is the mixing ratio of that particle type within each analysis layer. As with the radar reflectivity calculation, separating ice crystals out into irregular and regular types is an additional step beyond the simpler conventional bulk parameterization approach in which all precipitating non-rimed ice particles are referred to as "snow". Hence to compare with the latter simple bulk snow parameterizations, the individual irregular and regular ice crystal mixing ratios are also combined to yield a snow mixing ratio for comparison with model-derived values.

It should be noted that the mixing ratios found here are determined using the binned concentrations which assumed equivalent spherical volumes at the central diameter of each size bin. If feasible, a more accurate and detailed approach could be to factor the actual sizes of individual particles as an alternative to the present assumption of the spherical volume corresponding to the bin center. As the binned concentrations are used for reflectivity calculations, it is expedient to simply use the binned counts to calculate mixing ratios. The latter simpler approach also facilitates direct comparisons to model results, which are also using binned concentrations rather than individual particles.

5.4. Main program: Traverse

The final step in the combined analysis program is to bring in data from gridded radar-based analyses. As one of the many applications of the PASIV's detailed microphysics measurements is comparison with radar, it was deemed necessary to retrieve radar information at the balloon's location. For any radar case the traverse

program uses the balloon's GPS location to prescribe its time and space position with respect to the radar analyses, and retrieve the analyzed reflectivity and other variables including vertical velocity (and if needed the differential reflectivity). Only reflectivity is being examined for comparison with the PASIV at present. A time series of single-radar analyses was available for the 21 June case discussed in Chapter 6, while a time series of triple-Doppler analyses including vector wind and reflectivity was available that combined several DC3 mobile radars in the 29 May 2012 case to be discussed in Chapter 7. A diabatic Lagrangian analysis (DLA; Ziegler 2013a,b) was also performed for the 29 May case which provides time-dependent, 3-D fields of rain, snow, and graupel/hail mixing ratios for comparison with equivalent camera-derived quantities. The DLA algorithm diagnoses rain and graupel/hail mixing ratios and concentrations from the radar-analyzed reflectivity assuming appropriate two-moment inverse-exponential size distribution functions with prescribed intercept parameter values. The Traverse program again employs the location and time of the balloon observation to retrieve the correct co-located DLA output variables.

With this final step, all available data sets are now loaded, corrected where necessary, classified, and required derived variables calculated. This concludes the data processing and manipulation, and allows for analysis to begin. Though several data sets exist for the PASIV instrument spanning a wide range of observable conditions, focus will be on two specific cases during the Deep Convective Clouds and Chemistry (DC3) field campaign. The first case sampled a large multicellular complex of rather weak convection with weak-moderate updrafts and an expansive stratiform precipitation shield on 21 June 2012. The 21 June case serves as a rather benign test case of the full

PASIV instrument and will be discussed first. Individual sections dealing with the Parsivel and the camera separately will be presented, followed by a comparison of the Parsivel and camera analyses. These comparisons will highlight the ability of the PASIV instrument to collect high spatio-temporal observations from two independent sources and serves to provide confidence in the camera data set. The second case was a strong, tornadic supercell sampled on 29 May 2012 and demonstrates the ability of the PASIV to collect data in volatile conditions.

Chapter 6

21 June 2012 – DC3

6.1. Overview

The first case for analysis is an early morning deployment to sample weak, pulse-type multicell storms on 21 June 2012 during DC3. The morning of 21 June was characterized by a moist boundary layer below weak and variable flow through the entire troposphere (Figure 22). Mixed layer parcels attained only minimal convective available potential energy (CAPE), and were required to ascend through a deep layer of inhibition before reaching their level of free convection (LFC). Given the minimal instability, any updrafts that did form would not be expected to support large, high-density rimed ice particles. At the surface, a weak cold front was pushing south through the area, providing a lifting mechanism for the moist surface layer to promote convection initiation. As the front pushed south across the central Oklahoma region throughout the

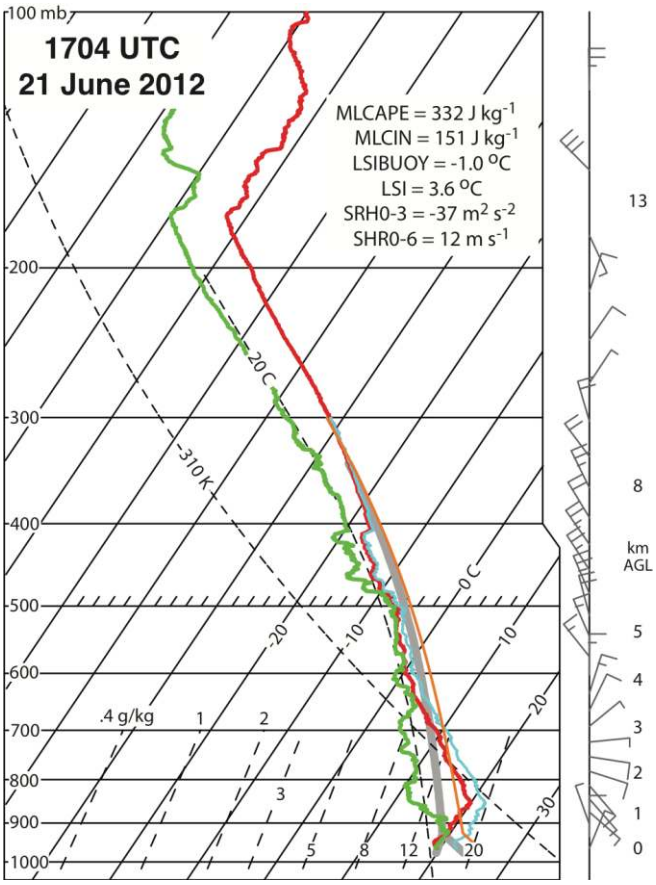

Figure 22. PASIV sounding at 1704 UTC on 21 June 2012.

morning, an area of weak, widespread, multicellular convection broke out and DC3 operations were commenced.

The ballooning team deployed from the NWC in Norman, OK and found a launch site near Binger, OK. At approximately 1704 UTC (all times are Universal Time), an instrument train consisting of a full PASIV instrument, a radiosonde, and an EFM was launched into the weak deep convection (Figure 23). The launch conditions for this case were relatively benign with light stratiform rain falling, making the physical launch of the balloon straightforward. Given the relatively weak conditions expected, the version of the PASIV that included the Parsivel with the videosonde was used for this flight as the chance of a successful launch and recovery was high. The instrument train rose through the storm complex completely, topping out at a maximum altitude of 18.7 km and a minimum pressure of 72 mb. During the flight the Parsivel unit sampled over 316,000 particles, with several 10 s periods exceeding 4000 particles. The videosonde camera detected slightly less than 518,000 objects through the same layer, with several images having more than 60 objects per image.

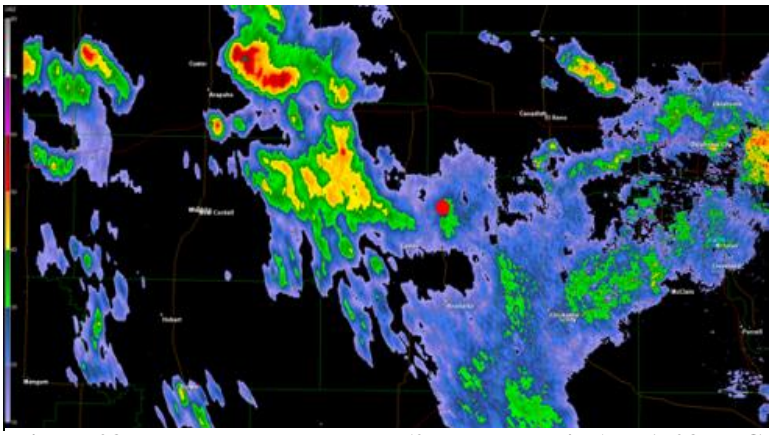

Figure 23. KTLX radar base scan (0.5 deg elevation) at 1703 UTC during the 21 June 2012 DC3 weak pulse storm case. The radar data is displayed using the Gibson Ridge (GR) Level 2 Analyst program. The approximate launch location of the PASIV at the time of the radar scan is marked by a red dot.

6.2. Parsivel observations

6.2.1. Total particle size count

The Parsivel-derived PSC indicates a heavy dominance of small particles, less than 1 mm diameter, throughout the entire profile (Figure 24). In the figure, the color fill indicates the number of particles detected on a logarithmic scale, per size bin and per integration period. Given the high particle counts, these layers are integrated over 10 s, which corresponds to a roughly 50 m vertical layer. A prominent tail of larger diameters in the distribution occurs from 6-10 km, with several detected particles larger

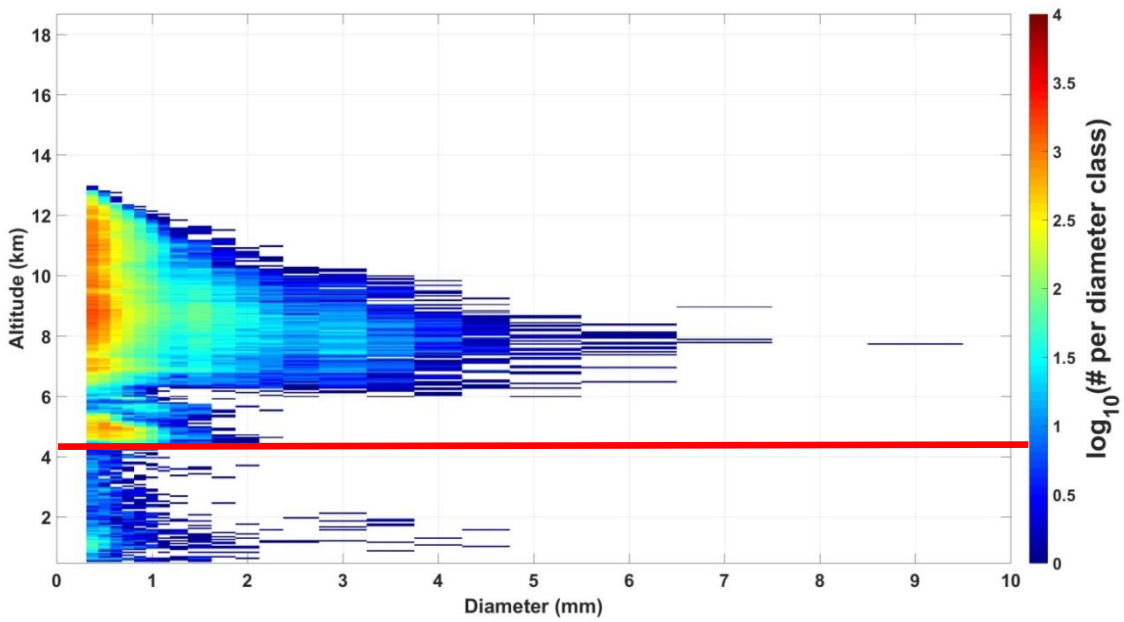

Figure 24. Histograms of total particle size count (PSC) versus height on 21 June 2012 using the Parsivel data. Large tail in the distribution occurs near 8 km, with a secondary maximum near 5 km. The melting layer (0°C isotherm) is indicated by a heavy red line. Color indicates the number of particles (on a logarithmic scale) per size bin, for 10 s layers.

than 6 mm in diameter. A secondary maximum in the distribution occurs near 5 km, immediately above the 0°C isotherm indicated by the heavy red line in Figure 24. This secondary maximum is likely caused by aggregation and the onset of melting as particles approach the ML. The liquid water present on the ice structures leads to

particle sticking and larger average particle sizes (Hosler et al., 1957; Stewart et al. 1984).

Given the relative minimum in particle concentration around 5.5km, it appears that the larger particles sampled aloft do not survive their descent towards the melting layer. This could be an indication of particle breakup, potentially due to ice-ice shattering (Vardiman 1978; Heymsfield and Musil 1982; Yano and Phillips 2011). The Hallett-Mossop ice multiplication process could also be playing a role, however this is typically only active with riming conditions in the -3°C to -8°C range (Hallet and Mossop 1974) and this particular layer was closer to -10°C and likely not actively riming. However, any process involving the breakup of ice particles would tend to eliminate the larger particles in favor of higher concentrations of smaller particles, a behavior that was not observed. Given the vertical nature of the convection, the nearly vertical ascent of the balloon, and the weak upper level flow it is unlikely that the balloon simply missed where these large ice crystals were falling. The latter in turn suggests that if particle breakup was occurring, the ice crystals produced would have been smaller than the observable range of the PASIV (i.e., < 0.5 mm diameter). Considering the in-storm sounding provided by the PASIV flight, it is unlikely that evaporation or sublimation

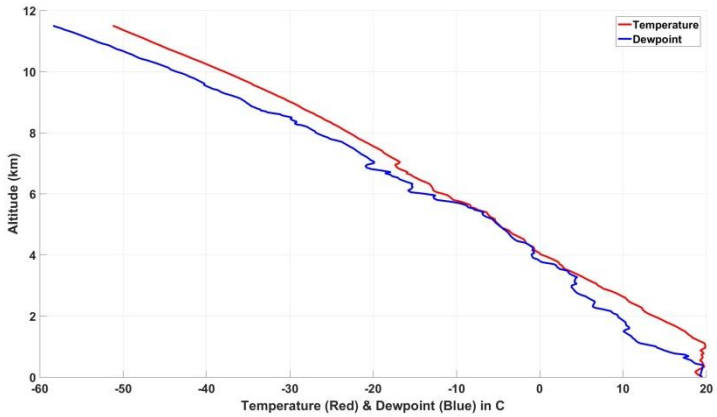

Figure 25. In-storm sounding for 21 June 2012 as recorded from the PASIV flight. Air temperature (red) and dew point (blue) are shown. Profile indicates a nearly saturated environment for most of the profile.

led to the decreased particle counts observed based on the nearly ice-saturated conditions present (Figure 25). A more robust hypothesis regarding the origin of the local minimum in particle counts is under ongoing investigation.

Below the ML, as particles continue to melt and fall speeds increase, a decrease in the size and number of particles detected is evident. As particles melt, they collapse inward towards smaller sizes and their terminal velocity increases, leading to larger spacing between observed particles. This is consistent with previous aircraft observations of decreased particle concentrations immediately below the ML due to gravitational sedimentation (Stewart et al. 1984). As the particles approach the surface however, collision and coalescence processes act to broaden the drop size distribution and several large particles are observed by the Parsivel (i.e., assumed to be rain drops).

6.2.2. Particle velocity distribution

In addition to the bulk particle size measurements from the Parsivel, bulk particle velocity data are also available. The measured velocity is a combination of the fall speed of the particle object and the rise rate of the balloon with respect to still air. While information about individual particles is not provided by the Parsivel, the observations do allow a comparison of the measured particle velocities to various theoretical relations derived for different potential particle types. The ML will be avoided for this analysis due to the lack of distinguishing information regarding particle type. To account for the fact that the Parsivel is moving upwards, any theoretical relations must also be adjusted upwards equivalent to the rise rate of the balloon with respect to still air. Unfortunately, the still-air rise rate is not measured so an approximation must be made.

The Parsivel observations in the rain layer (surface – 4km, Figure 26) show particles increasing in relative velocity from roughly 5 m s^{-1} at diameters around 0.5 mm to approximately 11 m s^{-1} at diameters around 3.5 mm. The color fill in the figure

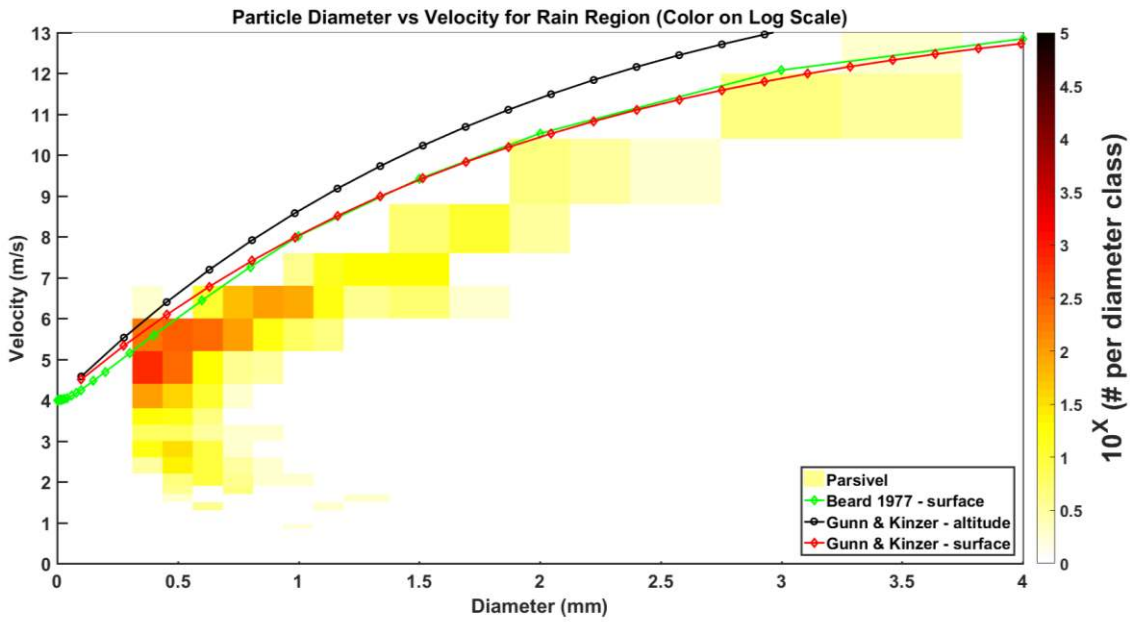

Figure 26. Parsivel measured velocities for the rain layer (sfc - 4km) in 21 June 2012. The color filled scale depicts the number of particles in a given size-velocity bin on a log scale. Also shown are theoretical relations from Beard (1977) and Gunn & Kinzer (1949) that have been adjusted upwards according to the assumed rise rate of 4 m/s.

indicates the number of particles, on a logarithmic scale, for each diameter-velocity bin. For this layer and given the rounded shape of the balloon, a balloon rise rate of 4 m s^{-1} with respect to still air was assumed by averaging the total balloon rise rate provided by GPS over the layer. It was assumed that there were no substantial vertical motions present in the environment and that the reported GPS rise rate was approximately equal to the still air rise rate of the balloon. However, it should be noted that precipitation loading could conceivably cause the balloon rise rate value with respect to still air to decrease locally. These Parsivel relative particle velocity observations appear to agree reasonably well with terminal velocity relations (Beard, 1977; Gunn and Kinzer, 1949) after adjusting to account for the assumed balloon rise rate, although the Parsivel

velocity observations are systematically lower than the theoretical terminal velocities. This could be an indication of a slower true balloon ascent rate than the assumed value, though only in relatively shallow layers since the average rise rate value is broadly consistent with individual values through the depth of the sounding. The velocity relation from Gunn and Kinzer (1949) at altitude has been adjusted using a density correction at the midpoint of the layer from the surface to the melting level, thus variations in air density could account for some of the observed differences as well. It is also possible that a small number of Parsivel-sampled ice particles in various stages of melting are included in the sample, which would account for a slower velocity than that of pure raindrops.

In the rain layer, most of the particles observed fell into smaller size categories with correspondingly slow fall velocities. A handful of larger objects in the range of 4 mm were also detected, but were infrequent. There are a number of detections that occurred in the small size bins with measured velocities that are below the assumed rise rate of the balloon. The latter result would imply that the slow-moving particles were actually rising up through the ascending PASIV particle sampling chamber, which is a physical impossibility. There could be occasional periods during ascent in this layer where the balloon rise rate is slower than the assumed 4 m s^{-1}. Any local transient balloon ascent rate reductions, however momentary, would reduce the relative fall speed of the particles through the Parsivel, and could act to shift those measured values lower on the plot. An alternate explanation could relate to the possible random occurrences of particles following immediately behind one another. If two or more particles were to pass through the Parsivel laser close enough together, it is conceivable

that the Parsivel detection algorithm may not be able to distinguish their individual signals. In the latter event, the Parsivel would tend to sense an elongated residence time in the laser, and thus a slower fall speed. It is also possible that some of these detections occurred at the ground or immediately after launch while the balloon was not at terminal velocity. Regardless, the number of detections observed in this unphysical region of parameter space are small and of little impact on the overall trends in the rain layer.

For the ice region, several smaller layers were chosen for examination to highlight changes in the velocity structure that could reflect changes in the concentrations of various ice particle habits with height. In these layers, several diameter-velocity relations are shown due to the likely presence of a mixture of particle habits. Without any additional information regarding particle type from the Parsivel instrument, it was felt that a suite of potential fall speed relationships at various altitudes within the ice layer would be beneficial for comparison. It is hypothesized that any similarities of Parsivel size-velocity observations to these theoretical fall speed relationships would suggest the likely presence of those particular ice particles. As for the rain region, the velocity relations were calculated using a midpoint of the atmospheric conditions across the ice layer chosen and a balloon ascent rate of 4 m s^{-1} was assumed for each layer.

The first examined layer in the ice region was from 7 to 8 km (Figure 27). The color fill in the plot again indicates the number of particles detected in a given diameter-velocity bin. Since any rimed ice particles in this rather weak, decaying convective cloud likely encountered rather low supercooled liquid water contents at cold riming

temperatures and small impact velocities, two lump graupel calculations were performed using ice densities of 300 kg m^{-3} (black line with diamonds) and 100 kg m^{-3} (black line with circles) using the generalized ice particle fall speed expression of Bohm (1989). These assumed bulk graupel density values are on the extreme low end of the range of bulk densities assumed for various graupel classifications discussed in section 5.3.3. Particle classification, and the associated graupel fall speeds overlap on the fall speeds associated with the low-density irregular crystal classifications. To represent columns, the "Cle" relation from Davis and Auer (1974) was used (blue line). Magono and Lee (1966) defined crystal classifications for nearly 80 crystal types that Davis and Auer and others have used, the "Cle" relation refers to solid bullets. Two relations for plates were used, "Pla" (green dashed line) following Davis and Auer (1974) for hexagonal plates and "P1e" (green line with "x" symbol) for ordinary dendritic crystals from Pruppacher and Klett (1997). The curve "R1d" (black line with "x" symbol) is a relation for rimed stellar crystals from Pruppacher and Klett (1997). Finally, "Agg_{Du}" (red line) is for aggregates of unrimed radiating assemblages of dendrites from

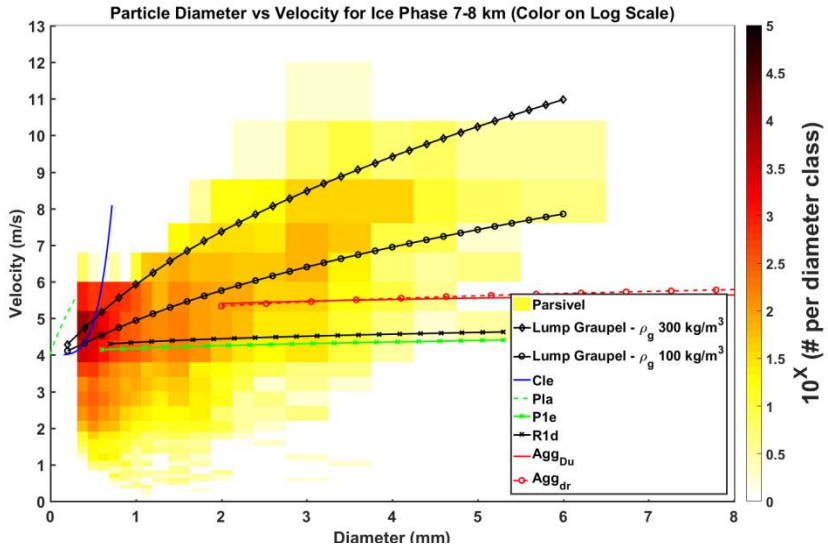

Figure 27. Measured Parsivel velocities for the 7-8 km ice layer with multiple velocity relations adjusted for the assumed balloon ascent rate (4 m/s). The color filled scale depicts the number of particles in a given size-velocity bin on a log scale.

Pruppacher and Klett (1997), while "Agg_{Dr}" (red line dashed line with circles) is for rimed assemblages. All velocity relations have been adjusted upwards using a density correction at the midpoint of the layer.

It is evident from the spread in the velocity data that a large mix of particle types was present throughout this layer (Figure 27). The low density graupel corresponds very well to the upper tail of the velocity data, while the more numerous, small particles appear to relate to the fall speeds of columns. At the larger diameters, several particles are detected that fall within the range of the velocities expected for aggregates. However, there are a number of Parsivel-detected particles that have fall speeds below the 4 m s^{-1} balloon rise rate, a similar behavior to that noticed in the rain layer discussed previously. While much of that earlier discussion regarding these detections applies here, there are some additional factors which may come into play for snow particles. Balloon velocity changes may still be a consideration, however this layer is only a kilometer deep making the latter less of a possibility. A perhaps more likely explanation for the lower velocity tail is the local occurrence of highly elliptical ice particles that are tilted with respect to the Parsivel laser beam. Highly elliptical, canted particles would result in an overestimation of particle fall time through the laser while simultaneously underestimating the maximum dimension, thus reducing derived fall speeds accordingly (Battaglia et al. 2010). Depending on the orientation of the particles, and their ellipticity, the occurrence of highly elliptical, canted ice particles could also affect the measured size. While not a prominent source of error, the potential occurrence of such events would increase with increasing particle concentrations. As in the rain layer, the number of objects detected at 7-8 km is small compared to the total

number of objects detected over the entire layer and thus is not expected to cause significant influence.

Moving up to the 8-9 km layer (Figure 28), a slight difference is manifested in comparison to the 7-8 km layer. The most notable change is not only an increase in the number of particles within each size-velocity bin, but a slight shift towards higher velocities.

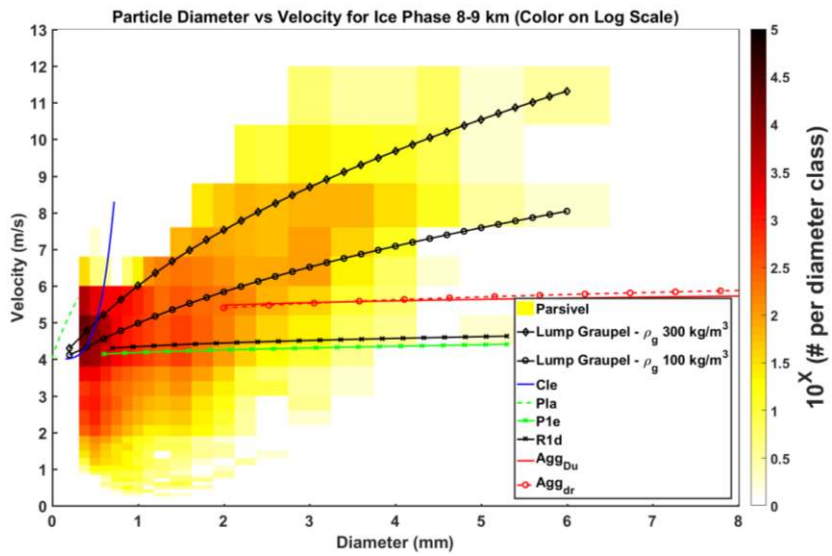

Figure 29. Measured Parsivel velocities for the 8-9 km ice layer with multiple velocity relations adjusted for the assumed balloon ascent rate (4 m/s). The color filled scale depicts the number of particles in a given size-velocity bin on a log scale.

This would tend to suggest the presence of higher-density ice particles, which in turn would have a higher fall speed in comparison to a lower density particle of the same size. The spread in the velocity data generally indicates the continued likelihood of several particle types, including columns, plates, aggregates,

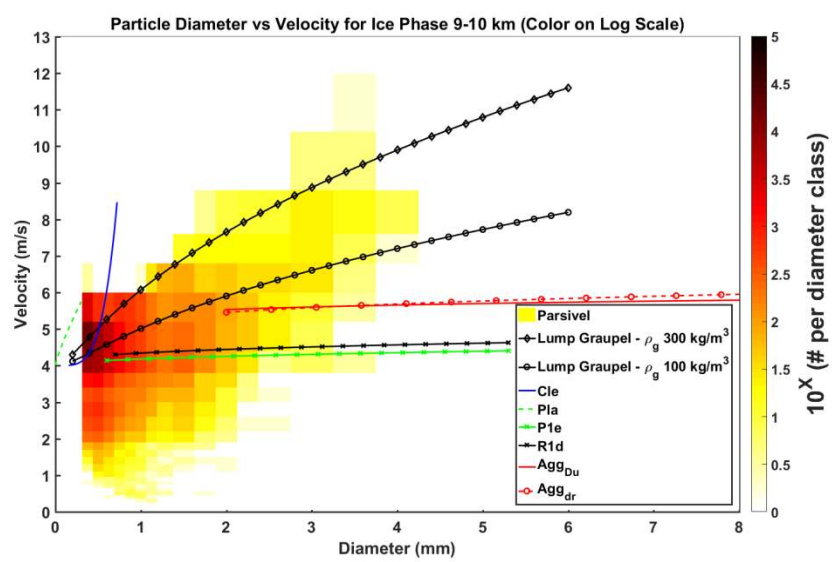

Figure 28. Measured Parsivel velocities for the 9-10 km ice layer with multiple velocity relations adjusted for the assumed balloon ascent rate (4 m/s). The color filled scale depicts the number of particles in a given size-velocity bin on a log scale.

and low density graupel. Furthermore, several particles are still detected with unphysically low fall speeds likely due to the reasons discussed previously.

The 9-10 km layer (Figure 29) has a structure and range that is broadly similar to the 7-8 km layer. While still hypothetically dominated by a mixture of particle types via the broad range of fall speeds of given sized particles, the relative number of particles in the larger size and velocity bins has decreased markedly. This layer, along with the 7-8 km layer, appears to bracket the region of higher bulk ice particle densities that were evident in the 8-9 km layer.

The final layer examined was between 10 and 12 km which essentially corresponds to the top of the storm (Figure 30). A rapid drop off is evident of both the larger particle sizes and the larger fall speeds. The low density graupel type particles have almost entirely disappeared from the layer as gauged by comparison with the graupel fall speed relations, and the remaining particles appear to be largely in the broader class of columns, plates, and stellar crystals. The particle counts of the Parsivel-measured

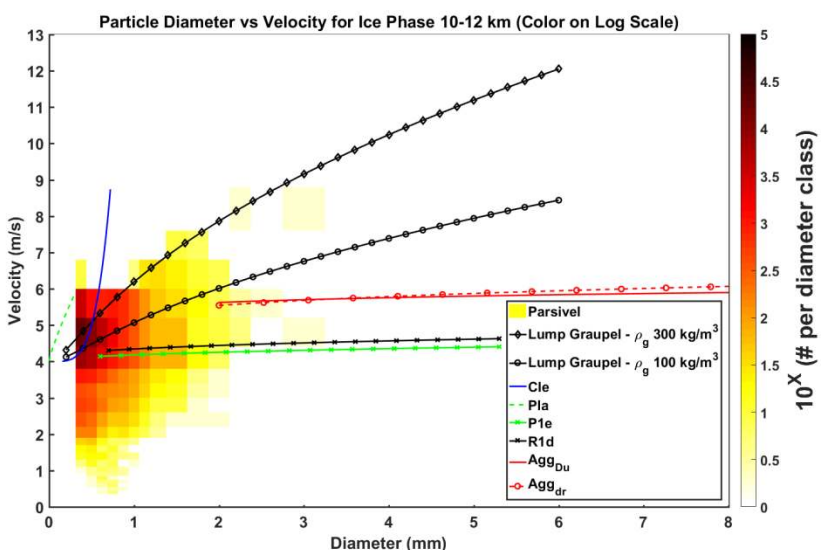

Figure 30. Measured Parsivel velocities for the 10-12 km ice layer with multiple velocity relations adjusted for the assumed balloon ascent rate (4 m/s). The color filled scale depicts the number of particles in a given size-velocity bin on a log scale.

smaller particles are still relatively high, however the distribution is now focused on a small window of particle fall speeds and sizes.

These Parsivel observations appear to be capable of at least broadly confirming several theoretical velocity relations for various ice particles at altitude that span a range of in situ microphysical states. This confidence in the velocity relations will be used later in conjunction with the camera data over the same layer.

6.3. Camera observations

6.3.1. Total and habit-discriminated particle size count

To compliment the PSC provided by the Parsivel (Figure 24), a PSC from the video data is also examined (Figure 31). The camera-derived and Parsivel-derived PSCs display a very similar structure, although the highest overall particle counts have smaller measured sizes in the Parsivel-derived PSC than the equivalent feature in the camera-derived PSC. The upper tail of the camera-derived PSC toward

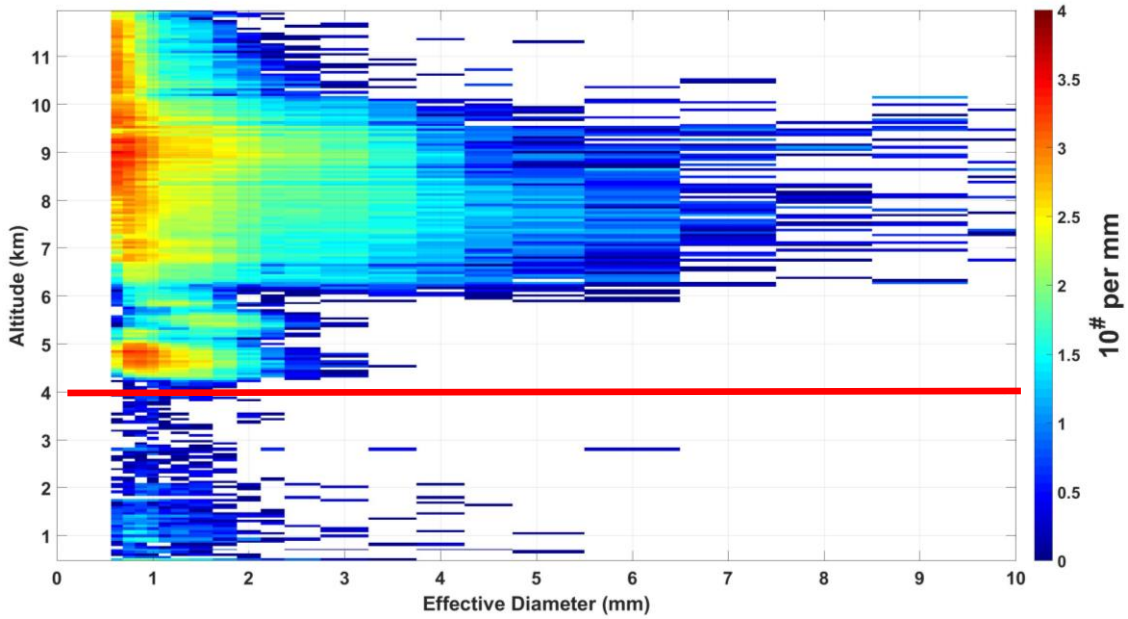

Figure 31. Histograms of total particle size count (PSC) versus height from the camera on 21 June 2012. Color fill indicates particle counts (on a logarithmic scale), per size bin, per analysis layer (50 m). The melting layer (0°C isotherm) indicated by heavy red line.

larger particle sizes in the 6-9 km layer is also evident here, but has broadened considerably with respect to the number of larger particles (> 5 mm) detected. The larger sampling volume of the camera system allows it to more easily detect these large objects. A secondary maximum near 5 km as particles approach the ML is still present, as is the lack of large objects detected in the relative minimum between 5-6 km. This again suggests that the numerous large particles detected aloft do not survive their descent toward the ML. Below the ML, the detected number of particles spreads out as particle melting and increased fall speeds reduce the concentrations there. Similar to the Parsivel data as the distribution nears the ground, the average size of particles tends to increase likely due to collision and coalescence processes.

Another distinctive aspect of the distribution is the rapid shift in the PSD between analysis layers. Most notable is a single layer near 9.5 km where the number of detected particles changes nearly two orders of magnitude in the span of only 50 meters for some particle diameters. Other such layers exist near 7 km, 8.4 km, and 10.2 km. These layers have been visually checked by hand to validate the analysis, and a notable decrease in the number of objects passing through the PASIV during these times is observed. Rapid, large changes in concentration are also qualitatively confirmed by corresponding changes in the frequency of particle impacts on the PASIV's outer skin inferred from the audio record from the videosonde camera. This marks the first storm observational dataset to the author's knowledge in which shifts in total particle counts of this magnitude on spatial scales this small have been documented. Broader analysis layers would smooth out these changes in the distribution and thus would go unnoticed. The implied small-scale spatial heterogeneity

of this type would not be well represented by cloud model microphysical parameterizations or cloud models that typically assume grid cell dimensions exceeding 100 m on a side.

The present analysis shows that the camera-derived PSCs are broadly consistent with the Parsivel-derived PSCs. However, an important and unique advantage of the camera is its ability to distinguish particle habits (Figure 32). The same distribution from Figure 31 is shown in Figure 32, except that separate panels are shown for the camera-derived PSCs of each of the four particle types described in 5.3.3. Particle classification. The ML is clearly evident around 4 km where there is a sharp drop off in the ice phase particles, and below where only rain is detected. Above the ML, there are distinct layers at various heights where different combinations of particle habits are prominent.

Graupel only occurs between 4-6 km within a relatively shallow layer directly above the ML (Figure 32). This is consistent with the anticipated behavior of the low-CAPE updrafts that were not expected to support the growth of large ice particles. In this weak-updraft scenario, supercooled cloud water and moderate-sized, moderate-density graupel would develop through the depth of the convective updraft and reflectivity core of the short-lived convective cells. During the decay stage of the weak updraft, the graupel particles would fall out of the updraft and would likely be confined along with what little supercooled liquid water is available within a relatively small layer near the freezing level as the upper portions of the former liquid cloud and anvil become glaciated and dominated by smaller, lower density ice particles. The latter

hypothesis that the balloon sampled a weak, decayed convective core is consistent with the low height of observed graupel.

Around 6 km, as the relative number of classified graupel particles decreases, there is a marked increase in the number of irregular ice crystals (Figure 32). These low density ice particles increase in concentration through a fairly deep layer before dropping off substantially around 9 km. Throughout the entire layer however, there are large numbers of small ice particles present. These regular crystals have the highest

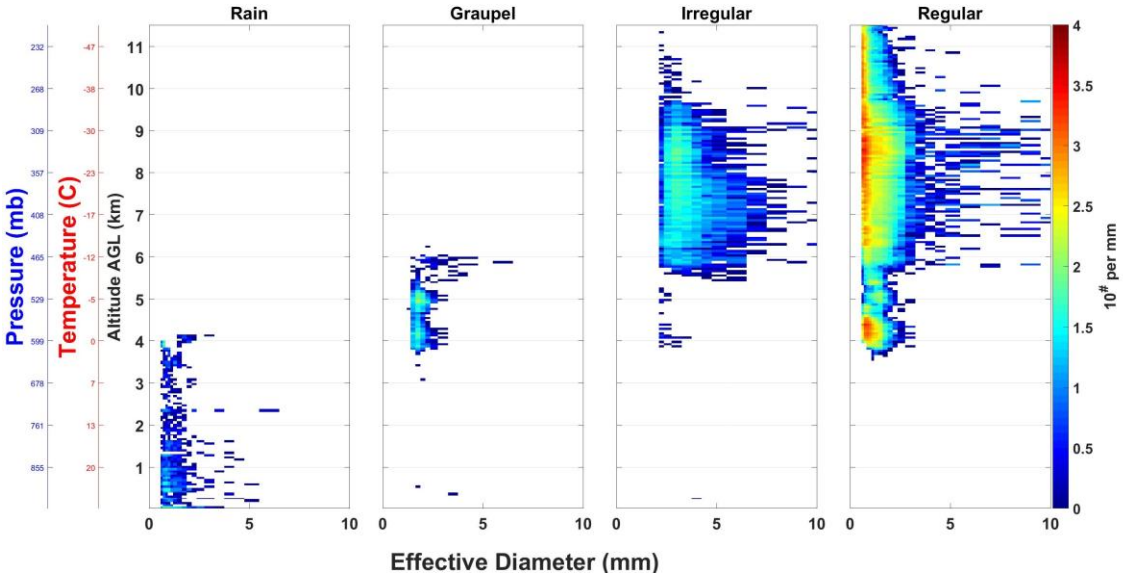

Figure 32. Histograms of individual particle size count (PSC) from the camera on 21 June 2012 showing particle size distribution as a function of altitude, temperature, and pressure according to particle type (rain, graupel, irregular, and regular). Color fill shows number of detected particles, per size bin, per analysis layer (50 m).

counts observed in the entire profile, but are largely concentrated around the smaller sizes (0-5-2 mm). As was discussed earlier, there are sharp changes in the number of detected particles on scales of 50-100 m. The dominance of the irregular and regular ice crystals is broadly consistent with the observations by Heymsfield and Musil (1982), given their particle definitions and limited sampling volumes.

By extension of the PSCs, the particle size distributions (PSDs) may be calculated since the sample volume is known. While the Parsivel provides estimates of particle velocity, there is currently no way to tie these observations to individual particles in the camera data. As such, the theoretical relations outlined in 5.3.4.1. Particle size distribution are used to determine the detection efficiency from Eq. (2) and subsequently the particle concentration (Figure 33). Although the concentrations of graupel and irregular crystals are similar, the regular crystal category consistently contains concentrations approaching 10,000 m^{-3}.

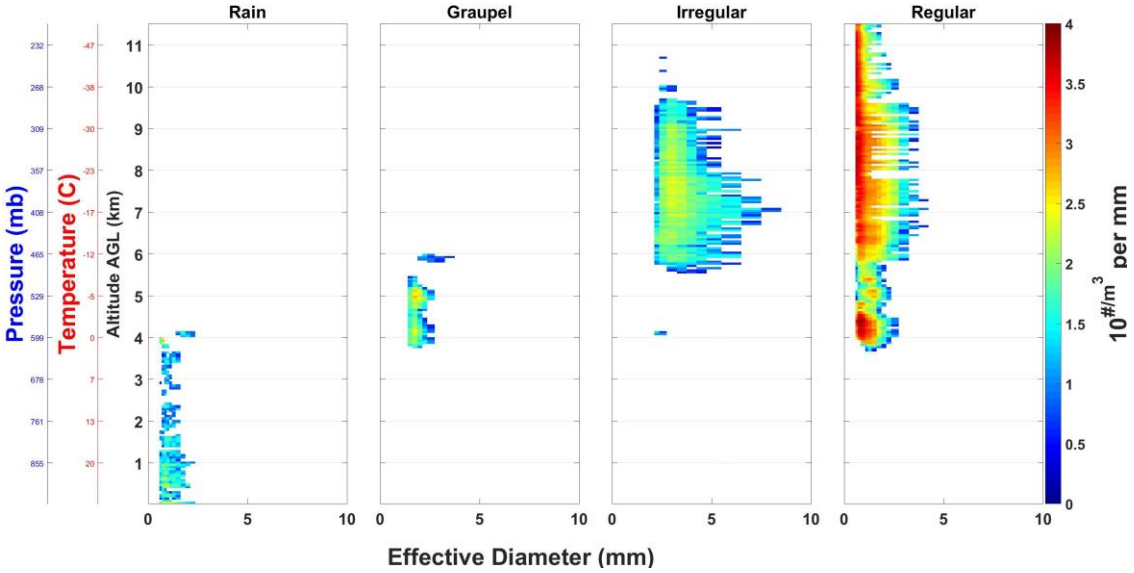

Figure 33. Individual particle size distributions (PSDs) from the camera on 21 June 2012 as a function of altitude, temperature, and pressure according to particle type (rain, graupel, irregular, and regular). Color fill indicates concentration (m^{-3} mm^{-1}) in each 50 m deep analysis layer.

6.3.2 PSD profiles and parametric functional fitting

While examining the particle distribution for the entire storm provides context for various measurements and a semblance of the overall structure, examining the PSDs of individual layers can also be useful. Aside from observing the contributions that various particles make to the total PSD sampled, various single-, double-, and triple-

moment parametric functions may be fit to the data in an attempt to represent the observed distribution with a smoothed parametric functional form. Such smoothed parametric empirical functions are employed by models to represent parameterized microphysics, and comparing the fitted parameter values would provide a check against the equivalent values assumed by model parameterizations.

To develop a conceptual model of the shape of the distribution and how that shape varies with different particle types, several layers in the 21 June sounding will be examined. The first examined layer that was sampled by the PASIV is a 500 m deep layer centered around 0.45 km within the rain layer (Figure 34). In this and similar subsequent figures, the total particle concentration (m^{-3} mm^{-1}) for each

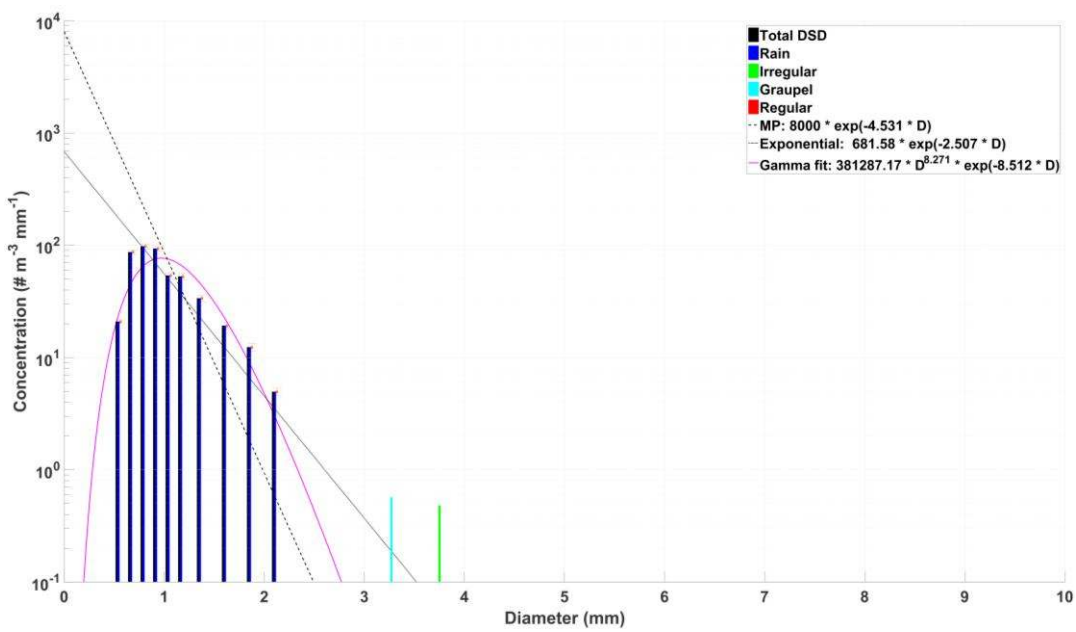

Figure 34. PSD over an approximately 500 m deep layer centered on 0.45 km from 21 June. The distribution shows the total particle concentration in each size bin for all particles (black), rain (dark blue), irregular ice (green), graupel (light blue), and regular ice (red). Also shown are the fitted distributions for the MP (dashed line), exponential (dotted line), and gamma (magenta line) functions. A 95% confidence interval is indicated for the total DSD.

size bin is shown in black while the concentrations of the various particles types are shown in the indicated colors. The distribution is almost entirely composed of rain

drops and represents a straightforward comparison to a distribution that could be sampled by a surface-based disdrometer. There were two detections in this layer that were classified as a graupel and an irregular ice crystal that upon examination do appear to resemble their respective identified classes. This would be an exceptional observation however as it is unlikely that such a particle would survive the decent to such warm temperatures, but for now has been left in the analysis (though not used for fitting purposes). The DSD is clustered around smaller particles and a mean diameter of about 1 mm, with detections ranging between 0.5-2 mm diameter and a peak concentration value of 100 m^{-3} at 0.75 mm diameter.

The camera-derived PSD is usefully fit with various functional representations that as mentioned previously have been used to varying degrees to represent bulk microphysics in cloud models. The classical double-moment (i.e., two variable parameters) inverse-exponential distribution takes the form

$$N(D) = N_0 \exp(-\lambda D) \tag{8}$$

where N(D) is the number of particles per unit volume per unit size interval (m^{-3} mm^{-1}), D is the drop diameter (mm), λ is the slope parameter (mm^{-1}), and N_0 (m^{-3} mm^{-1}) is the intercept parameter (Gilmore et al. 2004a,b; Straka and Mansell 2005; Zhang et al. 2008). A special case of the inverse-exponential distribution with an assumed fixed intercept parameter value of 8000 m^{-3} mm^{-1} is known as the Marshall-Palmer (MP) model (Marshall and Palmer 1948) and has been widely used for rain distributions. An alternate form of the inverse-exponential rain distribution with a fixed intercept parameter value of 800 m^{-3} mm^{-1} (i.e., equivalent to 8 x 10^5 m^{-4}) was developed and applied by Ziegler et al (2010) to obtain a very realistic morphology of the forward

flank rainy downdraft in a simulated long-lived supercell storm. A frequently applied triple-moment function known as the modified Gamma distribution (Ferrier 1994; Ulbrich and Atlas 1998) takes the form

$$N(D) = N_0 D^{\mu} \exp(-\lambda D) \tag{9}$$

where λ is the previously defined slope parameter, N_0 has units of m^{-3} $mm^{-1-\mu}$, and μ is a shape parameter. Given these functional forms and the observed distribution, the Method of Moments (MoM) as outlined in Ulbrich and Atlas (1998) and Zhang et al. (2008) can be used to determine the various fitted parameters for each parameterized size distribution function. The 2nd,4th, and 6th moments are used for the MoM Gamma distribution fitting, while the 2nd and 4th moments are used for the MoM exponential distribution fitting. The MoM fitting of the MP relation uses the 3rd moment for the determination of the slope parameter.

A comparison of the various functional fits to the observed PSD indicates that the three parameter Gamma distribution agrees with the observations quite well (Figure 34). The Gamma distribution fit reproduces the downward trend to smaller sizes both below 1 mm and above 2.5 mm diameter as observed. The exponential distribution matches the mean of the PSD well, but overestimates the observed values for diameters less than 0.75 mm and above 2.5 mm diameters, well above where the observations extend. The MP distribution provides a very poor fit of the PSD due to its unrealistically high assumed intercept.

To determine how these types of distributions change with various particle types, a roughly 500 m deep layer centered around 4.6 km is shown in Figure 35. For the entire distribution, the regular ice crystal classification dominates at every size bin,

with several size bins containing only regular ice crystals. Graupel is only a significant contributor at diameters above 1.5 mm, and irregular crystals are present in low concentrations. This layer corresponds to a level immediately above the melting layer, where the PSD begins to expand rapidly (Figure 31). The distribution itself is rather focused, only spanning a diameter range between 0.5 and 3 mm.

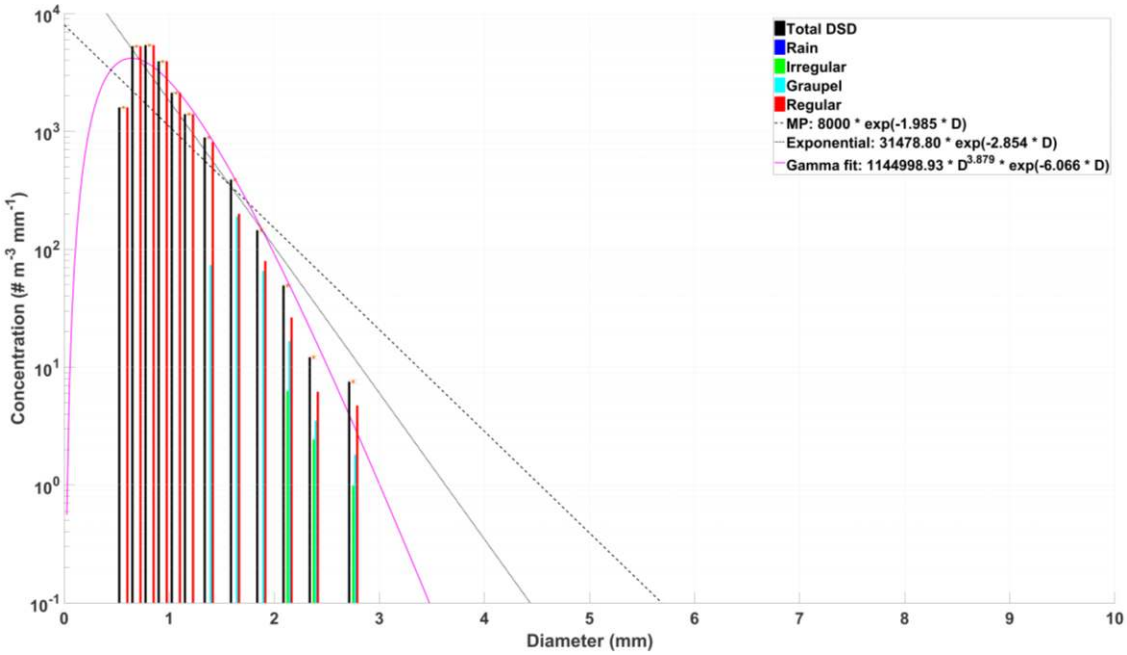

Figure 35. PSD over an approximately 500 m deep layer centered on 4.6 km from 21 June. The distribution shows the total particle concentration in each size bin for all particles (black), rain (dark blue), irregular ice (green), graupel (light blue), and regular ice (red). Also shown are the fitted distributions for the MP (dashed line), exponential (dotted line), and gamma (magenta line) functions. A 95% confidence interval is indicated for the total DSD.

The Gamma distribution again fits the observed data quite well (Figure 35). Both the exponential and MP distributions overestimate the particle concentrations at diameters above 2 mm. The Gamma distribution more closely matches the observations, and also indicates the drop off at the smallest size bins. The MP distribution extends much further than observed towards larger particles and again provides a very poor fit of the observations.

The PSD changes significantly as graupel becomes non-existent and the irregular ice crystals begin to dominate the larger size bin concentrations near 8 km (Figure 36). The highest concentration values have similar magnitudes to the previous layer near 4.6 km, however the shape has changed and is now better represented by an exponential distribution. The three parameter Gamma distribution undercuts the concentrations by as much as an order of magnitude at the smaller diameters, suggesting that a modified MoM Gamma distribution fit with $\mu < 0$ would better handle the high concentrations below 1 mm diameter. The presence of the larger irregular ice crystals

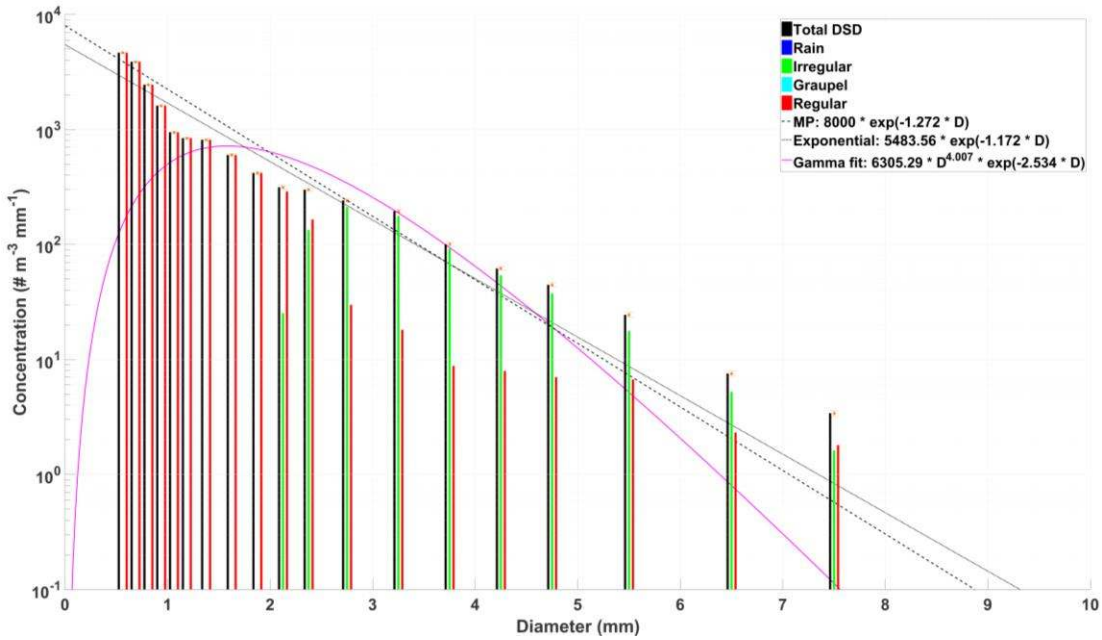

Figure 36. PSD over an approximately 500 m deep layer centered on 8.25 km from 21 June. The distribution shows the total particle concentration in each size bin for all particles (black), rain (dark blue), irregular ice (green), graupel (light blue), and regular ice (red). Also shown are the fitted distributions for the MP (dashed line), exponential (dotted line), and gamma (magenta line) functions. A 95% confidence interval is indicated for the total DSD.

at the larger sizes extends the distribution outward, a shape not well represented by the Gamma distribution. It is interesting to note that the irregular ice particle PSD appears capable of being rather well fitted with a Gamma distribution based on visual

inspection. The MP distribution provides a relatively better fit to the total PSD than was the case for the lower-altitude layers.

Functional fits have been performed for the total PSDs in every layer to characterize the vertical variations in the fitted parameters through the depth of the sounding (Figure 37). Note that the N_0 parameter has different units and magnitudes for the inverse-exponential and MP functions in contrast to the Gamma function. Below 4 km in the rain layer, there is a considerable amount of spread between the three distribution fits. The Gamma distribution in the rain layer consistently maintains the largest λ values which approach 10 mm^{-1} on average. The λ values of the MP distribution in the rain layer are about 5 mm^{-1}, while the inverse-exponential distribution has λ values of about 3 mm^{-1}. For the MP case, the large assumed intercept forces the slope to be rather

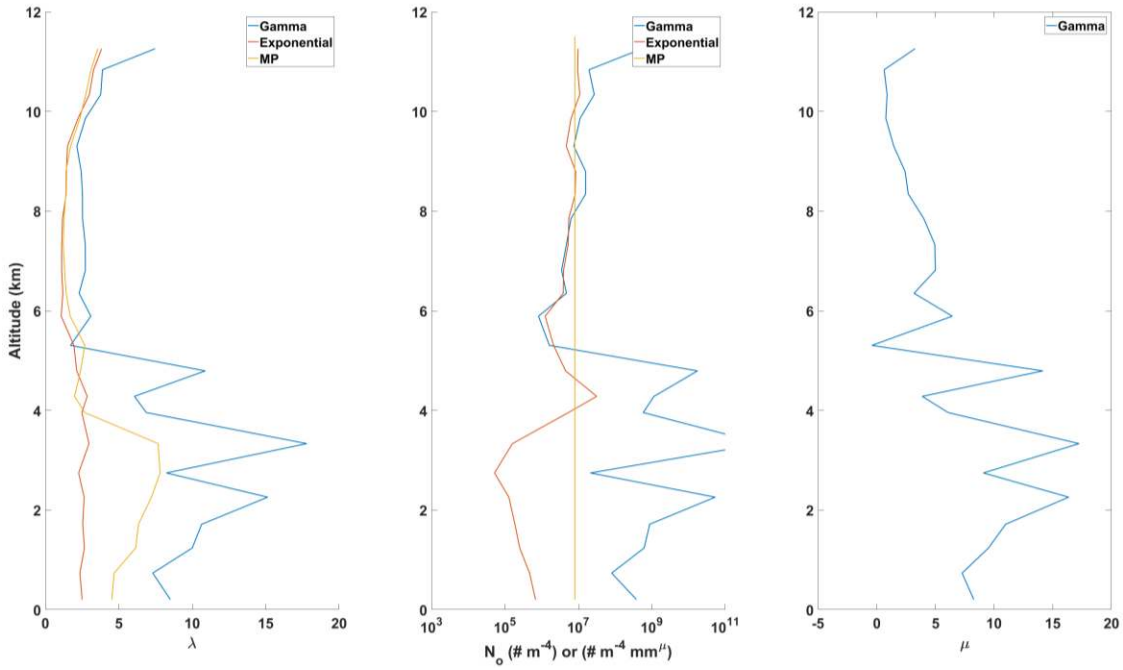

Figure 37. Calculated parameters for the gamma (blue), exponential (red), and MP (yellow) functional fits across 500 m deep layers throughout the 21 June sounding. Parameters were found using the MoM technique.

too steep in the rain layer. Above the rain layer the three distributions converge to a similar inverse-exponential character, with λ values averaging around 1-2 mm^{-1} for nearly the rest of the profile and λ value differences between the relations on the order of 1 mm^{-1}.

The intercept parameter cannot be directly compared between the three relations due to its units for the various distribution functions which are either m^{-3} mm^{-1} or m^{-4} (inverse-exponential and MP functions) or m^{-3} $mm^{-1-\mu}$ for the Gamma function (including the shape parameter μ). To compare against more historical observations and values used in models, the intercept parameters shown here are multiplied by a factor of 10^3 to provide units of m^{-4} $mm^{-\mu}$ for the Gamma distribution and units of m^{-4} for the inverse-exponential distribution (Figure 37). The MP intercept parameter is fixed as part of the MP assumptions to a value of 8 x 10^6 m^{-4}. The inverse-exponential distribution varies slightly throughout the sounding, ranging from 1-8 x 10^5 m^{-4} and one order of magnitude less than the MP relation in the rain layer. The inverse-exponential distribution generally converges to a similar value as the MP function in the ice layer

The Gamma distribution in the rain layer is characterized by values on the order of 10^9 m^{-4} $mm^{-\mu}$ or higher (Figure 37). It should be noted that the Gamma distribution converges identically towards the inverse-exponential distribution for $\mu \rightarrow 0$ as the decreasing μ value forces the power-of-diameter term toward unity. Throughout the rain layer, the shape parameter is generally around 10. However, the shape parameter reduces drastically with values generally below 5 in the ice layer, indicating a tendency for the Gamma distribution to converge towards the inverse-exponential distribution in these data fits for $\mu < 5$. Hence, the Gamma distribution trends toward the inverse-

exponential distribution with increasing altitude in the ice layer. This supports the previous claim that the inverse-exponential distribution appears to be more representative of the observed distributions in the ice region.

6.3.3. Radar reflectivity comparison

The calculation of radar reflectivity from the camera-derived total PSDs facilitates their validation via a comparison with observed radar data. To accomplish this comparison however, the analysis layer for the particle data must be on the same order as the radar observations for a fair comparison. Although the 50 m layer-averaging depth as used in the previous distribution figures is relevant for discussions involving the very finescale microphysical structure of the storm, the PSDs computed with a 500 m layer-averaging depth of the particle data are more representative to the layers the radar is sampling (Figure 38).

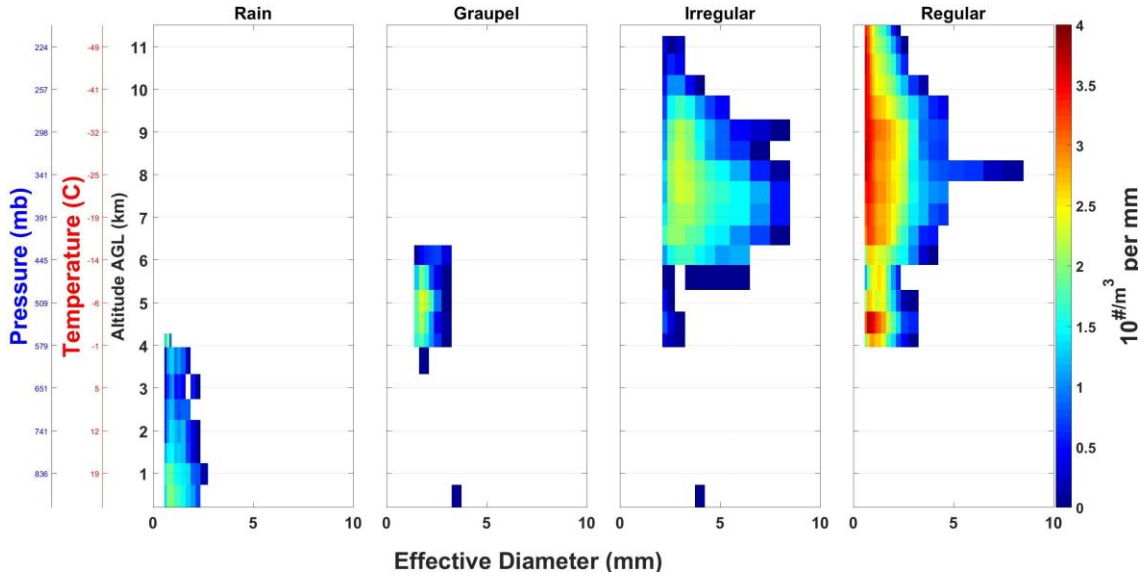

Figure 38. Individual particle size distributions (PSDs) from the camera for each particle type on 21 June 2012 versus altitude, temperature, and pressure as calculated in 500 m deep analysis layers.

The most notable difference between Figure 38 and Figure 33 is the relative smoothness of the PSD profiles assuming a 500 m layer depth. By extending the

analysis layer to a 500 m depth (or approximately 100 seconds of data), a substantial portion of the finescale details observed in the 50 m resolution are smoothed out via the increased layer averaging. In fact, when changing the analysis layer depth, the particle concentrations of graupel move from a single peak structure (500 m) to a double peak structure (50 m). This highlights the importance of layer depth when examining in situ microphysics observations. To compliment the changes in the microphysical structure simply due to integration depth, Figure 39 shows the 500 m layer depth version of Figure 32 for particle size distributions. The differences between these figures is substantial and demonstrates the effect that the integration depth can have on the observed distribution. With the deeper layer, the microstructure is completely smoothed out and the mean particle size is shifted towards larger diameters. Thus integrating over a larger vertical or horizontal scale, as is the case with aircraft, can potentially misrepresent the actual structure.

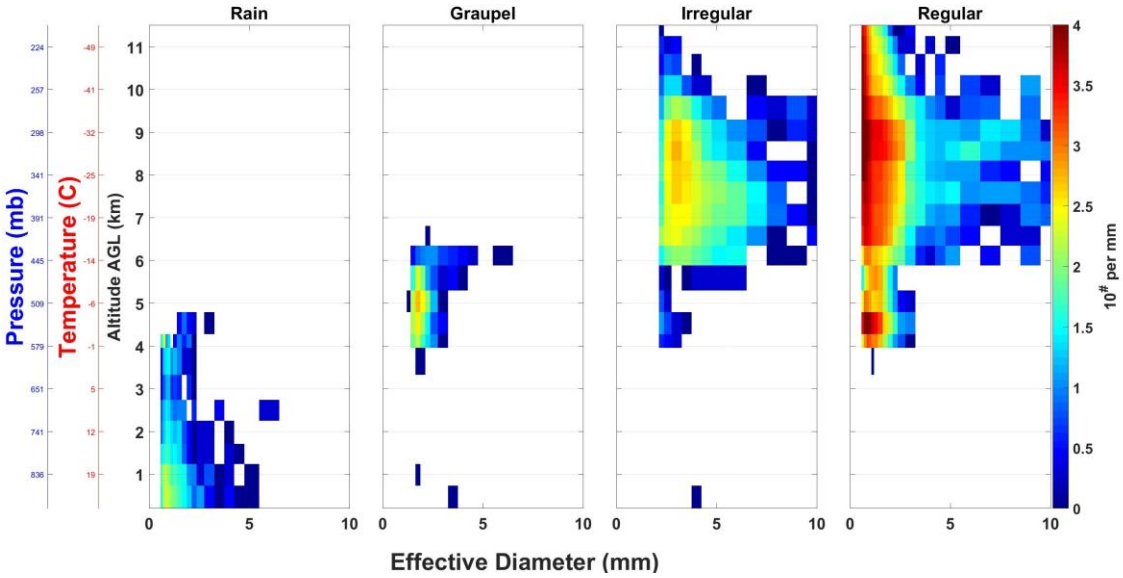

Figure 39. Histograms of individual particle size count (PSC) from the camera for each particle type on 21 June 2012 versus altitude, temperature, and pressure as calculated in 500 m deep analysis layers.

Given these observations, the 500 m layer depth concentrations for the various particle types can be used to calculate radar reflectivity of each particle type (Figure 40). The reflectivity calculation takes into account the particle densities and binned particle concentrations for each respective type, and follows Eq. (7) and the methods outline in 5.3.4.2. Radar reflectivity. The total radar reflectivity can be found by summing the individual radar reflectivities of each contributing particle class. The Shared Mobile Atmospheric Research and Teaching Radar (SR2, Biggerstaff et al. 2005) provided time-spaced volumetric measurements of reflectivity. A sequence of time-spaced SR2 radar objective analyses provided fields of gridded reflectivity at a 500 m grid spacing within a fixed three-dimensional radar volume. As previously described in section 5.4, the radar-analyzed output reflectivity fields were linearly interpolated in

time and space from the radar analyses to the moving Lagrangian point representing the

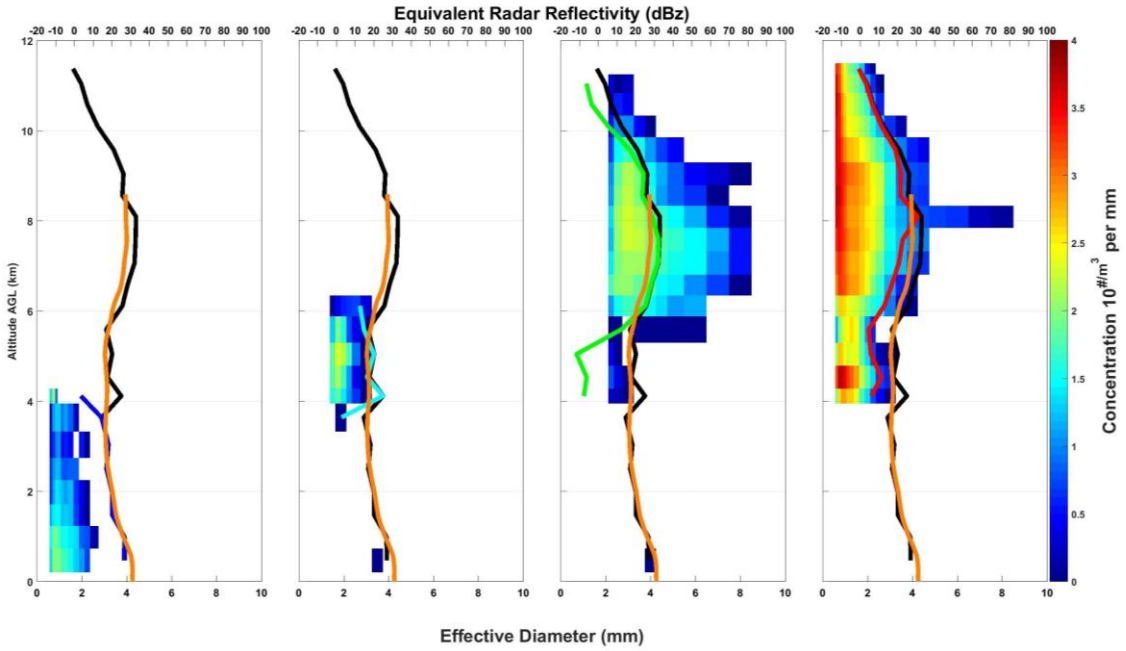

Figure 40. PSDs (m^{-3} mm^{-1}) on 21 June for each particle type with calculated and observed radar reflectivity overlaid. Color fill indicates particle concentration (log scale, m^{-3} mm^{-1}). The orange line indicates the observed radar reflectivity from SR2 during DC3, while the heavy black line is the calculated total reflectivity from the sum of the individual reflectivities of the measured PSDs. The various colored lines in each subplot indicate the reflectivity from that particle classification. Left – rain, left center – graupel, right center – irregular, right – regular.

balloon to facilitate direct comparison with camera-derived reflectivity. Graupel, irregular ice crystals, and regular ice crystals were assumed to have bulk density values of 300 kg m^{-3}, 50 kg m^{-3}, and 100 kg m^{-3} respectively in the 21 June case. In general, the radar reflectivities calculated from the observed PSDs (heavy black line) agree with the observed reflectivities (Figure 40, orange line). Within each subplot, the colored line indicates the reflectivity contribution from each specified particle class (dark blue – rain, light blue – graupel, green – irregular ice crystal, red – regular ice crystal). Throughout most of the profile the calculated values are within a few dBZ of the radar observed fields. Throughout the rain layer, the difference between the observed and calculated total reflectivities is almost imperceptible.

Above the melting layer, there are three distinct periods during which different particles dominate the calculated reflectivity. In the 4-6 km layer, graupel is almost entirely responsible for the observed reflectivity. While concentrations of the regular crystal type particles are significantly higher, the larger sizes and higher assumed bulk density accounts for a larger radar reflectivity. This observation is consistent with previous research which shows that graupel and hail tend to dominate radar reflectivity whenever present (Heymsfield and Musil 1982). Here the PASIV tends to overestimate the reflectivity in some layers compared to the observed SR2 values, likely due to low concentrations of the contributing particles. Because the graupel particles have relatively low concentrations, the PASIV observations may be sensitive to overestimation due to inadequate sampling. Statistically rare particles could potentially lead to overinflated concentrations due to the detection efficiency described by in equations (2) and (3). In general however, the difference between the observed and the calculated reflectivity is generally within ~ 5 dBZ which is consistent with frequently-observed measurement differences between individual well-calibrated radars.

In the 6-10 km layer however, the major contributor to radar reflectivity shifts to the low density irregular crystal types. The relatively high concentrations of particles in the 2-4 mm diameter range, combined with the absence of graupel, contribute to the importance of the irregular ice crystals. Deviations between the calculated reflectivity values from the measured distribution and those observed from the mobile radar are on the order of 5 dBZ, a value well within the range of expected disagreement given the large sampling volume differences of the two instruments.

Above 10 km, the radar reflectivity is largely controlled by the concentrations of the regular ice crystal particles. In the top of the storm graupel is nonexistent and the irregular crystals are in very low concentrations, leaving the high concentrations of the small ice particles to dominate the radar return. Although individually small and of low bulk density, the sheer number of the small ice particles is enough to generate a moderate radar return. However at this altitude, the balloon had risen above the maximum elevation scan of the SR2 radar into its cone-of-silence and thus no reflectivity observations are available for comparison.

There is considerable general agreement between the observations provided by the PASIV instrument and the observed mobile radar analyses. These favorable comparisons provide confidence for the radar observations in an otherwise data sparse area. However, the reflectivity calculations rely partially on assumed values of the various bulk particle densities. Variations of the calculated reflectivity could potentially introduce uncertainty given a different choice in the assumed particle density (Figure 41). In the figure, the shaded areas represent the calculated radar reflectivity using the range of the assumed particle densities for each

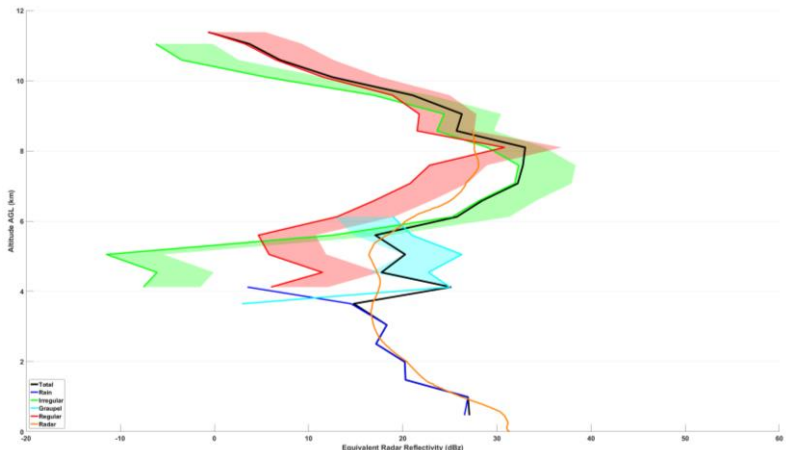

Figure 41. Calculated radar reflectivity from the measured particle distribution on 21 June 2012 showing reflectivity variations due to particle density for the different particle types. Red - regular crystals, green - irregular crystals, light blue - graupel, dark blue – rain.

class. The graupel bulk densities (light blue) are assumed to vary between 300 kg m^{-3} and 600 kg m^{-3}, while the irregular ice crystal (green) and regular ice category (red) densities are assumed to vary between 50 kg m^{-3} and 100 kg $m^{-}3$ and between 100 kg m^{-3} and 200 kg m^{-3} respectively. Rain (dark blue) has a fixed density value corresponding to water. The equivalent values used for the calculations shown in Figure 40 are indicated by the heavy colored lines for each particle type, and the observed reflectivity (orange line) is also shown. This provides an error bar for the calculated reflectivity and demonstrates that the particle densities which produced the most reasonable agreement with the observed radar occurred towards the lower densities for each class.

6.3.4. Precipitation mixing ratio

The availability of camera-derived PSDs facilitate application of the procedure outlined in 5.3.4.3. Mixing ratio, to determine mixing ratios for rain, graupel, irregular ice crystals, and regular ice crystals for the case of 500 m layer averaging depths. Unfortunately, the 21 June case does not currently have independent DLA output fields against which to compare, but the observations themselves are noteworthy in comparisons against the range of values reported in previous research (Figure 42). To assist comparisons with previous modeling studies, mixing ratios are also calculated for snow which is obtained by summing the irregular and regular ice crystal mixing ratios.

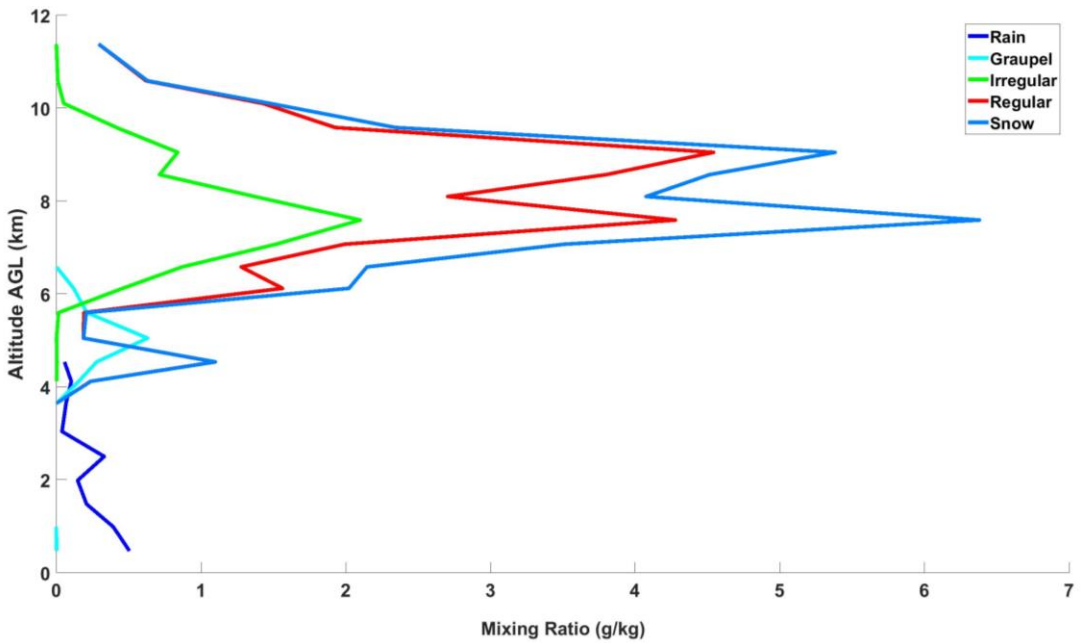

Figure 42. Particle mixing ratios for 21 June 2012 by as a function of altitude. Mixing ratios are shown as dark blue for rain, cyan for graupel, green for irregular ice, red for regular ice, and light blue for combined snow. Analysis was done for 500 m integration layers.

In the layer below 4 km, the mixing ratio for rain (dark blue) is on the order of 0.5 g kg^{-1} (Figure 42). Above 4 km however there is a rapid expanse in the mixing ratio values for snow (light blue), regular ice (red), irregular ice (green), and to some extent graupel (cyan). As was noted earlier, the total number of classified graupel objects was small and confined to a shallow layer, with the maximum graupel mixing ratio of 1 g kg^{-1} near 5 km that corresponded to the maximum graupel concentration of approximately 1000 m^{-3}. In the same layer the regular ice crystals also have a mixing ratio of 1 g kg^{-1}, indicating that despite the lower bulk density their much higher concentration values (10,000 m^{-3}) account for as much particle mass as the much less numerous, larger and heavier graupel particles.

The PASIV enters a region of heavy snow around 5.5 km, where both irregular and regular ice crystals dominate the distribution and graupel particles are no longer detected. The irregular ice crystals vary in concentrations throughout the layer, but

have a maximum mixing ratio of 2 g kg^{-1} around 7.5 km. In this region however, the regular ice crystal particle mixing ratio on the order of 4 g kg^{-1} accounts for the majority of the mass indicated by the total snow mixing ratio (6.5 g kg^{-1}). Thus for much of the sounding above the freezing layer, the smaller and more numerous regular ice crystals control a majority of the particle mass contained in any given layer.

6.3.5. Particle velocity distribution

Given the favorable comparisons of the particle data from the camera and the Parsivel as well as the camera-derived PSD reflectivity to radar observations, there is considerable confidence in both the particle distribution and the particle typing as inferred from the PASIV observations. Since the velocity observations of the Parsivel agreed in a bulk sense with the theoretical relations for various particle types, it is reasonable to apply these relations to the PSDs observed by the camera. The PSDs can be used along with representative velocity relations to calculate a velocity distribution for various particle types using the camera data. For each particle classification, an appropriate velocity relation is used given the particles diameter, and is corrected for the air density at the particle location.

Similar size-velocity distributions from the camera (Figure 43) and the Parsivel (Figure 26) are obtained in the rain layer from the surface to 4 km. The camera size-velocity distribution (Figure 43) has particle diameters that are slightly shifted larger than the Parsivel (Figure 26), but the general velocity structure is similar. The most notable difference between the two distributions is the lack of objects with velocities below the assumed still-air balloon ascent rate in the camera size-velocity distribution.

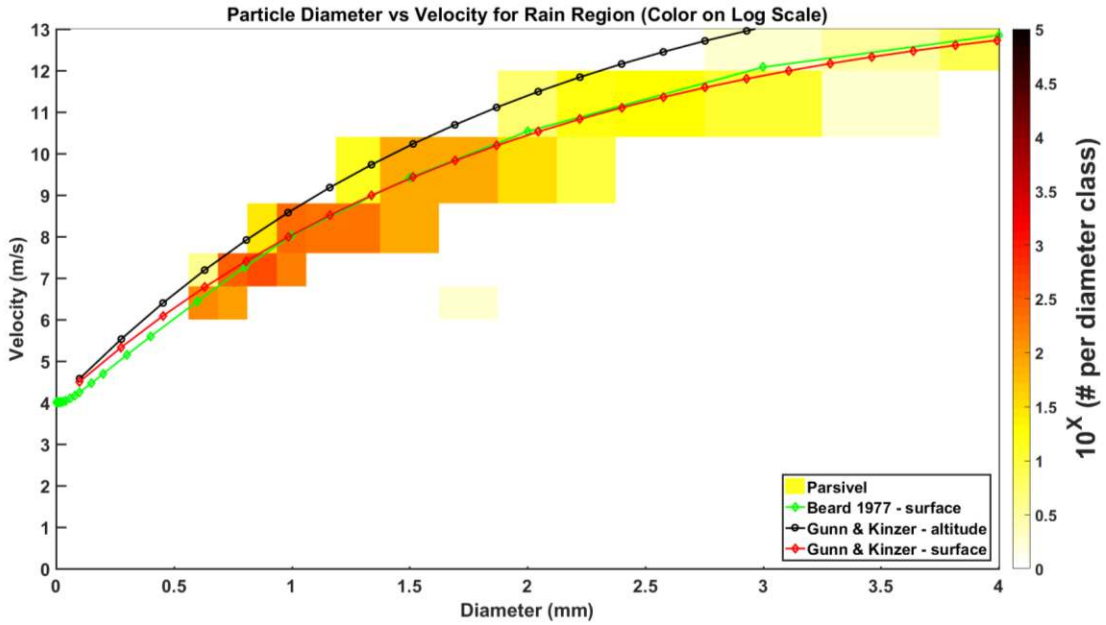

Figure 43. Camera size distribution and calculated velocities for the rain layer (sfc - 4km) in 21 June 2012. The color filled scale depicts the number of particle in a given size-velocity bin on a log scale. Also shown are theoretical relations from Beard (1977) and Gunn & Kinzer (1949) that have been adjusted upwards according to the assumed rise rate of 4 m/s. Velocity was calculated using Gunn & Kinzer (1949).

Noting that the Parsivel was designed to measure spherical liquid particles, there are common previously discussed sampling issues which could cause slower than actual velocities to potentially be measured by the Parsivel. On the other hand, the camera assumes that all particles conform to the theoretical relations and thus does not allow this low-velocity artifact.

For the ice phase region, the camera velocity in the 8-9 km layer (Figure 44) is considerably different compared to the same layer from the Parsivel (Figure 28). While the Parsivel data showed a large spread in the measured velocities, the camera velocities are confined to a narrow series of strips corresponding to the assumed velocity relations. As was discussed earlier, the Parsivel was not intended for use in conditions involving ice particles and contains many artifacts caused by sampling errors. These artifacts are

not present in Figure 44.

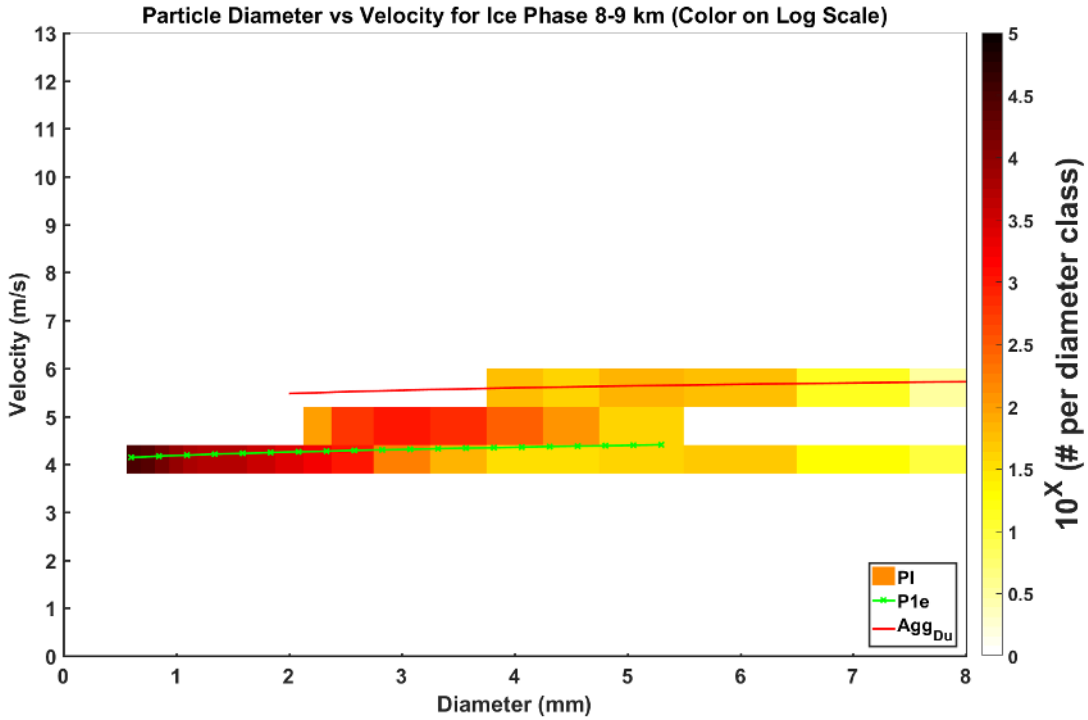

Figure 44. Camera size distribution and calculated velocities for the 8-9 km ice layer with multiple velocity relations adjusted for the assumed balloon ascent rate (4 m/s). The color filled scale depicts the number of particle in a given size-velocity bin on a log scale. Regular crystal velocity was calculated using the "P1e" relation, while irregular crystal velocity was calculated using the "Agg_{Du}" relation.

The 8-9 km layer along the PASIV path does not contain any graupel given the classifications performed on the camera data. Thus all particles fall into either the regular or the irregular ice crystal category. To calculate their velocities, the Agg_{Du} relation from Pruppacher and Klett (1997) was assumed to be representative for all irregular crystals, while the "P1e" relation for dendritic crystals (Pruppacher and Klett 1997) was used for the regular crystal class as well. In the latter case, the regular crystal class likely contains a mix of various particle habits (e.g., needles, columns, plates), but identifying these individual types is beyond the resolution capability of the current PASIV version. A single fall speed relation was instead chosen and it was felt

that the “P1e” relation was representative of the size and velocity range expected for the particles in this class given their behavior when viewing multiple video camera images.

The 7-8 km, 9-10 km, and 10-12 km layers all exhibit similar characteristics to the 8-9 km layer when comparing the camera velocities calculated from theoretical relations to the observed Parsivel data. In general, the Parsivel is not well suited for use in ice phase regions (Battaglia et al. 2010) and the presently observed spread in the measured velocities reinforces the latter finding. The camera data however confines the distribution along the lines of the theoretical relations and provides a robust estimate according to the particle classification made by the camera.

6.3.6. Electric field profile in the context of observed precipitation

Observations from the EFM are also available for comparison with precipitation particle measurements on 21 June. Since it has been well established that precipitation particles typically carry substantial space charges in thunderstorms (MacGorman and Rust 1998), changes in the electric field may be correlated with changes in the particle distribution to help infer the likely roles of the various charge-carrying precipitation particle habits. The profile of the vector electric field on 21 June as revealed by its vertical and horizontal components is shown in Figure 45. Most of the profile is characterized by relatively low electric field magnitudes, with the exception of the 6-9 km layer. Here the largest field values are observed, with a total vertical change of +120 kV m^{-1} in the vertical component between 7 and 8 km. The horizontal components (x – red, y – blue) do not show a major contribution to the vector electric field, and thus the 1-D approximation discussed in 5.2. Main program: EFM is a reasonable simplifying assumption. The vertical component of the electric field (black)

can then be used in Eq (4) to determine charge layers throughout the sounding. These charge layers can be plotted with the particle concentrations of the various identified

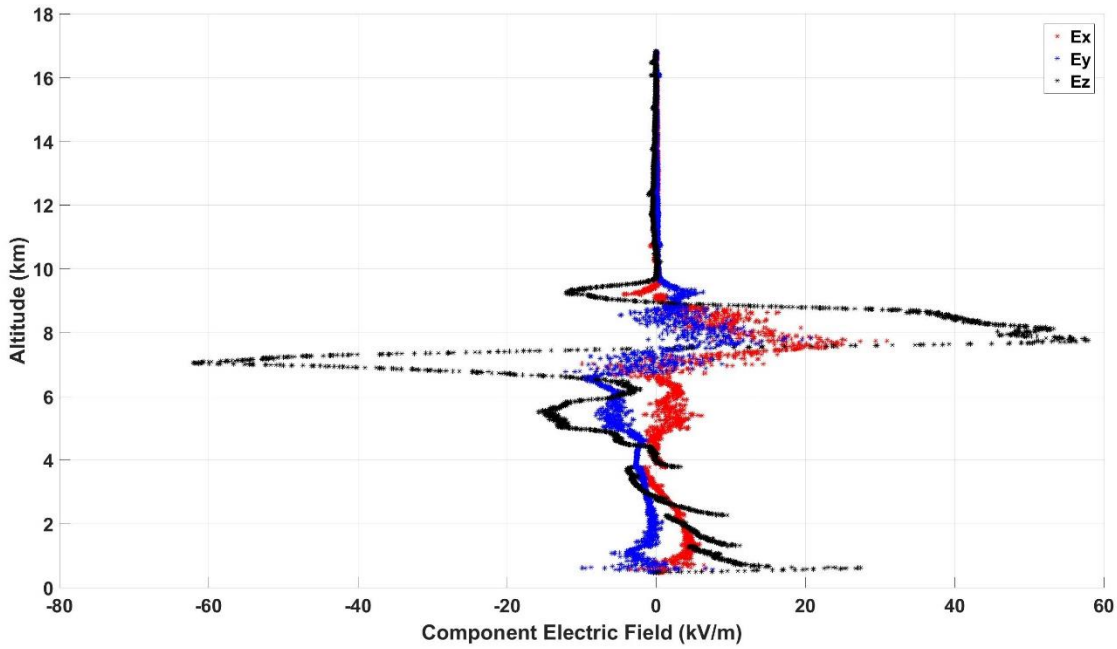

Figure 45. Total electric field profile for 21 June 2012, broken down in to x (red dots), y (blue dots) and z (black dots) components.

particles to determine where shifts in the charge layers occur relative to shifts in the observed particles (Figure 46). The analysis shows that the main region of positive charge lies in the 7-8 km layer, coincident with the large tail of the distribution towards larger particle sizes, and where most of the larger irregular ice crystals are detected. The storm's main negative charge region is located below this layer between 6-7 km. Here the dominant particle type is the regular ice crystal class, though some larger irregular crystals are also present. The final significant charge layer is a weaker negative charge above the positive charge layer between 8-9.5 km, and again is predominantly composed of small regular ice crystals. Given the charge layers observed, an inverted tripolar net space charge structure (Takahashi et al., 1999;

Bruning et al., 2010) is well representative of the storm, although the charge layers are lofted higher than in previously reported research.

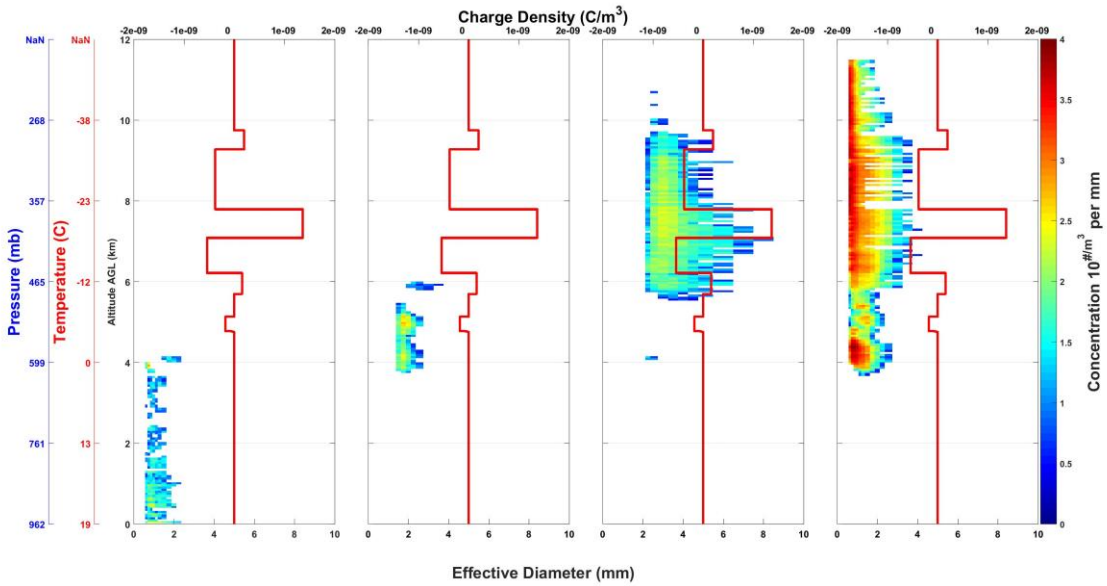

Figure 46. Camera data from 21 June 2012 showing particle concentration as a function of altitude, temperature, and pressure according to particle type (rain - left, graupel – left middle, irregular – right middle, and crystal - right) with charge density (C/m^3) overlaid. Color fill shows number of detected particles, per size bin, per analysis layer (50 m). Charge density (red line) shown on second axis.

The layer directly above the melting layer extending from 4-6 km shows very little observed charge. In this layer there is a small amount of graupel present along with relatively high concentrations of small regular ice crystals, but the lack of significant updrafts likely reduces the available liquid water required for in situ non-inductive charging (Reynolds, et al., 1957; Takahashi, 1978; Saunders, et al., 1991; Saunders, 1993; MacGorman & Rust, 1998; Takahashi et al., 1999). The charge layers observed are likely advected charges from nearby updrafts or remnant charges from a previous cell which likely contained stronger noninductive graupel-ice charging rates during the most intense phase of its life cycle.

6.4 Case Summary

The 21 June 2012 case provides a unique proving ground for the full PASIV observing capability. While relatively benign in terms of severe weather, the weak multicellular convection on 21 June allowed for a complete profile using the PASIV system which was able to retrieve particle size spectra at an unprecedented level of detail. These observations not only highlighted the fine scale heterogeneities present, but were also used to compare with theoretical velocity observations of various particle types and habits, mobile radar observations, and collocated electric field measurements.

With the observations and comparisons made for this case, confidence is high for using the PASIV instrument in a more volatile storm environment. The second case to be discussed is such an environment that occurred on 29 May 2012.

Chapter 7

29 May 2012 – DC3

7.1 Overview

The second analysis case is the supercell Kingfisher, OK storm on 29-30 May 2012 during DC3. A severe weather outbreak in central and northern Oklahoma produced several supercells, along with one tornado, and several reports of greater than 4 inch diameter hail. Throughout the day, a moderate amount of instability developed beneath a warm layer around 3 km serving as a cap for convection until later in the afternoon. As storms intensified, extreme convective instability represented by an MLCAPE of 3154 J kg^{-1} was in place along with a veering wind profile providing a storm-relative helicity in the lowest 3 km of 466 m^2 s^{-2} and a bulk 0-6 km shear of 23 m s^{-1} (Figure 47). A small scale mid-tropospheric short wave rotated over the area in the late afternoon, providing a lifting mechanism for the volatile environment strongly supportive of intense rotating updrafts. Once storms began firing,

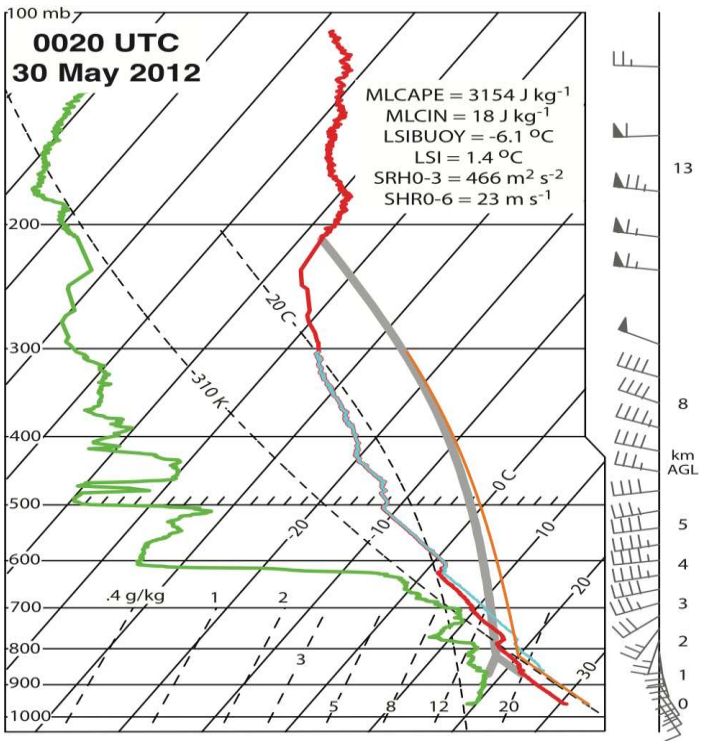

Figure 47. Mobile environmental storm-following sounding at 0020 UTC on 30 May 2012 during the DC3 field campaign operations. Sounding was taken from a NSSL mobile sounding unit in the far field environment of the severe weather outbreak.

the DC3 ballooning crew began operations and deployed from the NWC. At 2323 on 29 May roughly 14 km north of Kingfisher, OK, an instrumented balloon train was released into the forward anvil of the Kingfisher supercell (Figure 48). This launch was the first of two into this storm, and will be the focus for this case study. The Kingfisher supercell was the southernmost supercell in a complex.

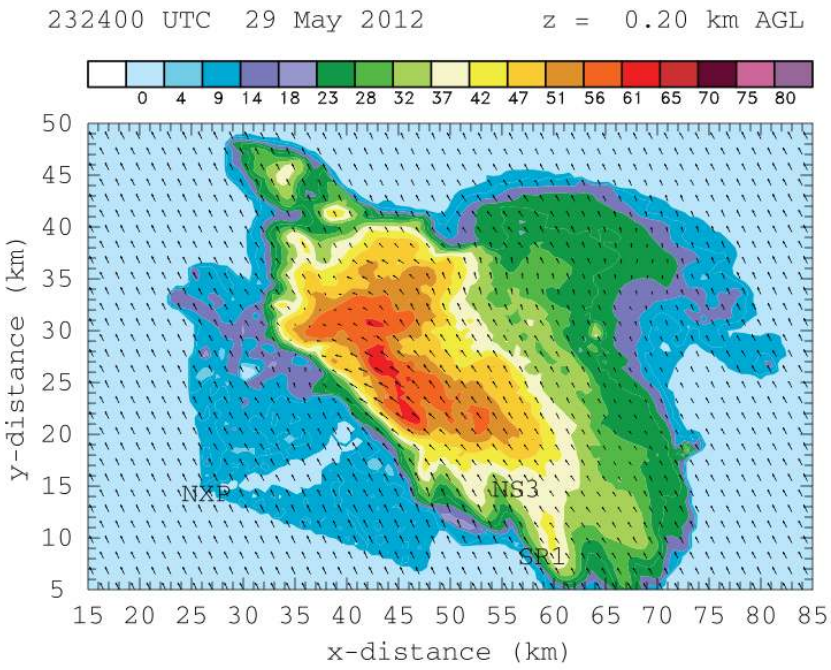

Figure 48. Triple-Doppler analysis at 0.2 km AGL and 2324 UTC for the 29 May 2012. Reflectivity (dBZ) is color-filled while synthesized horizontal wind vectors are scaled to 1 km = 20 m s^{-1}. The launch site at 2323 for the PASIV is indicated by the NS3 location.

Given the severity of the conditions expected on 29 May, it was decided that for this flight a non-Parsivel version of the PASIV would be used. The added weight on the instrument and subsequently larger required helium amounts was a concern for a successful launch. Having a lighter instrument train, with a less rigid filled balloon, was deemed more likely to be successful, particularly given the expected hail. The only data that were not available for this flight were the size and velocity distributions from the Parsivel. The instrument train therefore consisted of a camera-only PASIV, a radiosonde, and an EFM.

After launch, the instrument train ascended through the storm, skirted outside the edge of the main updraft on the east flank of the storm core, and eventually moved out into the left (northern) anvil of the supercell. A radiosonde malfunction resulted in the loss of temperature and RH data above 500 mb. Pressure and location (until roughly 7.3 km) information are nevertheless still available, which allows the vertical placement of the PSD data in the storm. However temperature is a key variable in a variety of processing steps, and so an assumed temperature profile following the dry adiabatic lapse rate of 9.8°C km^{-1} (i.e., essentially the upper levels of a moist adiabat) was used above 500 mb. A maximum altitude of 7.9 km and a minimum pressure of 375 mb was reached before the instrument train was struck by lightning. The lightning strike severed the instrument rigging just above the PASIV, separating the instrument train into two pieces and destroying the radiosonde. Both halves were recovered separately. Data from the ascent portion of the flight prior to the lightning strike will be examined. During this time, approximately 158,000 particles were sampled by the PASIV.

7.2. Camera observations

7.2.1 Total and habit-discriminated particle size count

Despite having the sounding prematurely terminated by lighting, the PASIV was able to measure a substantial number of particles and usefully profile at least part of the microphysical structure of the anvil region of the Kingfisher storm. Initially, there were only scattered detections below the melting layer as shown in Figure 49. As before, an analysis layer depth of 50 m was chosen to reveal any finescale layer structure. A majority of these detections at low levels were clustered around the 1 mm diameter range, but there were also several large detections over 5 mm in diameter. Given the

severity of the storm and the large hail reports associated with it, there was a high a priori likelihood that several of these objects were melting hailstones. Above the melting layer, between 4 to roughly 6 km, a significant absence of particles was detected. This period corresponded to the movement of the instrument train outside of the edge of the updraft and precipitation core of the storm in an area of very low reflectivity as indicated by the triple Doppler radar analysis. The observations were visually checked in the PA program to verify that very few particles were detected in this area of the analysis.

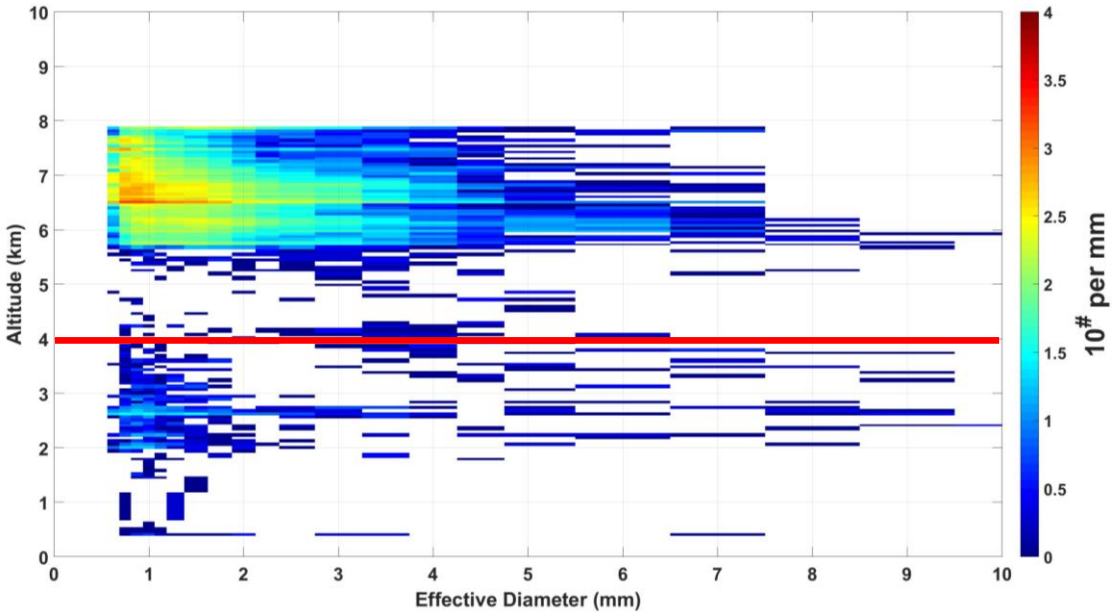

Figure 49. Histograms of total particle size count (PSC) versus height from the camera on 29 May 2012. Color fill indicates particle counts (on a logarithmic scale), per size bin, per analysis layer (50 m). The melting layer (0°C isotherm) is indicated by heavy red line.

At 5.7 km, the instrument train entered the left flank anvil precipitation core of the supercell, and a significant increase in particles was observed. The dispersion of the PSC quickly expanded to include large particle diameters, and a broad height range containing moderate particle counts between 1 and 4 mm was observed. The largest PSC values were confined to the smaller particle sizes with diameters on the order of 1

mm. As observed in the 21 June case, there were several periods in which the number of detected particles changes rapidly between layers. In contrast with the 21 June case, the fluctuations of PSC on 29 May are confined to a smaller range of extreme values. In fact, the entire profile on 29 May contained lower particle counts than in the 21 June case.

Given the environment present, as expected the particle classification on 29 May did indeed identify significantly different particle distributions according to habit compared to the 21 June case (Figure 50). Throughout the entire profile, higher amount

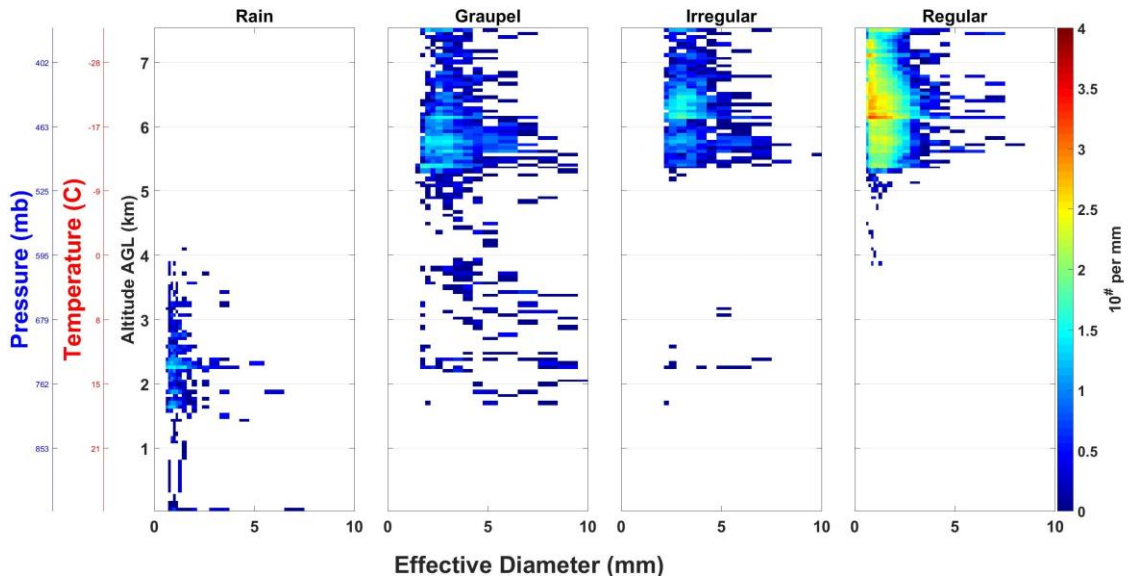

Figure 50. Histograms of individual particle size count (PSC) from the camera on 29 May 2012 as a function of altitude, temperature, and pressure according to particle type (rain, graupel, irregular, and regular). Color fill shows number of detected particles, per size bin, per analysis layer (50 m).

of graupel was present in the 29 May case compared with the 21 June case. Once the PASIV enters the anvil region at 5.7 km there mix of particles detected between all three ice categories for the remainder of the dataset. Although the regular crystals continued to dominate, graupel and irregular crystals showed nearly the same particle counts.

Below both the anvil region and the melting layer in particular, there were a number of detections in the graupel/hail and irregular categories that indicated the presence of large, evidently solid ice particles at temperatures well above freezing. These objects were in fact hailstones as clearly detected by the imager (Figure 51). Given the expected hail as inferred from severe weather reports and also the visually inspected images via the PA program, it was determined that these detections were valid and thus no habit correction was provided for these objects. Their inclusion in the various observed distributions is important for radar reflectivity calculations and comparisons with observed values.

Figure 51. Hailstone observed in the PASIV on 29 May 2012. Diameter was 18.1 mm and the air temperature was 15.5°C.

7.2.2. *PSD profiles and parametric functional fitting*

As with 21 June, the 29 May case presented a unique opportunity to examine both the individual and total PSDs and the associated single-, double-, and triple-moment parametric functional fits to the total PSDs. Given that 29 May contained several layers with distinctly different particle types and concentrations, several specific layers will be examined.

The layer of 500 m depth centered at 2.5 km provided a unique opportunity in that the total distribution contained moderate amounts of rain mixed with several large hailstones (Figure 52). This layer also corresponded to a region in which the observed reflectivity matched the reflectivity as computed from the total PSD (to be discussed in the following section). As the PASIV was well below the melting layer at this point

and as ice crystals thus would not be present, the combined rain and hail particles suggested a bi-modal distribution. The rain DSD spanned diameters in the range of 0.5-2 mm, while the hailstones encountered were concentrated between 3.5 and 9 mm in

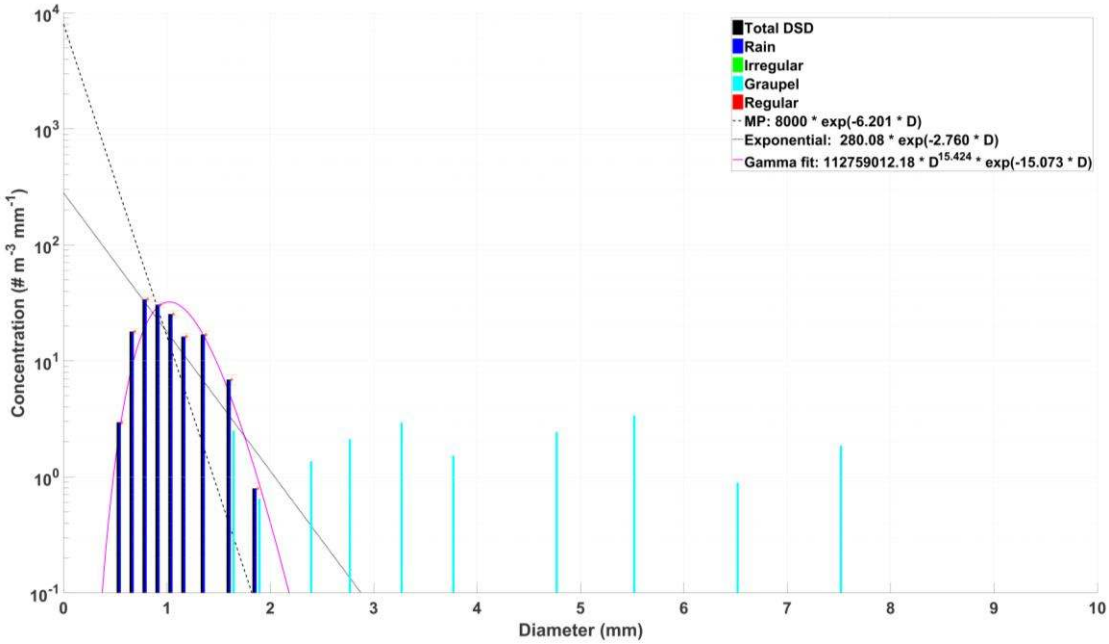

Figure 52. PSD over an approximately 500 m deep layer centered on 2.5 km from 29 May. The distribution shows the total particle concentration in each size bin for all particles (black), rain (dark blue), irregular ice (green), graupel (light blue), and regular ice (red). Also shown are the fitted distributions for the MP (dashed line), exponential (dotted line), and gamma (magenta line) functions. A 95% confidence interval is indicated for the total DSD.

diameter (though the added presence of several larger stones is noted). Since the hypothesized bi-modality of the distribution would need to be qualified due to the low concentration values associated with the hailstones and the likely rather qualitative nature of the estimated hail concentrations, the model fits for the single-, double-, and triple-moment prediction equations were restricted to the rain DSD only. Of the three fits, the three-parameter Gamma distribution was determined to most closely match the observed DSD. The MP and generalized inverse-exponential distributions both failed to capture the sharply decreasing drop concentrations at diameters below 0.75 mm. If the hailstones were included in the MoM calculations, the Gamma function did not well

represent the observed data (not shown). The latter biased Gamma fit to the total PSD in the rain layer was likely caused by increased sensitivity to the low concentration values at the larger diameter sizes from the hailstones.

The layer centered at 5.75 km, being above the melting layer, showed a mixture of graupel, irregular ice, and regular ice with varying relative contents (Figure 53). Among the smaller particles (0.5-2 mm diameters), the regular ice crystals tended to

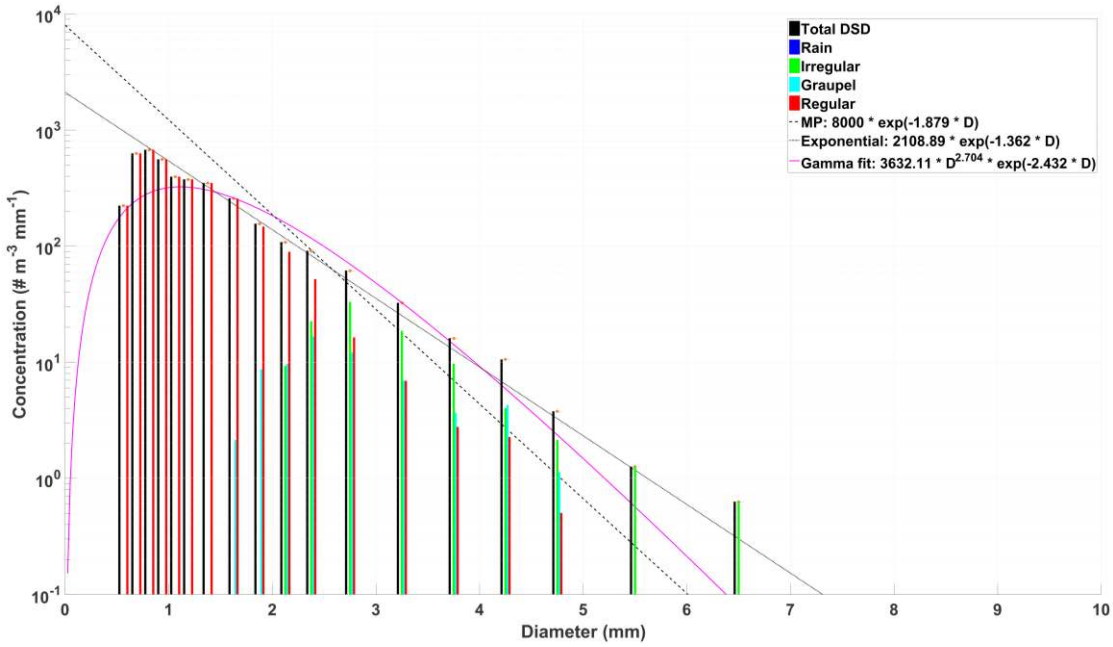

Figure 53. PSD over an approximately 500 m deep layer centered on 5.75 km from 29 May. The distribution shows the total particle concentration in each size bin for all particles (black), rain (dark blue), irregular ice (green), graupel (light blue), and regular ice (red). Also shown are the fitted distributions for the MP (dashed line), exponential (dotted line), and gamma (magenta line) functions. A 95% confidence interval is indicated for the total DSD.

dominate the observed concentrations. As the particle size increased, graupel and irregular ice crystals were largely responsible for the observations with regular ice crystals dropping out of the distribution entirely by 3.5 mm diameter. The entire distribution was rather broad, spanning the size range of 0.5-7.5 mm diameter with concentrations in the range of 10-100 m^{-3} over much of that size range.

As is generally the case with the PSDs examined thus far, the MP relation tended to significantly overestimate the smaller diameter particles, and underestimate the larger diameters. The inverse-exponential and Gamma distributions both showed some amount of agreement with the observed PSD, though both had drawbacks. The inverse-exponential distribution matched the concentrations well in the 1.5-4.5 mm diameter range, but overestimated below 1.5 mm and slightly underestimated above 4.5 mm. Conversely, the Gamma distribution approximated the downward trend at the small particle diameters, but underestimated the concentrations between 0.5-1.5 mm. Above 5 mm, the Gamma distribution underestimated the observed concentrations more than the exponential distribution, however the difference is relatively minor. Although the total PSD displayed a somewhat bimodal character, the individual regular and irregular ice and graupel/hail PSDs were all rather unimodal in character based on visual inspection of Figure 53.

The observed PSD was largely dominated by irregular and regular ice crystals at 6.6 km as graupel began to decrease in concentration (Figure 54). The distribution itself was more skewed towards the smaller diameter particles than the previous layer, with concentrations of diameters around 0.75 mm approaching 1000 m^{-3}. The MP distribution again largely overestimated the small diameter concentrations while systematically underestimating the larger diameter concentrations. As was also the case with the previous layer, the inverse-exponential and Gamma distributions represented

the observations well. The Gamma distribution did underestimate the concentrations of

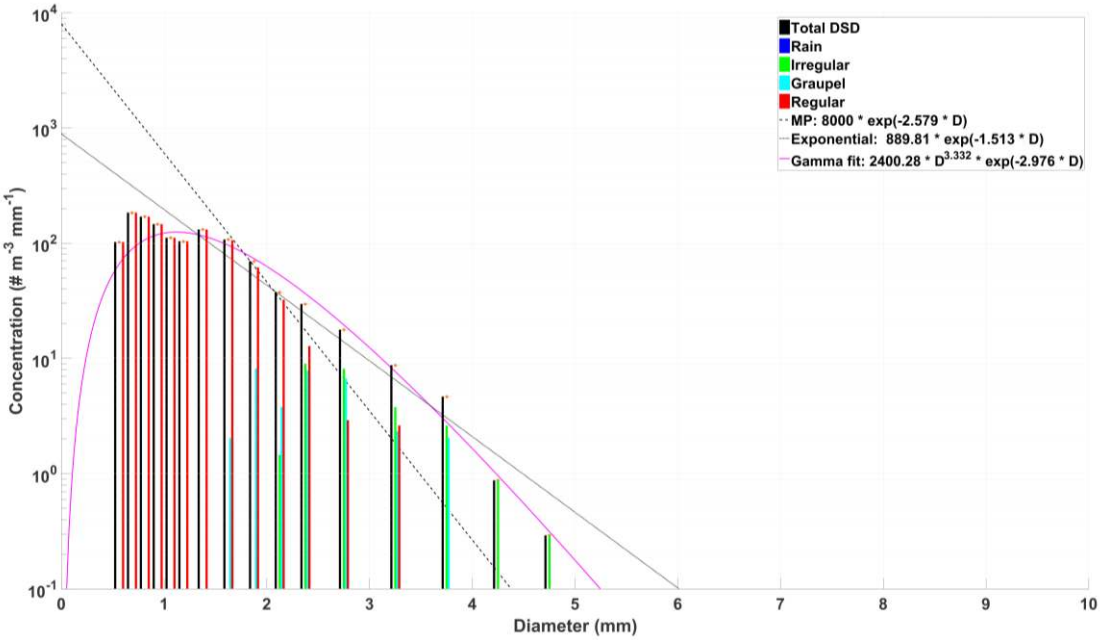

Figure 54. PSD over an approximately 500 m deep layer centered on 6.6 km from 29 May. The distribution shows the total particle concentration in each size bin for all particles (black), rain (dark blue), irregular ice (green), graupel (light blue), and regular ice (red). Also shown are the fitted distributions for the MP (dashed line), exponential (dotted line), and gamma (magenta line) functions. A 95% confidence interval is indicated for the total DSD.

diameters between 0.5 mm and 1 mm, but generally represented the remainder of the distribution well. Given the larger particle concentrations, the Gamma intercept parameter was slightly larger (3136 m^{-3} $mm^{-1-\mu}$) than the value in the previous layer (2839 m^{-3} $mm^{-1-\mu}$). The inverse-exponential distribution was also very close to the observed PSD, only deviating at diameters around 0.5 mm where the fitted function continued to increase in concentration despite the observed decreasing concentration. As with the lower layer (Figure 53), the total PSD again displayed a somewhat bimodal character whereas the individual regular and irregular ice and graupel/hail PSDs were all rather unimodal in character based on visual inspection of Figure 54.

Vertical profiles of the various fitted parameters facilitated comparison of the relative changes of the various functional fits with height (Figure 55). As was

previously observed, there was a considerable amount of disagreement between the three functions in the rain layer. The Gamma function consistently represented the observed DSD throughout the rain layer if graupel/hail particles were excluded from the fitting process. The MP and inverse-exponential distributions both overestimated the concentrations of the smaller particles as was observed in Figure 37.

Above the rain layer and within the ice phase region of the anvil, the three functions tended to converge toward similar values for the determined parameters. Beginning around 5.5 km the shape parameter of the gamma function decreased to values approaching 2, indicating a trend towards the simpler inverse-exponential distribution to which the Gamma distribution reduces exactly for the case of $\mu = 0$. The

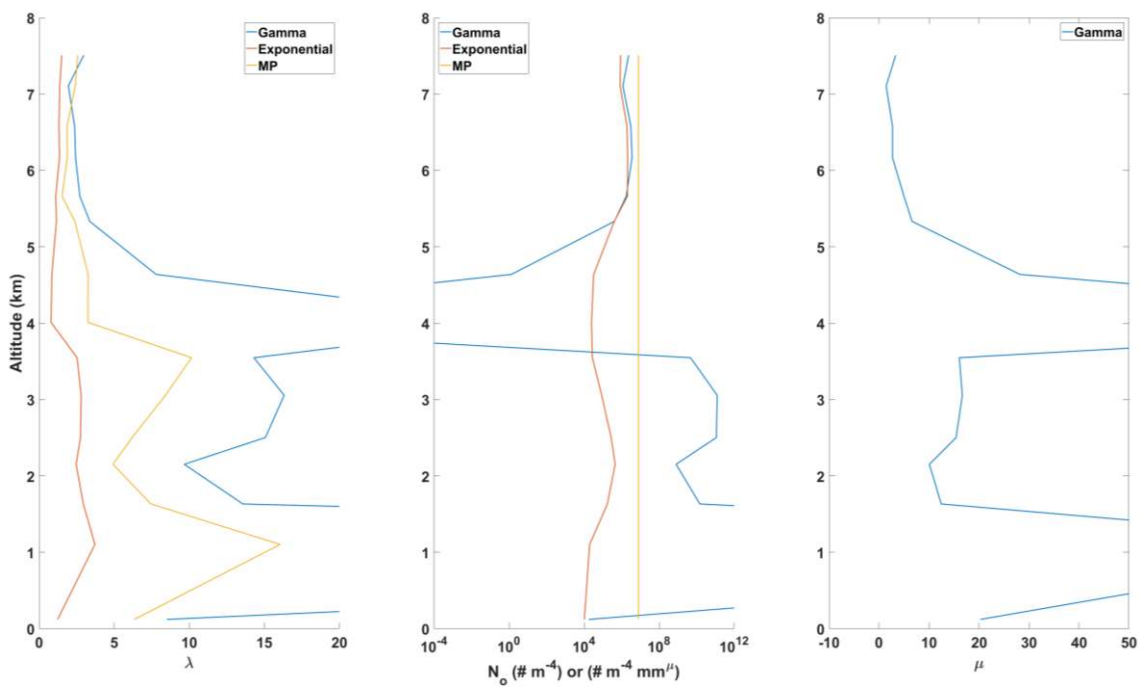

Figure 55. Calculated parameters for the gamma (blue), exponential (red), and MP (yellow) functional fits across 500 m deep layers throughout the 29 May sounding. Parameters were found using the MoM technique.

intercept parameters for the Gamma and the inverse-exponential distributions also trend towards the value assumed by the MP relation. Given these trends, it is reasonable to

infer that the inverse-exponential distribution was rather representative of the ice phase region of this particular case.

7.2.3. *Radar reflectivity comparison*

As with 21 June, particle concentrations were calculated for the 29 May case using 500 m integration depths. A sequence of synthesized, time-spaced objective analyses of SR1, SR2, and NOXP observations provided fields of gridded winds and reflectivity at a 500 m grid spacing within a fixed three-dimensional radar volume via a triple-Doppler radar analysis (Huntrieser et al. 2016), the gridded analyzed reflectivity being assigned the maximum value from the three local radar observations (two of the radars being C-band). As previously described in section 5.4, the output reflectivity fields were linearly interpolated in time and space from the time-spaced radar analyses to the moving Lagrangian point representing the balloon to facilitate direct comparison with camera-derived reflectivity. For the 29 May case, graupel was assumed to have a bulk density of 600 kg m^{-3}, while irregular and regular ice were assumed to have bulk densities of 50 kg m^{-3} and 100 kg m^{-3} respectively as on 21 June. In comparing the observed reflectivity to the reflectivity calculated from the PASIV, generally close agreement was obtained throughout the depth of the sounding. The close agreement between the observations and camera-based calculations indicates high confidence in not only the particle classifications and measured distributions, but also the assumed particle densities for each class.

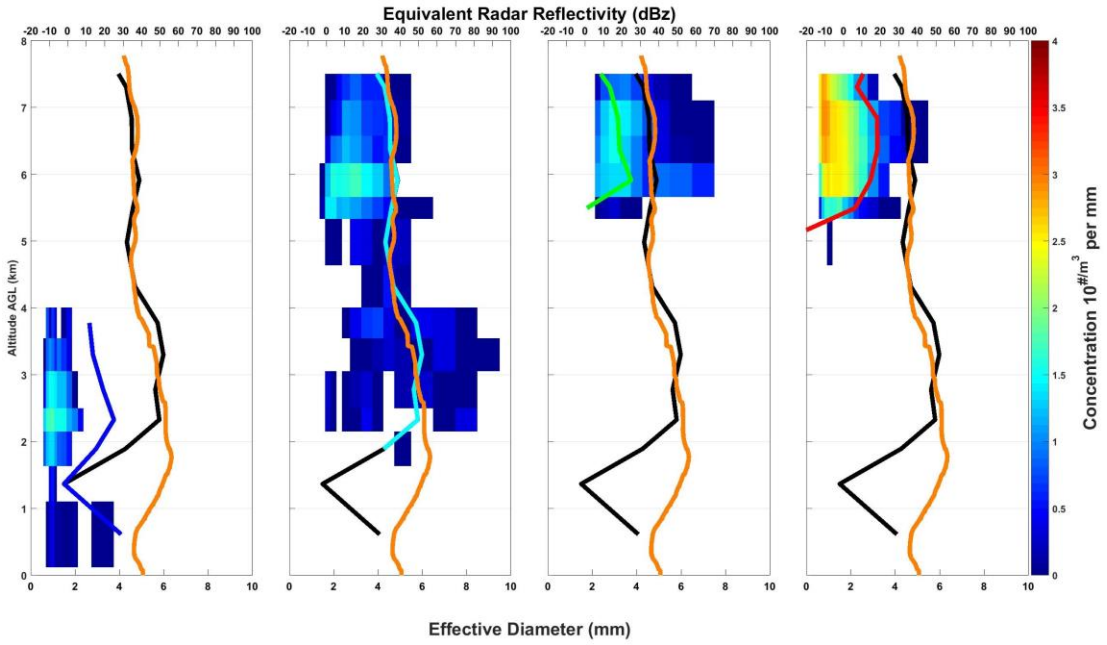

Figure 56. 29 May particle concentrations versus altitude per particle type with calculated and observed radar reflectivity overlaid. Color fill indicates # m^{-3} mm^{-1} per analysis layer (500 m). The orange line indicates the observed radar reflectivity from the triple-Doppler analysis, while the heavy black line is the calculated reflectivity from the measured PSD. The various colored lines in each subplot indicate the reflectivity from that particle classification. Left – rain, left center – graupel, right center – irregular, right – regular.

Throughout the profile, whenever graupel/hail is present in the distribution, the reflectivity from that classification tended to dominate the radar return. The predominance of graupel/hail reflectivity characterized essentially almost the entire profile as graupel and hail were present throughout nearly the entire sampled depth. The predominance of graupel/hail reflectivity was also obtained in the 21 June case (albeit confined to a very shallow layer). These observations of predominant graupel/hail reflectivity are consistent with results of a study by Heymsfield and Musil (1982) who found that graupel, and also to some degree rimed aggregates, were the predominant particle types observed when reflectivity was between 20-40 dBZ. The measured irregular ice crystals in this case contributed some reflectivity, while the regular ice crystals despite their high concentrations contributed very little reflectivity.

Near the surface where graupel/hail was not detected, there was a considerable amount of disagreement between the observed reflectivity and that calculated from the rain drop DSD. While the radar analysis shows reflectivities of up to 40 dBZ over the lowest 1.5 km of the sounding, the PASIV indicates extremely low concentrations of very large rain drops in that region with no appreciable reflectivity. In examining the 50 m resolution particle counts (Figure 50) and personal observations noted at the time of launch, there were widely scattered very large rain drops near ground and aloft. These large drops, and any potentially melting hail present, would be capable of producing moderate reflectivities despite low concentrations. The mobile radars would sample a larger volume in this region and thus would be more likely to observe the sporadic particles than expected with the much smaller PASIV sampling volume. It is hypothesized that there were particles present in the environment that either simply did not pass through the PASIV or else passed through the PASIV but were not imaged by the brief video frame exposure, possibly explaining the discrepancy in the calculated reflectivity.

As with 21 June, there is some uncertainty regarding the assumptions made for particle density when calculating radar reflectivity.

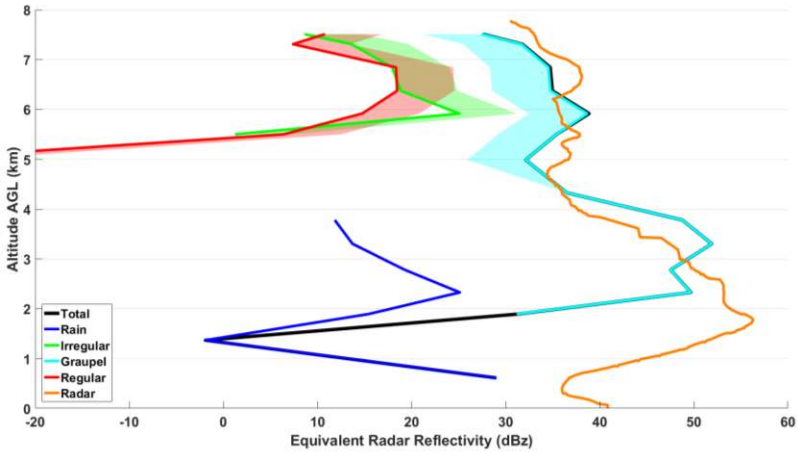

Figure 57. Calculated radar reflectivity from the measured particle distribution on 29 May 2012 showing reflectivity variations due to particle density for the different particle types. Red - regular crystals, green - irregular crystals, light blue - graupel, dark blue – rain.

As such, it is prudent to examine a range of bulk densities for the individual particles habits, the objective being to estimate the possible error in calculated reflectivity due to the assumed bulk particle density value (Figure 57). As previously mentioned, graupel/hail dominates the radar reflectivity calculation throughout much of the profile. Hence, the variations in graupel density are hypothesized to be largely responsible for the radar reflectivity error. In the ice phase region where graupel is present, the PASIV-derived reflectivity generally tends to be well within 5 dBZ of the observed reflectivity and systematically lower except for a single layer near 5.75 km which is higher. This could be the result from a slightly underestimated bulk density for graupel throughout most of the flight, and a slightly overestimated density near 5.75 km. As explored in subsequent discussion, a locally lower bulk graupel/hail density could arise from potentially very low rime layer densities associated with moderate supercooled cloud water mixing ratios at large undercoolings at high altitude (Macklin 1962, Heymsfield and Pflaum 1985).

7.2.4. Precipitation mixing ratio

The time-dependent, 3-D triple Doppler radar analysis fields of airflow and reflectivity for this case were assimilated via a diabatic Lagrangian analysis (DLA, Ziegler 2013a,b) which retrieved potential temperature as well as water vapor cloud water and ice mixing ratios and virtual buoyancy. The DLA additionally diagnosed the rain, graupel/hail, and snow particle mixing ratio fields. These collective DLA outputs provided a unique opportunity to compare observed mixing ratio values determined from the camera-derived PSDs with mixing ratios retrieved from the actual radar-observed storm employing a conventional single-moment cloud model microphysics

module. The DLA utilized an inverse-exponential distribution form for rain, graupel/hail, and snow particles (Ziegler 2013a,b) following the Lin-Farley-Orville (LFO) microphysics parameterization by Gilmore et al. (2004a). The rain and snow intercept parameters in the DLA were assigned inferred supercell-representative values of $8x10^5$ m^{-4} and8 $x10^6$ m^{-4} respectively following Ziegler et al. (2010), while a height- and reflectivity-dependent expression for the graupel/hail intercept was derived from an empirical fit to the mass-weighted average intercept values from the evolving low-, medium-, and high-density graupel and frozen drop distributions in the same simulated supercell (Ziegler et al. 2010). Snow was diagnosed from dimensional parameterized relationships for bulk ice nucleation and deposition growth evaluated along Lagrangian air trajectories using output statistics of the snow field in a simulated supercell storm by Ziegler et al. (2010). The earlier supercell simulation employed a single-moment parameterization in the Straka Atmospheric Model's 10-class bulk ice (10-ICE) scheme (Straka and Mansell 2005). It is important to note that the maximum DLA-diagnosed snow mixing ratio Q_{max} was constrained for the 29 May analysis case to satisfy an a priori chosen input parameter value of Q_{max} = 1 g kg^{-1}, although the optional choice of a larger Q_{max} value would have scaled the DLA snow mixing ratio field accordingly.

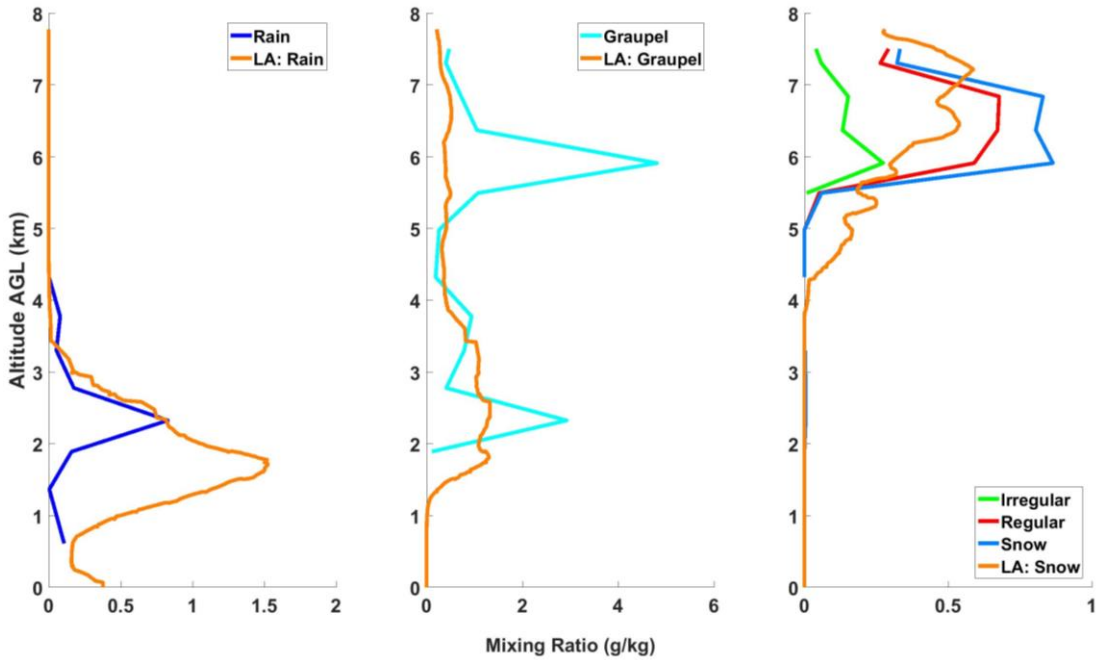

Figure 58. Particle mixing ratios for 29 May 2012 by type (rain - left, graupel/hail - middle, snow - - right) as a function of altitude. The orange line in each subplot shows the retrieved mixing ratio for that particle type from the DLA. The PASIV mixing ratios are shown as dark blue for rain, cyan for graupel, green for irregular ice, red for regular ice, and light blue for combined snow. Analysis was done for 500 m integration layers.

Mixing ratios for rain (dark blue), graupel/hail (cyan), irregular ice crystals (green), and regular ice crystals (red) were calculated using the camera PSDs and the procedures outlined in section 5.3.4.3 (Figure 58). Since the DLA provided only mixing ratios for rain, graupel/hail, and snow (depicted as the orange line for each particle class), the irregular and regular ice crystal categories from the camera PSDs were also combined to form a hybrid snow category (light blue) for comparison. As previously described in section 5.4, the output fields including temperature and the mixing ratios of cloud and precipitation were linearly interpolated in time and space from the time-spaced DLA analyses to the moving Lagrangian point representing the balloon to facilitate direct comparison with and provide context for interpreting the camera-derived precipitation mixing ratios.

In the warm layer below the melting level, the DLA implied a larger rain mixing ratio than the rain mixing ratio obtained from the PASIV. The DLA-derived rain mixing ratio varied throughout the warm layer in relation to the observed reflectivity profile and the mass fraction of retrieved graupel/hail. The peak DLA-derived rain mixing ratio value of roughly 1.5 g kg^{-1} occurred around 1.7 km, whereas the maximum in the PASIV occurred near 2.3 km and is a much lower value (roughly 0.7 g kg^{-1}). This disagreement was likely caused by the widely scattered large rain drops that as previously discussed were not well sampled by the PASIV. In the same layer, the camera-derived graupel/hail contained a strong local maximum value (3 g kg^{-1}) around 2.2 km where the PASIV indicates higher mixing ratios than compared to the 1 g kg^{-1} from the DLA. Since the bulk graupel/hail category in the DLA cannot distinguish between size-distributed graupel and hail separately, it is possible that the assumptions made in the DLA microphysics scheme could have effectively limited the resolution of the microstructure of large hail as potentially sampled by the PASIV. On the other hand, the potential undersampling of the relatively rare large particles by the PASIV likely qualified somewhat the camera-derived mixing ratio values at low levels. As rain concentrations increased around 2.5 km and drop sizes decreased, the disagreement between the rain and graupel/hail mixing ratios from the PASIV and the DLA also decreased.

Above the melting layer however, once the PASIV enters the anvil region of the supercell, there are various regions of agreement and disagreement between the DLA and the PASIV. In the 3-5 km and 6.3-7 km layers, the DLA and PASIV both indicate nearly identical graupel/hail mixing ratios (0.5 g kg^{-1}). These regions show low total

graupel/hail concentrations on the order of 10 m^{-3}, however the agreement between the two indicates that the region was well sampled but simply did not contain significant particle mass.

For the 5-6.3 km layer however, there is considerable disagreement between the graupel/hail mixing ratios from the PASIV and the DLA. The retrieved mixing ratio from the DLA is still fairly constant around 0.5 g kg^{-1} in the 5-6.3 km layer, while the PASIV indicates mixing ratios of up to 5 g kg^{-1} in a single 500 m layer at 5.5 km. This corresponds to an area in which total graupel/hail concentrations were found to be on the order of 100 m^{-3}. The size distribution did not change appreciably throughout these layers, only the total concentration. Given the camera PSD observations and considering also the high-biased graupel/hail reflectivity in the 5.5 km layer, it is possible that the assumed 600 kg m^{-3} graupel/hail density value in the camera-derived PSD calculations is locally too large.

The comparison of camera PSD and DLA snow mixing ratio values shows a similar behavior to the graupel/hail mixing ratio comparison. Above 5 km, the DLA shows a steady increase from roughly 0.2 g kg^{-1} to 0.6 g kg^{-1} by 7 km (but note again that the DLA snow mixing ratio value was limited to an assumed Q_{max} = 1 g kg^{-1}). The total snow mixing ratio from the PASIV shows values of order 1 g kg^{-1} over the same layer or roughly a factor of two larger than the DLA values, which implies that a more appropriate a posteriori choice of Q_{max} could be ~ 2 g kg^{-1}. Separating the hybrid PSD snow category into the regular and irregular ice crystal categories, it is evident that a majority of the mass comes from the regular ice crystals. While the concentration-weighted mean diameter of the irregular crystals is somewhat larger than the mean

regular crystal diameter, the irregular crystals have lower total concentrations (~ 50 m^{-3}) than the regular ice crystals (1000 m^{-3}) and also have lower assumed bulk densities. The regular ice crystal mixing ratio values compare well with the DLA values for snow, indicating that the DLA may be not be handling the irregular ice crystals properly due again to the DLA's inability to discriminate potential variability of particle habit within the broad upper tail of the parameterized PSD. Although the irregular crystals do not contribute a majority of the snow particle mass, they largely account for the observed differences between the DLA and the PASIV.

7.2.5. Particle velocity distribution

Given the general agreement of various theoretical fall speed relations to the observed particles in the 21 June case, it is reasonable to apply the same velocity relations to the 29 May case to examine the structure of the size-velocity distribution of the camera data. However, the Kingfisher storm provides a unique challenge in that hail and small graupel are present in the sounding in various layers. While the previously-used fall speed relations for graupel still apply, an independent relation for hail fall speed is prudent in the 29 May case.

Heymsfield and Wright (2014) provide a velocity-diameter relation for 900 kg m^{-3} bulk density hail particles valid in the size range between 6 and 15 mm diameter. For the purposes of this analysis, the applied dynamic range of this hail fall speed relation is extended slightly to cover 1-16 mm diameters. A difficulty arises in discriminating which particles are high-density hail or lower density graupel. It is likely that there is a mixture of the two, particularly near the melting level. Graupel will tend to survive further below the melting level than ice crystals, but will eventually collapse

inward as melting proceeds. This process of deliquiescence during melting would have a significant effect on the fall speed of the graupel particle. Higher density hail will survive greater distances, and will tend to shed excess water from its surface. This makes accurate depictions of individual melting graupel and hail particle fall speeds more difficult given the current information provided by the PASIV (e.g., lacking unambiguous distinction between hail and graupel or information about the liquid water fraction of the melting ice particle). Hence, it is assumed for the limited purpose of estimating graupel and hail fall speeds that any particles which fall within the graupel classification and are at temperatures above freezing are hail. Their velocities are calculated using Eq. (8) from Heymsfield and Wright (2014). At temperatures colder than freezing, all graupel/hail classifications are considered graupel whose terminal velocity is calculated using the relations from Bohm (1989) discussed previously.

The diameter-velocity distribution for the 0-4km layer shows the spread in the distribution which is due to detections of given sized rain drops and hail particles at a range of altitudes and bulk air densities (Figure 59). A rise rate of 4 m s^{-1} was assumed

for this layer. While there are a number of smaller hailstones that have comparable

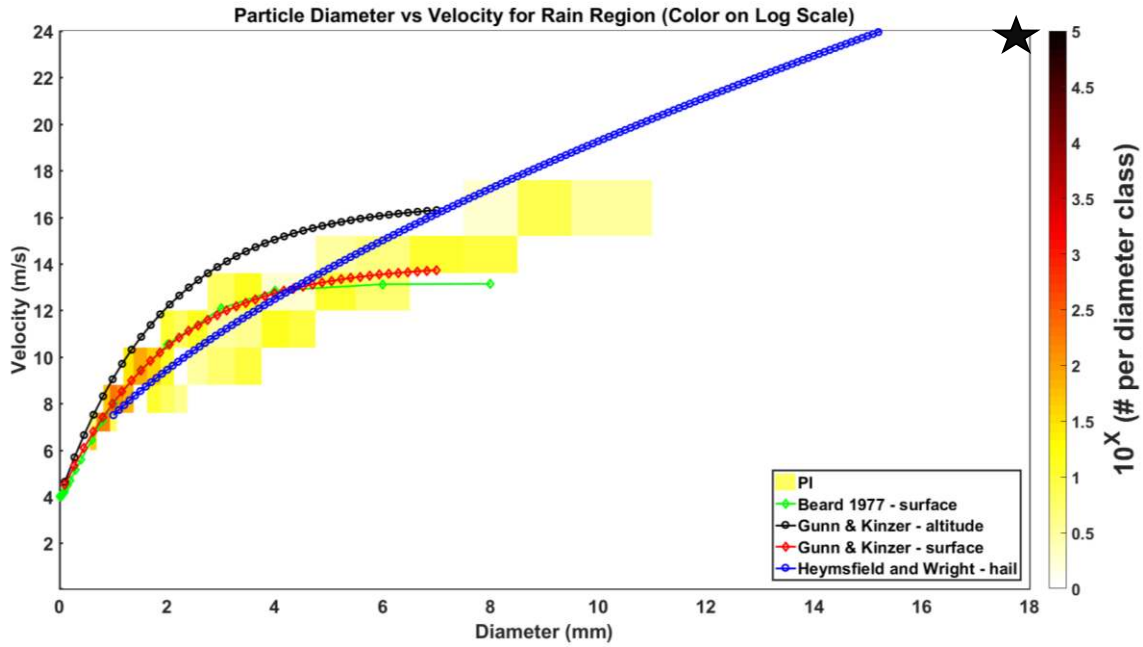

Figure 59. Camera size distribution and calculated velocities for the rain layer (sfc - 4km) in 29 May 2012. The color filled scale depicts the number of particles in a given size-velocity bin on a log scale. Also shown are theoretical relations from Beard (1977) , Gunn & Kinzer (1949), and Heymsfield and Wright (2014). The latter two have been adjusted upwards according to the assumed rise rate of 4 m s^{-1}. Velocity was calculated using Gunn & Kinzer (1949) for rain and Heymsfield and Wright (2014) for hail. The large hailstone depicted in Figure 51 is denoted with a star.

velocities to some of the larger raindrops, many of the larger stones have considerably higher velocities. A majority of the objects detected were relatively small raindrops in the 0.5-2 mm diameter range. Due to the low concentrations, many of the larger particles are singular occurrences and as such are not displayed in Figure 59. The one exception is the large hailstone discussed earlier (Figure 51) which is of such notable occurrence that it has been marked on the figure with a star. The 18 mm diameter hail stone had a fall velocity of approximately 20 m s^{-1} relative to ground.

Once the PASIV enters the anvil region, a mixture of graupel, irregular ice, and regular ice particles results in a more bimodal distribution of derived fall speeds than in the rain layer (Figure 60). Because the velocity of each particle changes with the air

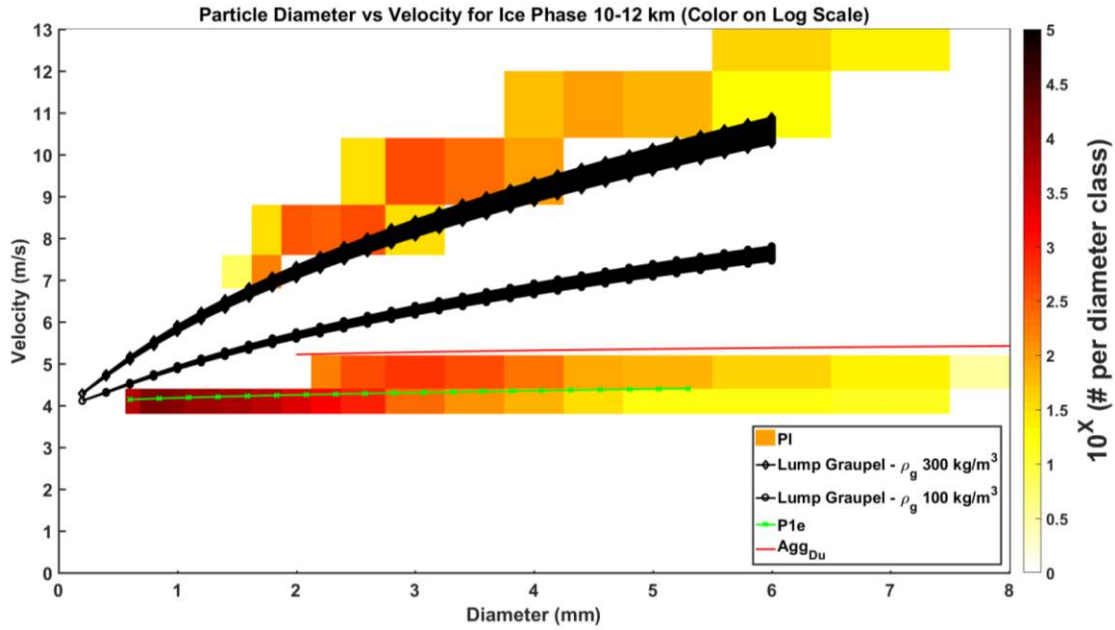

Figure 60. Camera size distribution and calculated velocities for the ice layer above 5 km on 29 May 2012 with multiple velocity relations adjusted for the assumed balloon ascent rate (4 m/s). The color filled scale depicts the number of particles in a given size-velocity bin on a log scale. Regular crystal velocity was calculated using the "P1e" relation, irregular crystal velocity was calculated using the "Agg_{Du}" relation, and graupel was calculated using the 300 kg/m^3 Bohm (1989).

and bulk particle densities, the application of the fall speed relations are corrected for the local air density value with inclusion of the assumed bulk particle density. The size-distributed graupel particle fall speeds are typically different than the reference graupel fall speed curves which for simplicity have assumed a small constant bulk particle density value that is consistent with the 21 June case analysis. Rather than showing a reference fall speed relation valid at a single point, a spread of each relation corrected for the range of air densities experienced in the layer is presented. This gives an estimate of the expected range of the particle velocities throughout the layer that factors the variation of particle drag with air density. The distribution in Figure 60 shows that a majority of the particles were concentrated around the smaller sizes and slower fall speeds. While the fall speed of irregular and regular ice shows little variation, graupel ranges between 6.5-12 m s^{-1} PASIV-relative velocities (i.e., 2.5-8 m s^{-1} range of ground-

relative fall speeds with respect to still air). Given the likely higher density graupel sampled by the PASIV as suggested by the radar and DLA comparisons, the fall speeds above 5 km were calculated with the assumed bulk density value of 600 kg m^{-3}.

7.2.6. Electric field profile in the context of observed microphysics

In addition to the PASIV probe, an electric field meter was also used for the 29 May case. The 3-component electric field shows a sharp change in the vertical component which approaches -80 kV m^{-1} around 6 km (Figure 61). This rapid change in the vertical electric field intensity occurs as the instrument train begins to approach the region of higher particle concentrations detected around the base of the anvil region. Between 6 and 8 km, the field value changes sign to positive and approaches values of up to +50 kV m^{-1}.

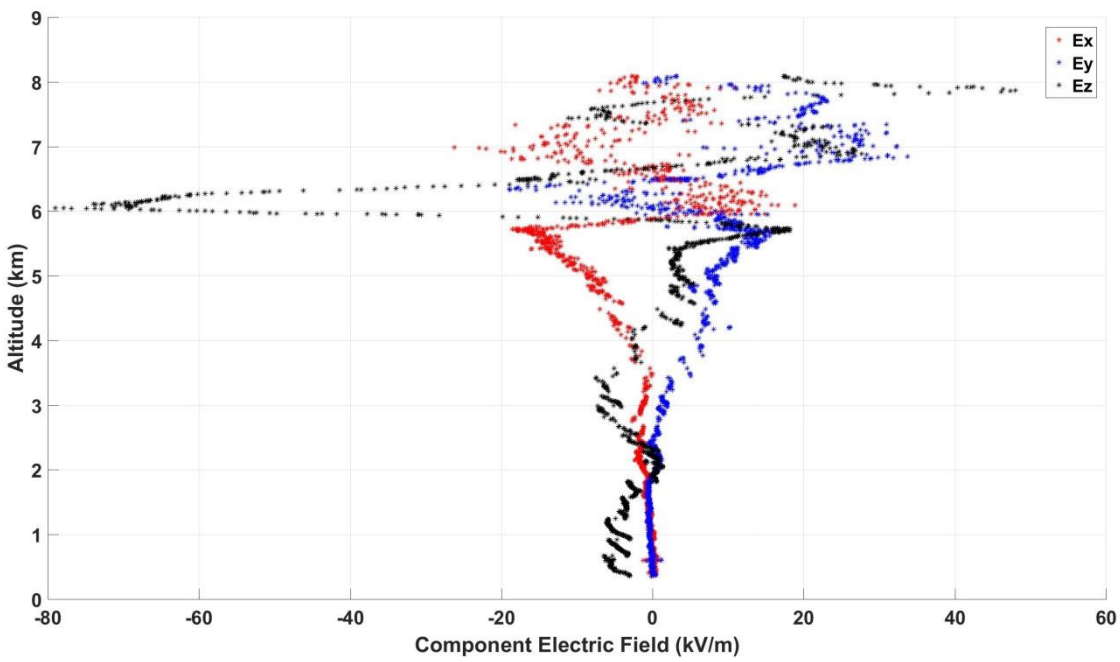

Figure 61. Total electric field profile for 29 May 2012, broken down in to x (red dots), y (blue dots) and z (black dots) components.

Performing a standard net space charge layer analysis (Rust and Marshall 1989) and overlaying the net space charge profile on the identified particle types, it is evident

that the region of negative charge corresponds to a layer of higher graupel concentrations of up to approximately 50 m^{-3} (Figure 62). This region also contains a low concentration of the irregular crystal types on the order of 10 m^{-3}. The regular ice crystal concentrations are on the order of 500-1000 m^{-3}, but do not vary much throughout the sounding. The temperature of this layer varies between approximately -12°C and -17°C. The negative charge region is the strongest charge layer of the sounding, with a value of nearly -2 x 10^{-9} C m^{-3}. This is a considerably higher negative charge than was found in the 21 June case, in addition to the higher graupel/hail concentrations.

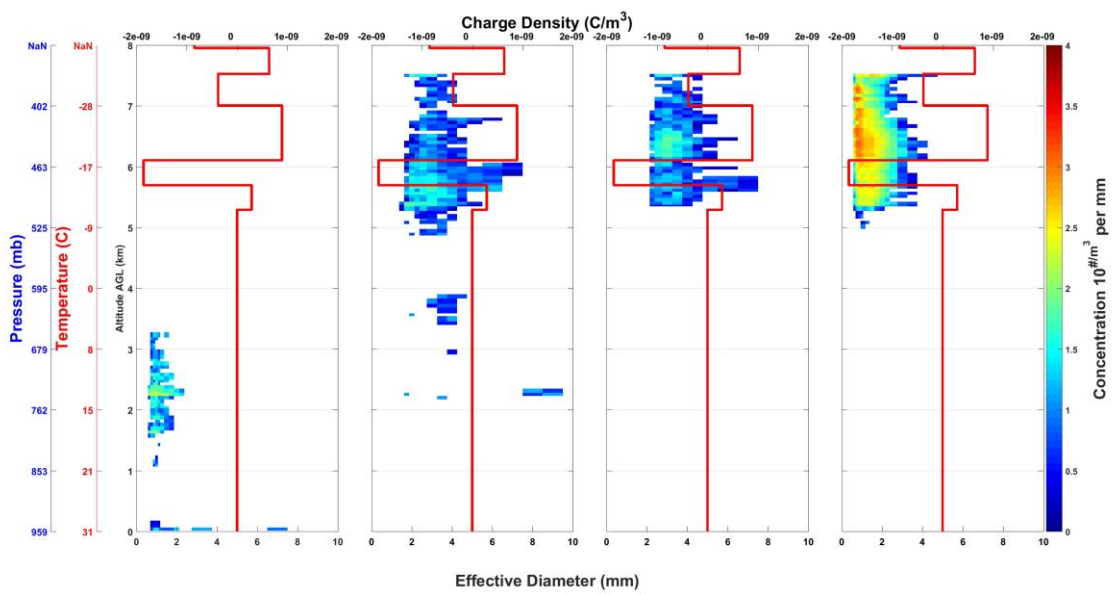

Figure 62. Camera data from 29 May 2012 showing particle concentration as a function of altitude, temperature, and pressure according to particle type (rain -left, graupel – left middle, irregular – right middle, and crystal - right) with charge density (C/m^3) overlaid. Color fill shows number of detected particles, per size bin, per analysis layer (50 m). Charge density (red line) shown on second axis.

Above the negative net space charge layer, irregular crystals increase in concentration, approaching values of 100 m^{-3}, while graupel concentrations decrease. The observed concentrations of the regular ice crystals also increase slightly, but remain

in the 500-1000 m^{-3} range. These changes in concentration are accompanied by a transition to a positive net space charge layer, with a charge value of 1 x 10^{-9} C m^{-3}.

The radar analysis indicates that there are no large vertical motions at the balloon location at the upper levels of the sounding (Figure 63, Figure 64). The interpolated vertical velocity profile at the PASIV location (not shown) reveals that there are two layers containing significant updraft, the lower layer from 4.8 to 5.3 km (~2339) containing updraft up to 6 m s^{-1} and the upper layer from 5.7 to 7.4 km (~ 2345) containing updraft up to 2 m s^{-1}. Furthermore, maximum values of cloud water

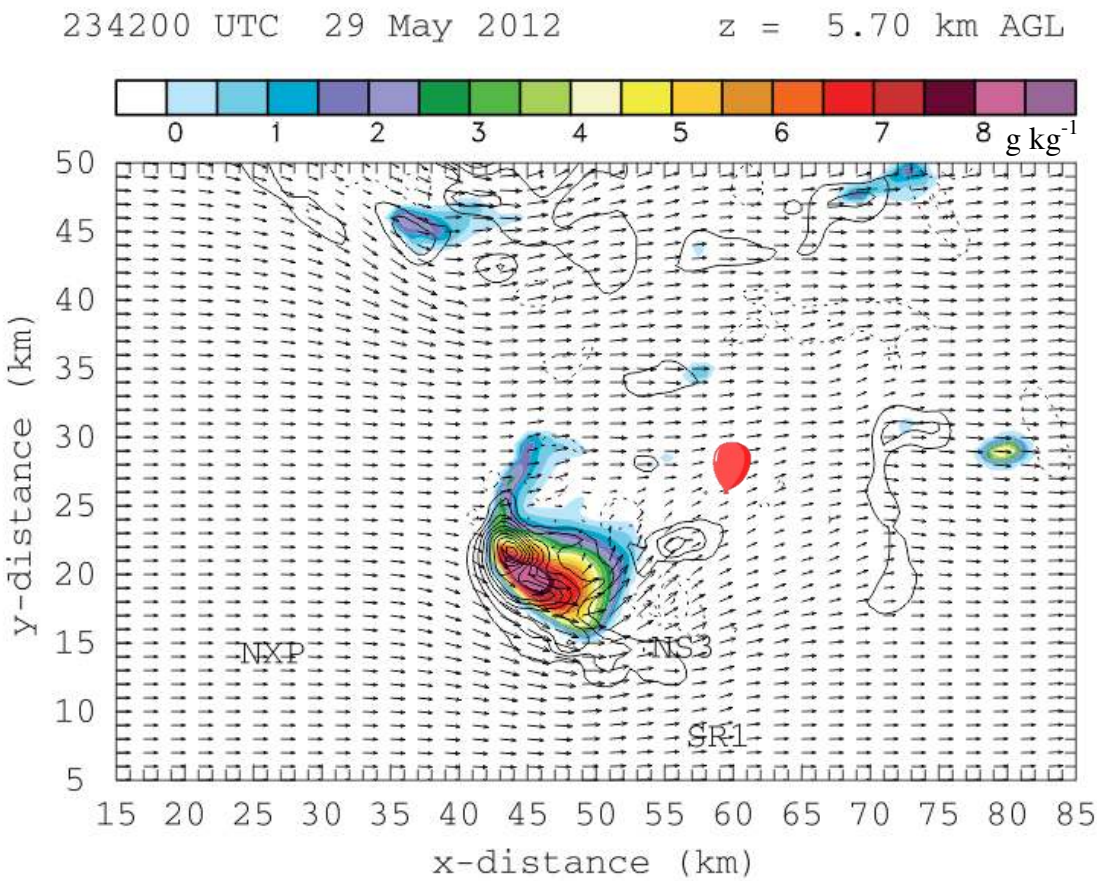

Figure 63. DLA at 5.7 km AGL and 2342 UTC for 29 May. Color fill shows cloud water mixing ratio (g kg^{-1}), synthesized wind vectors are scaled to 1 km = 20 m s^{-1}, and contours indicate vertical veloctiy at 5 m s^{-1}. Updrafts are solid, downdrafts are dashed. Balloon location at 23:41 UTC and 5.75 km indicated.

mixing ratio in the vicinity of the PASIV are of order 0.1 g kg^{-1} in the lower charge layer (Figure 63), while values approaching 1 g kg^{-1} are found in the positive charge region both at and upstream from the PASIV location (Figure 64). Given the rather weak updrafts, modest levels of available supercooled cloud liquid water mixing ratios, and the cold temperatures in the negative charge layer (-17°C to -27°C), it is likely that the dense, fast-falling graupel acquires and transports negative charge during collisions and falls out due to sedimentation in the absence of strong updrafts to form the lower

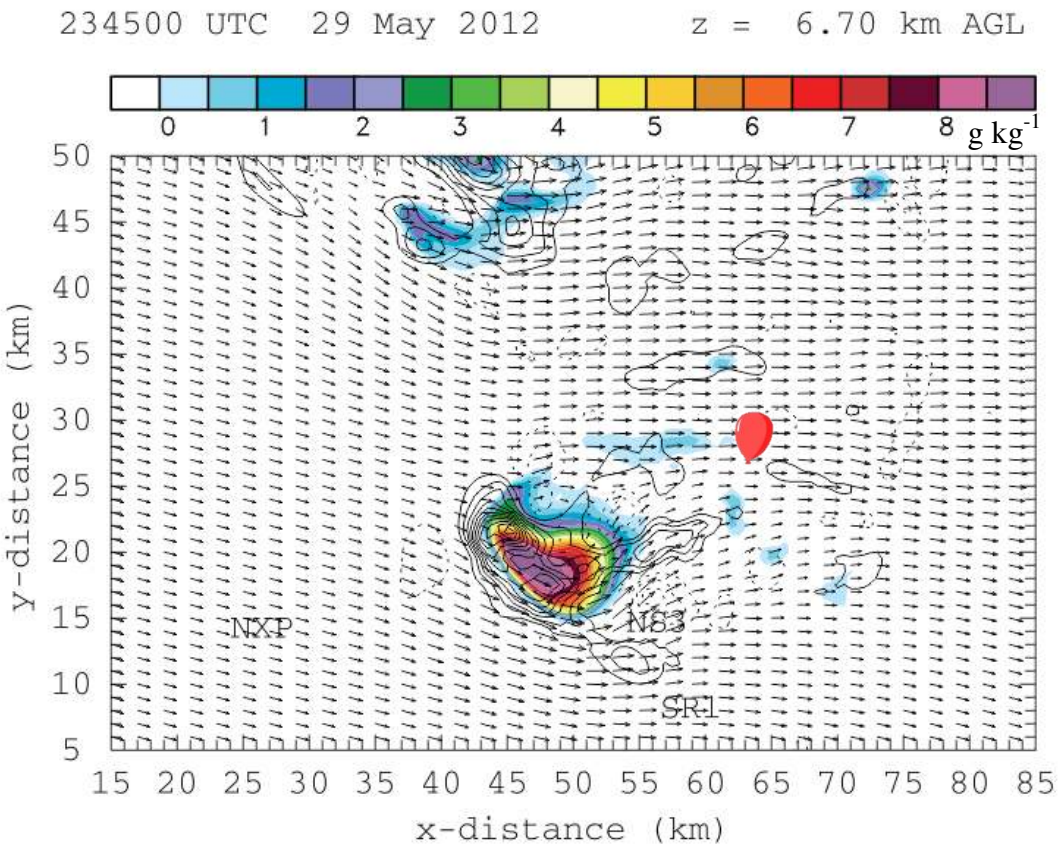

Figure 64. DLA at 6.7 km AGL and 2345 UTC for 29 May. Color fill shows cloud water mixing ratio (g kg^{-1}), synthesized wind vectors are scaled to 1 km = 20 m s^{-1}, and contours indicate vertical veloctiy at 5 m s^{-1}. Updrafts are solid, downdrafts are dashed. Balloon location at 23:41 UTC and 6.6 km indicated.

negative net space charge layer (MacGorman and Rust, 1998). The lighter, more slowly falling positively charged ice crystals likely form the net positive space charge layer at higher altitudes.

Above the main positive net space charge layer, particle concentrations decrease slightly for the irregular ice crystals and the vertical electric field profile becomes noisy. Beginning around 7 km the three components of the electric field are comparable in magnitude, thus rendering the one dimensional assumption inherent in the charge layer analysis as somewhat questionable. While not strictly valid, the computation of the charge layers using the vertical component is still performed, with the understanding that the identified layers are not necessarily an indication of the actual net charge profile. Furthermore, the uppermost charge layer identified was cut short due to the lightning strike mentioned earlier, leading to an incomplete picture of that particular layer. Given these limitations, it is improper to suggest an overall charge structure for the 29 May case outside of the discussed lower negative and upper positive net space charge layers.

Chapter 8

Integration and discussion of field observations

The two cases presented here highlight the ability of the PASIV to collect microphysics observations at an unprecedented level of detail. Although both cases represent deep convection, the storms are located in quite different convective environments and only the 29 May supercell storm contains severe weather. Thus, comparing these two cases presents a unique opportunity to compare the potentially widely ranging character of convective precipitation associated with storm intensity. Both significant differences and similarities are noted between the two cases.

8.1 Particle size distributions and concentrations

Both cases showed a wide range of PSDs across all particles types. The rain layer proved to be most challenging for observations as in both cases the distribution largely contained widely scattered drops but also containing hailstones on 29 May that were collectively somewhat incompletely sampled by the PASIV in the low levels. This serves to highlight one of the weaknesses of the PASIV instrument in that it is a limited sample size, a problem common with nearly all in situ disdrometers. In the ice phase region however, very high particle concentrations composed of varying mixtures of graupel, irregular ice crystals, and regular ice crystals are observed. The regular ice crystal category showed the highest concentrations in both cases, with similar structure to the distribution of particles. Both show the highest concentration values in the lowest few size bins, and detections rapidly begin to drop off above 2.5 mm diameter.

The 21 June case has much larger particle concentration values and a slightly broader spread of sizes than the 29 May case. The maximum total observed particle concentration was roughly 2800 m^{-3} on 29 May, whereas a maximum total particle concentration of 9470 m^{-3} (over 3 times more particles) in the same size bin (0.687 mm diameter) was observed on 21 June. The 21 June case showed higher concentrations of irregular ice crystals, on the order of 500 m^{-3} compared to 100 m^{-3} for 29 May, but also significantly less graupel. The 29 May sounding showed graupel present at all altitudes above the freezing layer in the anvil region, while the 21 June case showed only moderate concentrations localized near the freezing level. It is likely that the increased liquid water content and higher vertical velocities associated with the 29 May supercell storm case led to the increased production of larger, denser graupel and hailstones at the expense of smaller, low-density snow particles which likely served as graupel/hail embryos (Heymsfield and Musil 1982). The irregular crystals that were produced on 29 May may have also been more heavily rimed. Figure 64 at 6.7 km and Figure 65 at 8.7 km (at 2345 and 2348 UTC respectively) demonstrate the amount of cloud water available in the storm as retrieved by the DLA. A cross section through the storm indicated by the dashed black line in Figure 65 shows that this cloud water is being detrained out into the left anvil region where the PASIV sounding rose through (Figure 66). A combination of these effects could act to reduce the number of smaller ice crystals present in the 29 May anvil in favor of the higher density rimed particles. As previously noted in section 7.2.3, rime densities would be expected to be considerably smaller than the storm-average assumed 600 kg m^{-3} value in the low temperatures (not shown) of around -30 C and low supercooled liquid water contents present in the

northern anvil on 29 May. It should also be noted that the possibility of locally smaller bulk graupel densities in the northern anvil on 29 May would associate with locally better agreement between PASIV-calculated and observed reflectivities. Hence these collective storm observations are consistent with what would be expected given the two contrasting environments.

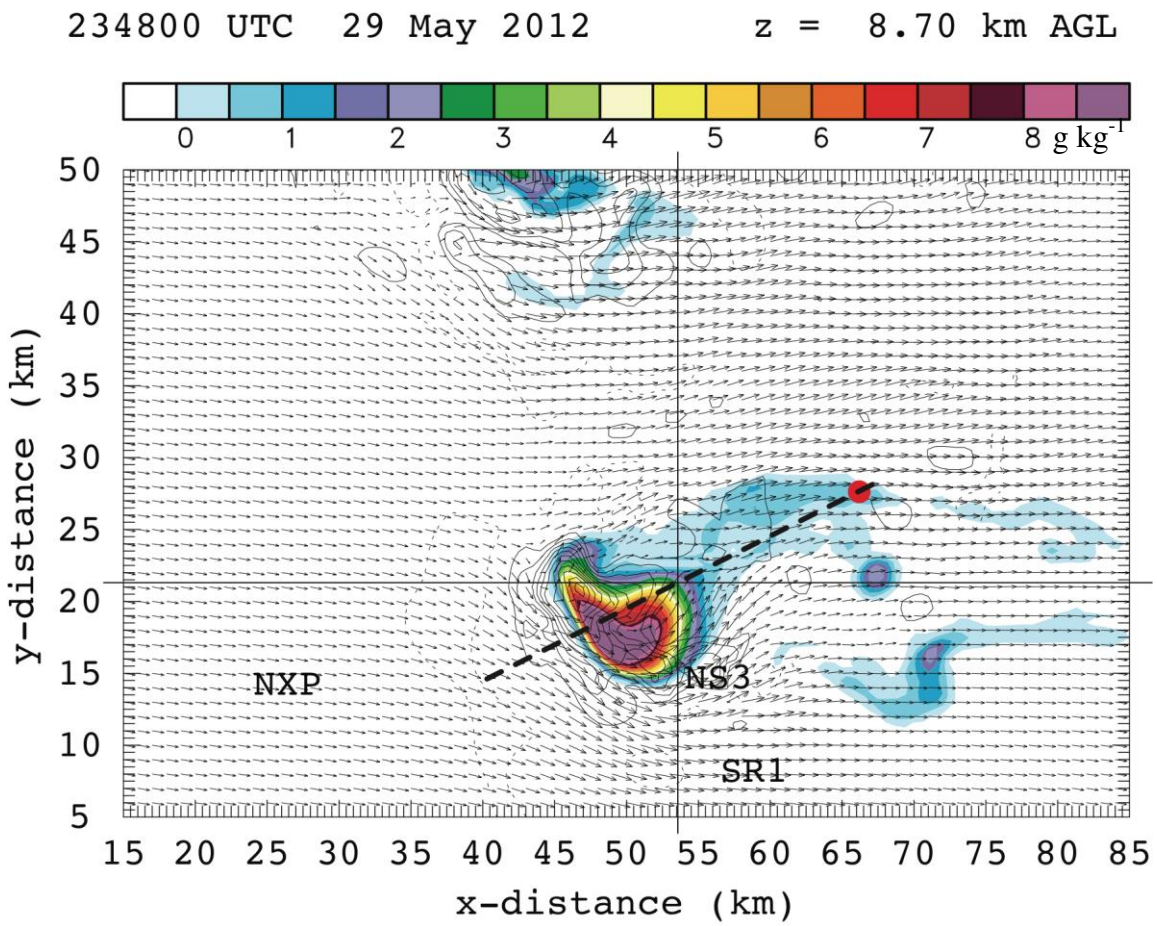

Figure 65. Triple-Doppler analysis at 8.7 km AGL and 2348 UTC for 29 May. Color fill shows cloud water mixing ratio (g kg^{-1}), synthesized wind vectors are scaled to 1 km = 20 m s^{-1}, and contours indicate vertical veloctiy at 5 m s^{-1}. Updrafts are solid, downdrafts are dashed. Black dotted line indicates cross section

A significant note of comparison between the two cases relates to the fine vertical length scales over which concentrations of the various particles were not infrequently observed to change dramatically. In both the 21 June and 29 May cases, there were rapid observed shifts in particle concentrations over several orders of

magnitude on spatial scales as small as 50 m. Observations on this fine vertical scale were not previously possible given the sampling limitations of previous observing platforms, and serve to highlight the potential degree of heterogeneity in the vertical dimension and hypothetically also in the horizontal dimension given a possibly isotropic 3-D structure. This difference is exemplified by comparing Figure 32 (50 m) and Figure 39 (500 m). The previous balloon-borne videosondes were limited in their sampling ability and also were unable to resolve vertical length scales as small as the PASIV's minimum resolvable scale of order 50 m.

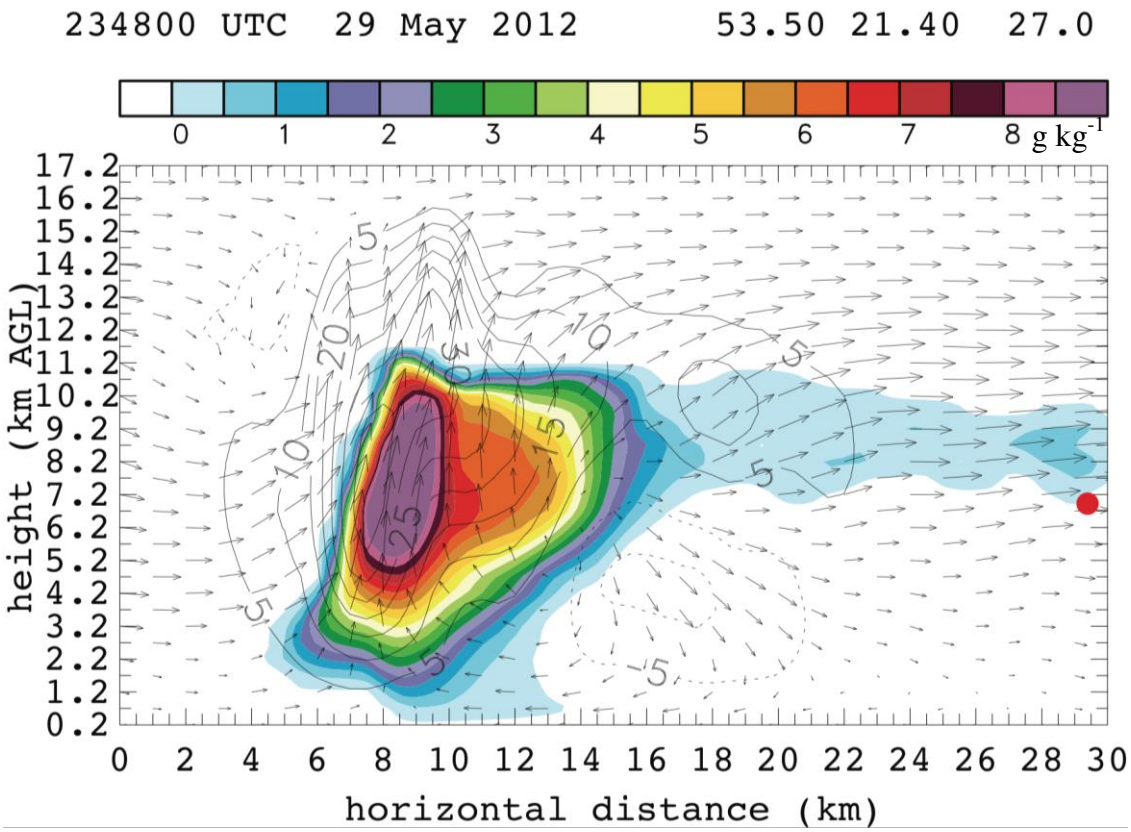

Figure 66. Triple-Doppler analysis 2348 UTC for 29 May. Cross section indicated in Figure 65. Color fill shows cloud water mixing ratio (g kg^{-1}), synthesized wind vectors are scaled to 1 km = 20 m s^{-1}, and contours indicate vertical veloctiy at 5 m s^{-1}. Updrafts are solid, downdrafts are dashed. Balloon location at 2348 UTC marked.

8.2 Radar comparisons

Using the distributions sampled by the PASIV, both cases were compared against observed mobile radar data for validation and insight into the distribution which comprises the radar return. In both cases the observed radar reflectivity from the available mobile radars agrees rather well overall with the reflectivity calculated from the PASIV-derived PSDs with assumed values of bulk particle density. Both the 21 June and 29 May cases were characterized by averaged differences of only a few dBz versus radar observations through the full depth of the soundings. However, it is noted that both cases had relatively shallow layers that contained larger differences up to the order of 5-10 dBZ. This could be at least partially attributable to the 29 May case using an objective analysis based on the largest local reflectivity value among the SR1 and SR2 (C-band) and the NOXP (X-band) radars, whereas the 21 June case only used objectively analyzed SR2 radar data. As previously discussed in section 8.1, a more likely contributing factor to local differences between PASIV-derived and radar-observed reflectivities is the assumed constant value of bulk particle density due to possible fresh rime accretion in very cold temperatures and low rime layer densities.

In both cases, it was possible to show which particle type dominated the radar return within any given layer. For example when graupel was present in either case, its higher bulk density combined with its moderate sizes and concentrations controlled the radar reflectivity (e.g., as through the entire 29 May sounding). Despite overall good agreement between PASIV-derived and observed reflectivity on 29 May, a shallow layer around 6 km had up to 5 dBZ higher reflectivity in association with a locally larger concentration of 1-2 mm diameter graupel than adjacent levels as well as locally

higher graupel mixing ratio than estimated by the DLA. In that layer dominated by graupel/hail reflectivity, it is hypothesized that graupel/hail bulk density is locally less than the assumed constant value of 600 kg m^{-3}. However in the 21 June case, graupel was confined to a shallow layer immediately above the melting layer. In the absence of graupel, the irregular and regular ice crystal classifications have periods where they dominant the reflectivity. This partitioning of the radar reflectivity is not possible given previous observations and provides more information than the bulk particle classifications available from radar observations (e.g., HCA).

In the rain layer which sometimes contained hail, comparisons between the PASIV and radar observations are difficult due to the inherent sampling differences of the instruments. In the rain layer for the two cases presented, the distributions are comprised of widely scattered particles. Although the integrated sampling depth of the PASIV approximates the radar pulse volume diameter, the PASIV nevertheless has difficulty sampling these sporadic particles given its very small sample volume compared to the circular-cylindrical radar pulse volume. This is more of an issue in the rain layer of the 29 May case where the disagreement between the PASIV reflectivity and the observed reflectivity is larger. In the 21 June case, the PASIV appeared to sample the actual distribution well (assuming valid bulk particle densities) since the calculated reflectivity agrees nearly perfectly with that observed by the mobile C-band SR2 radar. This is a limitation of a smaller balloon-borne system and is unavoidable, however it does serve to highlight the probable precipitation microstructure within the radar pulse volume.

8.3 Bulk microphysics comparisons

The two cases also provided an opportunity to look at various size distributions across specific layers and how various generalized functions conformed to those observed distributions. This is complicated by the fact that observations of this detail are limited. Surface disdrometers are capable of providing distributions with which functions can be fit, but aircraft observations can often find that difficult due to their large sample volumes. If the environment is generally steady-state and homogenous, then the aircraft distributions can be used to determine the parameters for various assumed functions. In either case, observations of the type presented here can also be compared to microphysics schemes to determine how the various schemes compare.

8.3.1. Fitted distribution parameters in the rain region (T > 0 °C)

Below the melting layer in the 29 May case, the PASIV sampled rather inconsistent particle concentrations that were a mix of rain and hail, however the layer shown in Figure 52 agrees well with the observed radar and makes for a confident analysis. In that layer, the exponential size distribution showed an intercept parameter of 280 m^{-3} mm^{-1}, or 2.8×10^5 m^{-4}, which is broadly comparable to the assumed inverse exponential rain intercept value of 8×10^5 m^{-4} as deduced for a supercell storm simulation (Ziegler et al. 2010) and as adapted to the development and application of the diabatic Lagrangian analysis technique for deep precipitating convection (Ziegler 2013a,b). It is noted that strong or supercellular deep convective storms typically contain relatively low concentrations of rather large graupel/hail-meltwater raindrops, and thus are expected to be characterized by significantly smaller rain intercept values than would be observed in the trailing stratiform regions of mesoscale convective

systems or within winter storms. The latter observed rain intercept values are also comparable although somewhat low in relation to the average values found in the Morrison et al. (2009) two-moment microphysics simulations for a trailing stratiform rain region, which is not unexpected given that the 29 May rainfall is associated with heavy convective precipitation including melting graupel and hail as opposed to melting small ice particles that are typically associated with stratiform regions. The 21 June case showed a similar behavior with an intercept parameter of 6.81×10^5 m^{-4}, with the sampled precipitation region in the latter case possibly being somewhat closer in character to a trailing stratiform rain region than the 29 May case but nevertheless rather similar to the DLA-assumed rain intercept value (Figure 34).

The inverse exponential rain intercept values in both cases were largely constant throughout the rain layer. However, while these values appear to agree reasonably well with the simulations from Ziegler et al. (2010) and Morrison et al. (2009) and the DLA, the observed raindrop size distributions in the 21 June and 29 May cases are rather better represented by the three-parameter gamma distribution function. In fact, for all DSDs examined in each layer of the rain region (not shown), the gamma distribution better represents the observations than the inverse exponential distribution (Willis 1984). Smith (2003) argued that the differences between these functions was largely irrelevant and that the improvements rendered by the increased number of fitted parameters were within the experimental uncertainties of the observed rain DSDs. While this may be a relevant point for the small diameters of the DSD, the exponential distribution also overestimates the concentrations at larger diameters which would have an impact on modeled microphysical processes. For this reason, it is speculated that

modeling studies generally may benefit from the inclusion of a triple-moment microphysics scheme at least in the rain layer. In such a study, the variation in the intercept of the gamma function could then be compared against the observations presented here.

The slope parameter values of the exponential distributions for both cases also appear to agree reasonably well with previous observations. Uijlenhoet et al. (2003) reported exponential slope values in the 2-4 mm^{-1} range throughout their observations across a squall line passage. Here, the exponential slopes of both cases were on the order of 3 mm^{-1}, making these cases comparable to the transition zone sampled by Uiklenhoet et al. (2003). The slopes of the gamma distributions for the 21 June and 29 May cases are also roughly comparable to their transition zone. Values of 10-15 mm^{-1} are common across both cases while the Uijlenhoet et al. (2003) averaged 10 mm^{-1} with a few peaks up to 15 mm^{-1}.

It should be noted that both cases revealed a large variability of the shape parameter with the rain region. This is partly due to the widely dispersed, low concentrations in the sampled DSDs. For the 29 May case, the shape parameters were generally high, averaging around 15. The 21 June case saw lower shape values on the order of 10-15. This is considerably higher than the values reported in Milbrandt and Yao (2005) and Uijlenhoet et al. (2003) who observed shape parameters between 2 and 5 for stratiform and convective regions respectively. The larger shape parameters in the present study reflect the increased width of the PASIV-observed distributions in the environments sampled. The general agreement of the present gamma and exponential distributions with previously reported work lends confidence to the PASIV-sampled

DSDs. It also reinforces the case that the gamma distribution, despite its added complexity, is a better fit for rain DSDs.

8.3.2. Fitted distribution parameters in the ice region (T < 0 ° C)

In the ice region of the 29 May supercell, the distribution shown in Figure 53 allows a comparison against previously observed graupel concentrations. While the distribution isn't entirely consistent of graupel, a significant portion of the larger diameters are due to the observed graupel particles. Gilmore et al. (2004b) reported results from previous work that showed graupel concentrations in the range of 10^6-10^{10} m^{-4}. The layer examined at 5.75 km showed an exponential intercept parameter of 2.108×10^6 for the total distribution, within the range previously reported. Here the exponential and gamma functions showed similar intercept parameters, though the exponential distribution was generally more representative. Properly representing the amount of graupel/hail in a severe storm is critical when performing modeling studies, as Gilmore et al. (2004b) showed that large variations in the ground-accumulated precipitation can occur with slight changes in the parameters describing those distributions. The observations presented here lend support to microphysical model formulations and simulated precipitation particle distributions.

Throughout the ice region in both cases the slope parameters not only converge to similar values within each case, but also show very little variation despite the changes in the particle types that occur throughout the sampled profile. The low values indicate a concentration that is widely distributed with comparable concentrations of both small and large particle diameters. Higher slope values, such as those found in the rain region, would indicate a higher ratio of small particles relative to the larger ones.

In the anvil region of tropical convection, Gallagher et al. (2012) found that the slope of their fitted exponential distributions (a gamma function was used with an assumed shape parameter of 0) was largely constant with distance from the storm. They postulated that this suggested a balance between large ice crystal production and their subsequent removal by sedimentation. In contrast, McFarquhar et al. (2007) found strong evidence of aggregation of predominantly irregular ice particles in the trailing stratiform regions of MCSs during BAMEX that produced rather broad Gamma size distributions characterized by slope parameters in the range of 0.5 - 1.5 mm^{-1} and shape parameters in the range of -2 to 0.

Given that a similar low slope behavior is noted here, a similar suggestion can be made that the distributions are held relatively constant due to the continued production and advection of larger ice crystals. Gallagher et al. (2012) also mention in their discussion that their distributions were approximately exponential (hence assuming a shape parameter of 0), an observation validated by the cases presented here. It is interesting however that the slopes of the various functions do not decrease much below roughly 2 mm^{-1}. Heymsfield et al. (2008) suggested that the lower limit for exponential distribution slopes of roughly 0.9 mm^{-1} that has been observed before is largely due to particle shattering associated with aircraft PSD measurements. These shattered particles increase the concentrations of small particles at the expense of the larger ones. Once removed, values lower than 0.9 mm^{-1} were possible. Given that such low values are not sampled in either case presented here, and that particle shattering is likely not a significant problem with the slower ascending balloon-borne PASIV, the suggestion that particles of all diameters are continually produced in these observations

is reinforced. Without the production of smaller ice particles, the distribution would broaden and the slope decrease as smaller crystals aggregated to form larger particles. Indeed as previously noted, McFarquhar et al. (2007) found strong evidence of aggregation of predominantly irregular ice particles in MCS trailing stratiform regions, which observations and models of stratiform snow fields have demonstrated tends to reduce both the intercept and slope parameters as aggregation reduces total concentration without changing mixing ratio (e.g., Passarelli 1978a,b).

8.4 Electric field profiles in the context of precipitation microphysics

The electric field exhibited very different profiles in the 21 June and 29 May cases, but also consistently showed changes in the electric field and associated charge layer structure that corresponded to changes in the respective particle distributions. For the 29 May case, the main charge layer was negative and centered on the higher concentrations of graupel particles observed in the sounding. As the particle concentrations of graupel decreased and the concentrations of irregular ice crystals increased, the charge structure changed to a positive layer. Although the 21 June case did not have as much graupel present, the largest charge layer in the sounding coincided with the higher concentrations and larger sizes of the irregular ice crystals and was also positive. Thus both cases showed layers containing significant net positive charge in regions with large irregular ice crystals and numerous small regular ice crystals.

While it is difficult to place the 29 May electrical structure into context due to the incomplete sounding, the 21 June electrical structure loosely resembles that of a Type A MCS as discussed in Marshall and Rust (1993). It has previously been noted that although the 21 June case was dominated by a field of rather weak, pulsing deep

convective updrafts, the 21 June sounding appears to have penetrated relatively decayed regions outside of precipitation cores that were dominated by absence of updraft combined with precipitation fallout, high ice concentrations, and a relative paucity of graupel with possible broad similarity to an MCS trailing stratiform region. Their Type A MCS structure was characterized by four charge regions, alternating between positive and negative layers, with a bottom negative charge layer near 0°C. There was also a fifth charge layer at the top of their structure that was hypothesized to be caused by an electrical screening layer effect. The present 21 June case reveals four charge regions, the lowest of which is a negative layer. The largest difference between the soundings is that the charge regions in this case do not occur until nearly 2 km above the freezing level. Furthermore, the final positive charge layer at the top of the electric structure does not occur at the top of the particle structure.

The last charge layer ends at approximately 10 km, whereas particles are detected until nearly 11.5 km. This would indicate that this layer is not a conventional screening layer since it occurs well within the precipitation boundary. The remaining charge is detected as the concentrations of the irregular ice crystals begin to drop off. Once concentrations drop below roughly 50 m^{-3}, no further charge is observed. Although there are still high total concentrations of regular ice particles on the order of 1000 m^{-3} in the layer between 10 km and 11.5 km, radar reflectivity as determined from the camera PSD shows values below 10 dBZ and bulk charge is absent. This suggests that the particles in the 10 - 11.5 km layer were neither previously nor currently involved in any charging mechanisms while potentially growing locally by vapor

deposition. As no charge was present near the cloud boundary, no screening layer charge was formed.

Chapter 9

Conclusions

This study presents the stages of design, testing, validation, and deployment of a high definition balloon-borne particle imaging device known as the National Severe Storms Laboratory (NSSL) PArticle Size, Image, and Velocity (PASIV) probe, and the scientific analyses of PASIV observations obtained in convective storms. The motivation behind the creation of this instrument lies in the significant need for in situ microphysics observations inside severe convection and other precipitating mesoscale cloud systems. With applications in storm structure, microphysical parameterization, cloud modeling, radar analysis, dual-polarization radar validation, hydrometeor classification, and electrification research, these observations are critical to the continuing body of work involving in situ microphysics observations. The observations presented here have illuminated the importance and need for high resolution in situ measurements of the particle size distribution. The unparalleled finescale observations of the PASIV shed light on the microstructure of precipitation within severe convection and provide the opportunity to conduct more detailed analysis of in situ storm microphysics in combination with microphysical measurements from other in situ platforms including the NOAA P-3 and the NSF .A-10 storm penetration aircraft (SPA).

9.1 Precipitation microphysics

The PASIV, while not the first balloon-borne videosonde, represents a significant advancement in its ability to obtain high spatio-temporal resolution microphysics observations. Whereas previous in situ measurements primarily from

aircraft have been capable of observations over scales on the order of kilometers, the PASIV is capable of particle size distributions over scales as small as 50 m. In comparison to other videosondes, many previous sounding-based studies have observed up to order 10^2 particles per flight whereas the PASIV observes on the order of 10^5 particles per flight. The high resolution data collected in the two cases presented has shown that there are large changes in the concentrations of particles on a vertical length scale as small as 50 m. Furthermore, with the development of automated classification algorithms for the data collected, these distributions can be parsed into the distinct particle habits of raindrops, graupel/hail, and regular and irregular ice particles.

Combining the particle data from both the camera and the Parsivel on the 21 June case allowed for the validation of various assumed theoretical particle fall speed relations. The particles observed and classified by the camera system provided a similar velocity distribution (i.e., via the theoretical fall speed relations) to the non-classified velocity distribution from the Parsivel. Thus the theoretical fall speed relations, which are largely based of surface observations and corrected for altitude, appear to be reasonable approximations for the observed velocities of in situ particles.

When comparing the observations against available radar, it was found that the reflectivity is largely dominated by graupel particles whenever present, despite higher concentrations of other lower density ice particles. In general, the radar reflectivity found from the PASIV distributions was within a few dBZ of the observed mobile radar values. The only significant difference occurred in the rain regions where low particle concentrations contributed to the erroneously low radar reflectivity values from the PASIV. This serves to highlight one of the limiting factors of the PASIV instrument.

The PASIV also suggests that while comparable, mixing ratio values for the various particle types are higher in observations than those assumed in some bulk microphysics packages that are commonly used in storm scale modelling. In addition, several particle layers were examined in detail to provide an in-depth analysis of the shape of the distribution and the function fits of exponential or gamma type assumed forms. This analysis suggests that for the rain region, the gamma distribution is a better approximation for the observed distribution than the exponential. In the ice phase region however, the gamma distribution trended towards the exponential distribution and suggests that the added complexity is not required for ice particle classes. The values of the parameters for the two distributions are largely in agreement with previous observations and values used in various modelling studies, providing confidence to those assumed distributions in microphysics schemes. Overall, the PASIV observations suggest room for improvement and refinement on which bulk microphysics schemes are applicable in various environments.

9.2 Ambient microphysical properties in strongly electrified storm environments

In a final analysis the detailed microphysics observations were compared against simultaneous in situ electric field observations. The 29 May sounding showed high concentrations of graupel particles coinciding with a layer of negative charge, providing in situ verification of the non-inductive charging mechanism involving collisions with graupel dependent on the environmental temperature (Reynolds, et al., 1957; Takahashi, 1978; Saunders, et al., 1991; Saunders, 1993; MacGorman & Rust, 1998; Takahashi et al., 1999). Furthermore, positive charge layers were documented in regions characterized by higher concentrations, and larger sizes, of the irregular ice crystals.

This supports the observations made by Takahashi et al. (1999) in Japan, but does so with more detail regarding the microphysical structure. Indeed the larger magnitude charge regions are associated with broader particle sizes in which the larger particles carry more charge.

9.3 Random Forest Training Dataset

A large focus of the PASIV probe is the ability to discern various particle habits through the use of a random forest classifier. As was discussed previously, there are a variety of visual factors that a human operator uses to determine what class a particular particle should fall into. Given the lack of a priori knowledge of where splits in these various predictor variables should occur, a random forest classifier is an excellent choice for the automated classification task. The setup and operation of this classifier was discussed in section 5.3.3.2 Random Forest classification method, however a specific discussion on the training data set is warranted here.

In order to build the training data set used to generate the forest for the random forest method, and to test its accuracy, a series of particles were hand classified. This process is both incredibly time consuming and tedious. An effort was made to include particles from both cases to be analyzed, and to not intentionally favor any specific class by adding more of a specific particle type. Images were chosen largely at random and particles identified and classified. Once the training data set reached its current size of roughly 650 objects, the classifier was run and the accuracy was found to be acceptable. Furthermore, the classifier was run on both cases and the results examined for logical consistency, as well as random particles examined to verify that the classifier was indeed working properly.

While the results of the classification appear to be accurate and consistent with physical expectations, and calculations performed using these classifications agree with independent measurements (radar analysis), the fact remains that a training data set of roughly 650 objects was used to train a forest which is being applied to roughly 8 million objects. An argument could be made that the classifier may be subject to bias present in the training data set and that the size of the training data is small enough to question the robustness of the random forest. While a potentially valid criticism, examination of the training data with respect to the population data and sensitivity tests performed on the classifier prove this to be unlikely.

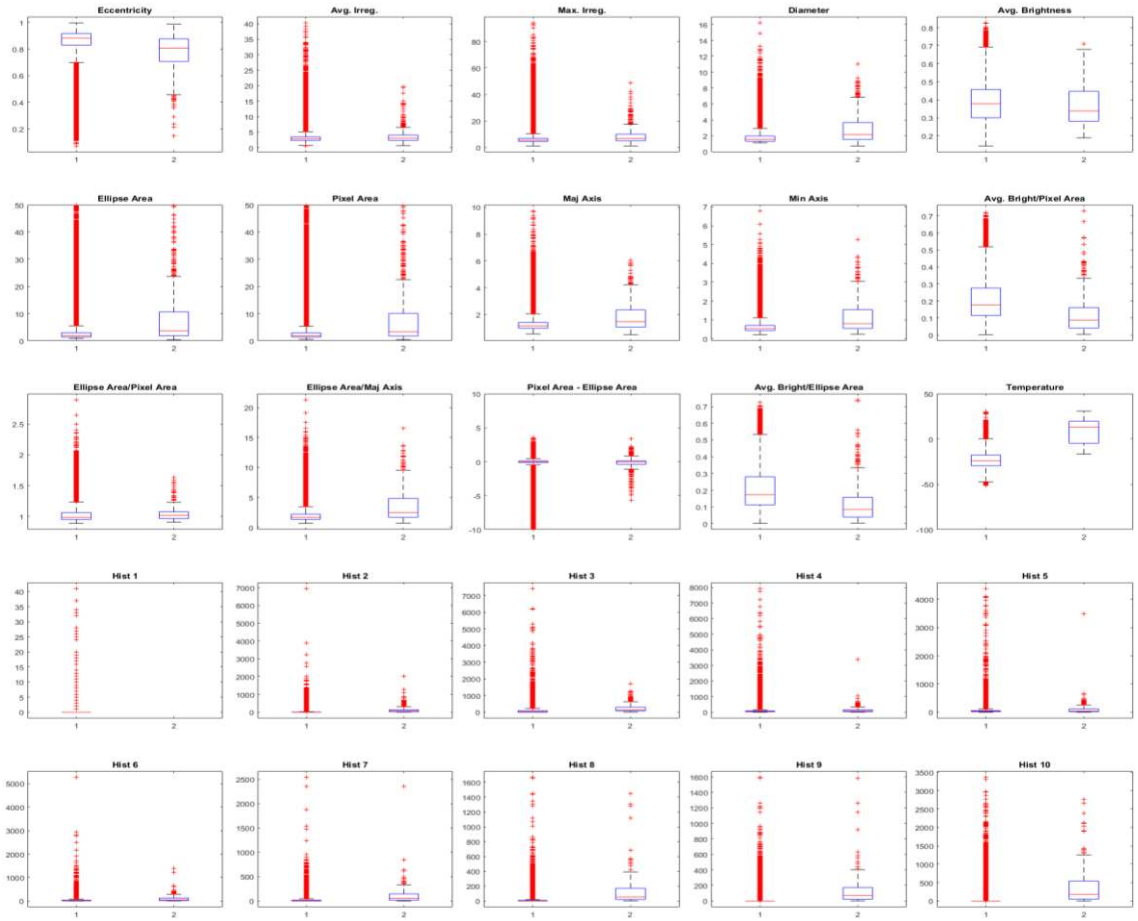

Figure 67. Distribution plot showing the population data (1) and the training data (2) for each of the predictor variables listed in Table 4 (excluding the binary graph type predictor). Each box represents the 25th and 75th percentile of the distribution, while the whiskers extend to +/-2.7 standard deviations.

To address the potential concern regarding any bias in the training data, it is useful to examine how the distributions of the various predictor variables compare between the population and the training data (Figure 67). In the figure it is apparent that for a majority of the predictor variables, the training data set covers a comparable range to the population data. While there are extremes in the population data that extend well beyond the training data assembled, these represent only a handful of cases. The only predictor that is significantly different between the training and population data is the environmental temperature of the particle. This difference is largely caused by the overwhelming number of ice particles present in the population data and the extremely cold temperatures of the 21 June case compared to the 29 May case, which has a tendency to shift the distribution of the population toward colder temperatures. There is a physical constraint at 0°C however that controls the distinction between liquid and frozen particles, and post classification cleanup is used to adjust these classifications as the random forest classifier is not aware of this physical constraint.

To address the sensitivity of the classification method to variations in the training data, a Monte Carlo approach was used where the random forest was generated and tested using a random subset of the training data 5000 times and the skill scores for the various particle classes computed at each iteration. These skill scores were then bootstrapped and the mean value recorded an additional 5000 times. The results show that the 95% confidence interval of the skill scores is focused on the reported value for each class (Figure 68). This demonstrates that the random forest classifier is not sensitive to the subset of the training data used for building the forest and provides confidence for using the random forest classifier moving forward.

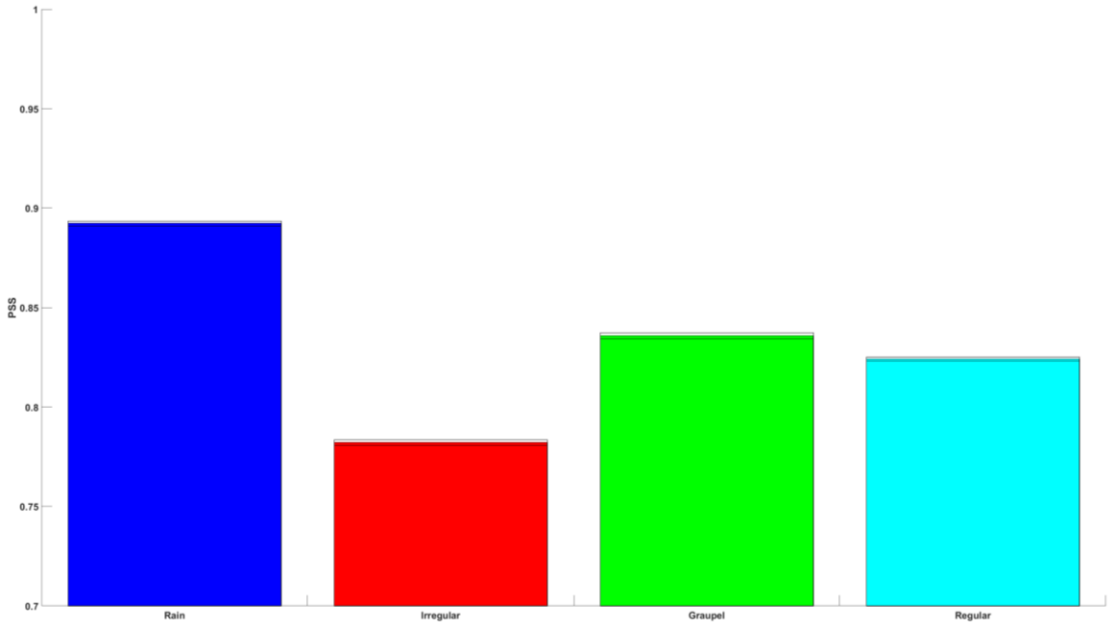

Figure 68. Peirce Skill Scores for the random forest classifications of rain (dark blue), irregular (red), graupel (green), and regular (cyan) particles. The 95% confidence interval of each skill score is shown, and the figure is zoomed to show these limits.

9.4 Future work

While the PASIV probe represents a significant advancement in the field of balloon-borne microphysics observations, and microphysics observations in general, it is also largely a prototype. The instrument, the launching sequence, the software to process the data, everything involving this device had to be designed from the ground up as no observational platform like this existed prior to the PASIV's development. While the PASIV in its current form is capable of high resolution observations, there are also a number of improvements and future research endeavors that give the instrument direction and advancement.

The two cases presented are only scratching the surface of the information contained within the particle data. If a DLA was performed on the 21 June case, particle trajectories and model comparisons for both 21 June and 29 May would be possible. Particle trajectories would be useful in determining where the observed

particles originated within the convection, particularly with reference to their inferred electrical charge. Utilization of the dual-polarization measurements available in both cases, as well as comparisons with the hydrometeor classification algorithms available would add more depth to either analysis. Furthermore, breaking down the particle classifications further and exploring individual functional fits to specific particle types would be an extremely useful exercise for comparisons with model assumptions.

While the body of work presented here pushes microphysics observations to a level of detail not previously achieved, the analysis here was done using only two cases. As it stands currently, there have been nearly two dozen successful launches of the PASIV probe into a wide range of precipitating environments, many of which bear examination. A recent project during the summer in Florida presented several cases where PASIV data could be compared against mobile radar observations in maritime convection. Comparing the observations across a wide spectrum of convective precipitation events, and a wide range of geographical regions would serve to highlight consistent patterns in the microphysics observations particularly with reference to modeled microphysics.

A limiting factor of the current PASIV lies in the resolution of the camera and the ability to clearly image objects. Upgrading the platform to a 4k resolution camera is currently underway. Doing so will require a redesign of the instrument body and the addition of more dispersed light sources. This added resolution may allow for the distinction of additional particle classes, as well as the ability to identify riming on particles when present. The next version of the PASIV will allow for even higher

resolution, and more accurate, PSD measurements with which additional research can be done for years to come.

References

Battaglia, A., E. Rustemeier, A. Tokay, U. Blahak, and C. Simmer, 2010: PARSIVEL snow observations: A critical assessment. *J. Atmos. Oceanic Tech.*, **27**, 333–344.

Beard, K. V., 1977: Terminal velocity and shape of cloud and precipitation drops aloft. *J. Atmos. Sci.*, **34**, 1293–1298.

Biggerstaff, Michael I., Louis J. Wicker, Jerry Guynes, Conrad Ziegler, Jerry M. Straka, Erik N. Rasmussen, Arthur Doggett IV, Larry D. Carey, John L. Schroeder, and Chris Weiss, 2005: The Shared Mobile Atmospheric Research and Teaching Radar: A Collaboration to Enhance Research and Teaching. *Bull. Amer. Meteor. Soc.*, **86:9**, 1263-1274.

Böhm, H. P., 1989: A general equation for the terminal fall speed of solid hydrometeors. *J. Atmos. Sci.*, **46**, 2419–2427.

Boussaton, M. P., S. Coquillat, S. Chauzy, and F. Gangneron, 2004: A new videosonde with a particle charge measurement device for in situ observation of precipitation particles. *J. Atmos. Oceanic Tech.*, **21**, 1519–1531.

Breiman, L, 2001: Random Forests. *Machine Learning*, **45**, 5-32.

Bruning, E. C., W. D. Rust, T. J. Schuur, D. R. MacGorman, P. R. Krehbiel, and W. Rison, 2007: Electric and Polarimetric Radar Observations of a Multicell Storm in TELEX. *Mon. Wea. Rev.,* **135**, 2525-2544.

Bruning, E. C., W. D. Rust, D. R. MacGorman, M. I. Biggerstaff, and T. J. Schuur, 2010: Formation of Charge Structures in a Supercell. *Mon. Wea. Rev.,* **138**, 3740-3761.

Cao, Q., G. Zhang, E. A. Brandes, T. J. Schuur, A. Ryzhkov, and K. Ikeda, 2008: Analysis of video disdrometer and polarimetric radar data to characterize rain microphysics in Oklahoma. *J. Appl. Meteor. Climatol.*, **47**, 2238–2255.

Cao, Q., G. Zhang, E. A. Brandes, and T. J. Schuur, 2010: Polarimetric radar rain estimation through retrieval of drop size distribution using a Bayesian approach. *J.*

Appl. Meteor. Climatol., **49**, 973–990.

Chen, C., A. Liaw, and L. Breiman, 2004: Using Random Forest to Learn Imbalanced Data. *Statistics Technical Reports*, **666**, 1-12.

Elmore, Kimberly L., 2011: The NSSL Hydrometeor Classification Algorithm in Winter Surface Precipitation; Evaluation and Future Development. *Wea. Forecasting*, **26**, 756-765.

Emersic, C., and C. P. R. Saunders, 2010: Further laboratory investigations into the relative diffusional growth rate theory of thunderstorm electrification. *Atmos. Res.*, **98**, 327-340.

Fanning, David, 2003: Fit Ellipse. Accessed 29 June 2016. [Available online at http://www.idlcoyote.com/ip_tips/fit_ellipse.html.]

Fernández-Delgado, M., E. Cernadas, and S. Barro, 2014: Do we Need Hundreds of Classifiers to Solve Real World Classification Problems?. *J. Mach. Learn. Res.*, **15**, 3133-3181.

Ferrier, B. S., 1994: A double-moment multiple-phase four-class bulk ice scheme. Part I: Description. J. Atmos. Sci., 51, 249–280.

Friedrich, K., E. A. Kalina, F. J. Masters, and C. R. Lopez, 2013: Drop-size distributions in thunderstorms measured by optical disdrometers during VORTEX2. *Mon. Wea. Rev.,* **141**, 1182–1203.

Gallagher, M. W., P. J. Connoly, I. Crawford, A. Heymsfield, K. N. Bower, T. W. Choularton, G. Allen, M. J. Flynn, G. Vaughan, and J. Hacker, 2012: Observations and modelling of microphysical variability, aggregation and sedimentation in tropical anvil cirrus outflow regions. *Atmos. Chem. Phys.*, **12**, 6609-6628.

Gagne II, J. D., A. McGovern, J. Basara, and R. Brown, 2012: Tornadic Supercell Environments Analyzed Using Surface and Reanalysis Data: A Spatiotemporal Relational Data-Mining Approach. *J. Appl. Meteor. Climatol.,* **51**, 2203-2217.

Giangrande, S. E., J. M. Krause, and A. V. Ryzhkov, 2008: Automatic Designation of the Melting Layer with a Polarimetric Prototype of the WSR-88D Radar. *J. Appl. Meteor. Climatol.*, **47**, 1354–1364.

Gilmore, M. S., J. M. Straka, and E. N. Rasmussen, 2004a: Precipitation and evolution sensitivity in simulated deep convective storms: Comparisons between liquid-only and simple ice and liquid phase microphysics. *Mon. Wea. Rev.*, **132**, 1897-1916.

Gilmore, M. S., J. M. Straka, and E. N. Rasmussen, 2004b: Precipitation uncertainty due to variation in precipitation particle parameters within a simple microphysics scheme. *Mon. Wea. Rev.*, **132**, 2610-2627.

Grossklaus, M., K. Uhlig, and L. Hasse, 1998: An optical disdrometer for use in high wind speeds. *J. Atmos. Oceanic Technol.,* **15**, 1051–1059.

Gunn, R., and G. D. Kinzer, 1949: The terminal velocity of fall for water droplets in stagnant air. *J. Meteor.*, **6**, 243–248.

Hallett, J., and S. C. Mossop, 1974: Production of secondary ice particles during the riming process. *Nature*, **249**, 26-28, doi:10.1038/249026a0

Habib, E., W. F. Krajewski, and A. Kruger, 2001: Sampling errors of tipping-bucket rain gauge measurements. *J. Hydrol. Eng.,* **6**, 159–166.

Heinselman, Pamela L., and Alexander V. Ryzhkov, 2006: Validation of Polarimetric Hail Detection. *Wea. Forecasting*, **21**, 839-850.

Heymsfield, Andrew J., 1978: The characteristics of graupel particles in northeastern Colorado cumulus congestus clouds. *J. Atmos. Sci.*, **35**, 284–295.

Heymsfield, A. J., P. N. Johnson, and J. E. Dye, 1978: Observations of moist adiabatic ascent in northeast Colorado cumulus congestus clouds. *J. Atmos. Sci.*, **35**, 1689–1703.

Heymsfield, A. J. and D. J. Musil, 1982: Case study of a hailstorm in Colorado. Part II: Particle growth processes at mid-levels deduced from in-situ measurements. *J. Atmos. Sci.*, **39**, 2847–2866.

Heymsfield, A. J., and J. C. Pflaum, 1985: A quantitative assessment of the accuracy of techniques for calculating graupel growth. *J. Atmos. Sci.*, 42, 2264–2274.

Heymsfield, A. J., P. Field, and A. Bansemer, 2008: Exponential size distributions for snow. *J. Atmos. Sci.*, **65**, 4017–4031.

Heymsfield, A. J., C. Schmitt, and A. Bansemer, 2013: Ice cloud particle size distributions and pressure-dependent terminal velocities from in situ observations at temperatures from 0° to −86°C. *J. Atmos. Sci.*, **70**, 4123–4154.

Heymsfield, A. and R. Wright, 2014: Graupel and Hail Terminal Velocities: Does a "Supercritical" Reynolds Number Apply?. *J. Atmos. Sci.*, **71**, 3392–3403.

Hosler, C. L., D. C. Jensen and L. Goldshlak, 1957: On the aggregation of ice crystals to form snow. *J. Meteor.*, **14**, 415-420.

Huntrieser, H. and coauthors, 2016: Injection of lightning-produced NO_x, water vapor, wildfire emissions, and stratospheric air to the UT/LS as observed from DC3 measurements. *J. Geophys. Res.,* **121**, doi:10/1002/2015JD024273.

Johnson, Marcus, Youngsun Jung, Daniel T. Dawson II, and Ming Xue, 2016: Comparison of Simulated Polarimetric Signatures in Idealized Supercell Storms Using Two-Moment Bulk Microphysics Schemes in WRF. *Mon. Wea. Rev.*, **144**, 971-996.

Jorgensen, D. P., and P. T. Willis, 1982: A Z-R relationship for hurricanes. *J. Appl. Meteor.,* **21**, 356–366.

Jung, Y., G. Zhang, M. Xue, 2008: Assimilation of Simulated Polarimetric Radar Data for a Convective Storm Using the Ensemble Kalman Filter. Part I: Observation Operators for Reflectivity and Polarimetric Variables. *Mon. Wea. Rev.,* **136**, 2228–2245.

Jung, Y. M. Xue, G. Zhang, 2010: Simulations of Polarimetric Radar Signatures of a Supercell Storm Using a Two-Moment Bulk Microphysics Scheme. *J. Appl. Meteor. Climatol.,* **49**, 146-163.

Kalina, Evan A., Katja Friedrick, Scott M. Ellis, and Donald W. Burgess, 2014: Comparison of Disdrometer and X-Band Mobile Radar Observations in Convective Precipitation. *Mon. Wea. Rev.*, **142:7**, 2414-2435.

Knight, C. A., and N. C. Knight, 2005: Very large hailstones from Aurora, Nebraska. *Bull. Amer. Meteor. Soc.*, **86:12**, 1773-1781.

Knight, C. A., P. T. Schlatter, and T. W. Schlatter, 2008: An unusual hailstorm on 24 June 2006 in Boulder, Colorado. Part II: low-density growth of hail. *Mon. Wea. Rev.*, **136**, 2833-2848.

Kouketsu, T., H. Uyeda, T. Ohigashi, M. Oue, H. Takeuchi, T. Shinoda, K. Tsuboki, M. Kubo, and K. Muramoto, 2015: A Hydrometeor Classification Method for X-Band Polarimetric Radar: Construction and Validation Focusing on Solid Hydrometeors under Moist Environments. *J. Atmos. Oceanic Technol.,* **32**, 2052–2074.

Kruger, A., and W. F. Krajewski, 2002: Two-dimensional video disdrometer: A description. *J. Atmos. Oceanic Technol.,* **19**, 602–617.

Liu, X. C., T. C. Gao, and L. Liu, 2014: A video precipitation sensor for imaging and velocimetry of hydrometeors, *Atmos. Meas. Tech.,* **7**, 2037-2046.

Löffler-Mang, M., and J. Joss, 2000: An optical disdrometer for measuring size and velocity of hydrometeors. *J. Atmos. Oceanic Technol.,* **17**, 130–139.

Löffler-Mang, M., and U. Blahak, 2001: Estimation of the equivalent radar reflectivity factor from measured snow size spectra. *J. Appl. Meteor.,* **40**, 843–849.

MacGorman, D. R., and W. D. Rust, 1998: *The Electrical Nature of Storms,* Oxford University Press, 422 pp.

Macklin, W. C., 1962: The density and structure of ice formed by accretion. *Quart. J. Roy. Meteor. Soc.*, 88, 30–50.

Mahlke, H., U. Corsmeier, C. Kottmeier, and M. Löffler-Mang, 2008: The new balloon-borne disdrometer 'Flying Parsivel'. 7th COPS Workshop, Strasbourg, France, Karlsruhe Institute of Technology. [Available online at https://www.imk-tro.kit.edu/download/Poster_Flying_Parsivel.pdf.]

Mansell, Edward R., Conrad L. Ziegler, and Eric R. Bruning, 2010: Simulated Electrification of a Small Thunderstorm with Two-Moment Bulk Microphysics. *J. Atmos. Sci.*, **67**, 171–194.

Marshall, T. C., & W. D. Rust, 1993: Two Types of Vertical Electrical Structures in Stratiform Precipitation Regions of Mesoscale Convective Systems. *Bull. Amer. Meteor. Soc.*, **74**, 2159-2170.

McFarquhar, G. M., M. S. Timlin, R. M. Rauber, B. F. Jewett, J. A. Grim, and D. P. Jorgensen, 2007: Vertical variability of cloud hydrometeors in the stratiform region of mesoscale convective systems and bow echoes. *Mon. Wea. Rev.,* **135**, 3405–3428.

McGovern, A., D J. Gagne II, J. K. Williams, R. A. Brown, and J. B. Basara, 2013: Enhancing understanding and improving prediction of severe weather through spatiotemporal relational learning. *Machine Learning*, **95**, 27-50

Milbrandt, J. A. and M. K. Yau, 2005: A Multimoment Bulk Microphysics Parameterization. Part II: A Proposed Three-Moment Closure and Scheme Description. *J. Atmos. Sci.*, **62**, 3065-3081.

Miloshevich, L. M., and A. J. Heymsfield, 1997: A Balloon-borne continuous cloud particle replicator for measuring vertical profiles of cloud microphysical properties: Instrument design, performance, and collection efficiency analysis. *J. Atmos. Oceanic Technol.*, **14**, 753–768.

Morrison, Hugh and Jason Milbrandt, 2011: Comparison of Two-Moment Bulk Microphysics Schemes in Idealized Supercell Thunderstorm Simulations. *Mon. Wea. Rev.*, **139**, 1103-1130

Morrison, H., G. Thompson, and V. Tatarskii, 2009: Impact of Cloud Microphysics on the Development of Trailing Stratiform Precipitation in a Simulated Squall Line: Comparison of One- and Two-Moment Schemes. *Mon. Wea. Rev.*, **137**, 991-1007

Murakami, M., T. Matsuo, T. Nakayama, and T. Tanaka, 1987; Development of cloud particle video sonde. *J. Meteor. Soc. Japan,* **65**, 803-809.

Murakami, M., and T. Matsuo, 1990: Development of the hydrometeor videosonde. *J. Atmos. Oceanic Technol.,* **7**, 613–620.

Musil, D. J., W. R. Sand, and R. A. Schleusener, 1973: Analysis of data from T-28 aircraft penetrations of a Colorado hailstorm. *J. Appl. Meteor.,* **12**, 1364–1370.

Musil, D. J., A. J. Heymsfield, and P. L. Smith, 1986: Microphysical characteristics of a well-developed weak echo region in a high plains supercell thunderstorm. *J. Appl. Meteor. Climatol.,* **25**, 1037–1051.

Norment, H. G., 1988: Three-dimensional trajectory analysis of two drop sizing instruments: PMS* OAP and PMS* FSSP. *J. Atmos. Ocean. Tech.,* **5**, 743–756.

Ogliore, R., C. Floss, F. Stadermann, A. Kearsley, J. Leitner, R. Stroud, and A. Westphal, 2012: Automated searching of stardust interstellar foils. *Meteor. and Planetary Sci.,* **47**, 729-736.

Passarelli, Richard E. Jr., 1978a: An approximate analytical model of the vapor deposition and aggregation growth of snowflakes. J. Atmos. Sci., 35, 118-124.

Passarelli, Richard E. Jr., 1978b: Theoretical and observational study of snow-size spectra and snowflake aggregation efficiencies. J. Atmos. Sci., 35, 882-889.

Park, Hyang Suk, A. V. Ryzhkov, D. S. Zrnić, and K. Kim, 2009: The Hydrometeor Classification Algorithm for the Polarimetric WSR-88D: Description and Application to an MCS. *Wea. Forecasting*, **24:3**, 730-748.

Pruppacher, H. R., and J.D. Klett, 1997: *Microphysics of Clouds and Precipitation* (2nd ed.). Kluwer Academic Press, 954 pp.

Reinhart, B., H. Fuelberg, R. Blakeslee, D. Mach, A. Heymsfield, A. Bansemer, S. L. Durden, S. Tanelli, G. Heymsfield, and B. Lambrigtsen, 2014: Understanding the

Relationships between Lightning, Cloud Microphysics, and Airborne Radar-Derived Storm Structure during Hurricane Karl (2010). *Mon. Wea. Rev.,* **142**, 590–605.

Reynolds, S. E., Brook, M. & Gourley, M. F., 1957: Thunderstorm Charge Separation. *J. Meteor.,* **14**, 426-436.

Rust, W. D., and T. C. Marshall, 1989: Mobile, high-wind, balloon-launching apparatus. *J. Atmos. Oceanic Technol.*, **6**, 215–217.

Saunders, C. P. R., 1993: A Review of Thunderstorm Electrification Processes. *J. Appl. Meteor.,* **32**, 642–655.

Saunders, C., 2008: Charge separation mechanisms in clouds. *Space Sci. Rev.*, **137**, 335-353.

Saunders, C. P. R., Keith, W. D. & Mitzeva, R. P., 1991: The effect of liquid water on thunderstorm charging. *J. Geophys. Res.,* **97**, 11007-11017.

Saunders, C. and S. L. Peck, 1998: Laboratory studies of the influence of the rime accretion rate on charge transfer during crystal/graupel collisions. *J. Geophys. Res.*, **103**, 13949-13956.

Schuur, T. J., A. V. Ryzhkov, D. S. Zrnić, and M. Schönhuber, 2001: Drop size distributions measured by a 2D video disdrometer: Comparison with dual-polarization radar data. *J. Appl. Meteor.*, **40**, 1019–1034

Schuur, T. J., B. F. Smull, W. D. Rust, and T. C. Marshall, 1991: Electrical and Kinematic Structure of the Stratiform Precipitation Region Trailing an Oklahoma Squall Line. *J. Atmos. Sci.,* **48**, 825-842.

Smith, Paul L., 2003: Raindrop size distributions: exponential or gamma – does the difference matter? *J. Appl. Meteor.*, **42**, 1031–1034

Smith, A. M., G. M. McFarquhar, R. M. Rauber, J. A. Grim, M. S. Timlin, B. F. Jewett, and D. P. Jorgensen, 2009: Microphysical and thermodynamic structure and evolution of the trailing stratiform regions of mesoscale convective systems during BAMEX. Part

I: Observations. *Mon. Wea. Rev.,* **137**, 1165–1185.

Straka, J. M., D. S. Zrnić, and A. V. Ryzhkov, 2000: Bulk Hydrometeor Classification and Quantification Using Polarimetric Radar Data: Synthesis of Relations. *J. Appl. Meteor.*, **39**, 1341–1372.

Straka, J. M., and E. R. Mansell, 2005: A bulk microphysics parameterization with multiple ice precipitation categories. *J. Appl. Meteor.*, **39**, 1341-1372.

Stewart, R. E., J. D. Marwitz, J. C. Pace, and R. E. Carbone, 1984: Characteristics through the melting layer of stratiform clouds. *J. Atmos. Sci.,* **41**, 3227-3237.

Takahashi, T., 1978: Riming electrification as a charge generation mechanism in thunderstorms. *J. Atmos. Sci.,* **35**, 1536-1548.

Takahashi, T., 1990: Near absence of lightning in torrential rainfall producing Micronesian thunderstorms. *Geophys. Res. Lett.,* **17**, 2381–2384.

Takahashi, T., T Tajiri, and Y. Sonoi, 1999: Charges on Graupel and Snow Crystals and the Electrical Structure of Winter Thunderstorms. *J. Atmos. Sci.,* **56**, 1561-1578.

Takahashi, T., 2010: The videosonde system and its use in the study of east asian monsoon rain. *Bull. Amer. Meteor. Soc.,* **91**, 1231–1246.

Thompson, E. J., S. A. Rutledge, B. Dolan, V. Chandrasekar, and B. L. Cheong, 2014: A Dual-Polarization Radar Hydrometeor Classification Algorithm for Winter Precipitation. *J. Atmos. Oceanic Technol.*, **31**, 1457-1481.

Ulbrich, C. W., and D. Atlas, 1998: Rainfall microphysics and radar properties: analysis methods for drop size spectra. *J. Appl. Meteor.*, **37**, 912-923.

Vardiman, Larry, 1978: The generation of secondary ice particles in clouds by crystal-crystal collision. *J. Atmos. Sci.,* **35**, 2168-2180.

Vivekanandan, J., W. M. Adams, and V. N. Bringi, 1991: Rigorous Approach to

Polarimetric Radar Modeling of Hydrometeor Orientation Distributions. *J. Appl. Meteor.*, **30**, 1053-1063.

Weverberg, K., A. M. Vogelmann, H. Morrison, and J. A. Milbrandt, 2012: Sensitivity of Idealized Squall-Line Simulations to the Level of Complexity Used in Two-Moment Bulk Microphysics Schemes. *Mon. Wea. Rev.*, **140**, 1883-1907.

Williams, John K., 2014: Using random forests to diagnose aviation turbulence. *Machine Learning*, **95**, 51-70.

Willis, Paul T., 1984: Functional Fits to some observed drop size distributions and parameterization of rain. J. Atmos. Sci., 41:9, 1648-1661.

Yano, J. –I. and V. T. J. Phillips, 2011: Ice-Ice Collisions: An ice multiplication process in atmospheric clouds. *J. Atmos. Sci.,* **68**, 322-333.

Yuter, S. E., D. E. Kingsmill, L. B. Nance, and M. Löffler-Mang, 2006: Observations of precipitation size and fall speed characteristics within coexisting rain and wet snow. *J. Appl. Meteor. Climatol.,* **45**, 1450–1464.

Zhang, G., J. Vivekanandan, and E. Brandes, 2001: A Method for Estimating Rain Rate and Drop Size Distribution from Polarimetric Radar Measurements. *IEEE Trans. Geo. Remote Sens.*, **39-4**, 830-841.

Zhang, G., M. Xue, Q. Cao, and D. Dawson, 2008: Diagnosing the intercept parameter for exponential raindrop size distribution based on video distrometer observations: model development. *J. Appl. Meteor. Climatol.,* **47**, 2983–2992.

Ziegler, C. L., E. Mansell, J. Straka, D. MacGorman, and D. Burgess, 2010: The impact of spatial variations of low-level stability on the life cycle of a simulated supercell storm. *Mon. Wea. Rev.*, **138**, 1738-1766.

Ziegler, C. L., 2013a: A diabatic Lagrangian technique for the analysis of convective storms. Part I: Description and validation via an observing system simulation experiment. *J. Atmos. Oceanic Technol.*, **30**, 2248-2265.

Ziegler, C. L., 2013b: A diabatic Lagrangian technique for the analysis of convective storms. Part II: Application to a radar-observed storm. *J. Atmos. Oceanic Technol.*, **30**, 2266-2280.

Appendix: Particle Glossary

A significant amount of work in developing the PASIV was spent on particle identification and classification. Being able to discern real objects from background noise, and properly identify their shape was the core of the initial development work. After the initial program was created and analysis began, it was decided that particle classification was also a requirement. A tremendous amount of effort was spent on identifying the necessary parameters to achieve automated particle classifications with reasonable accuracy as described in 5.3.3. Particle classification.

This appendix serves as a monument to that effort, documenting several examples of each particle type. Furthermore, in the course of analysis as individual images are examined, unique particles are often noted. These memorable particles are documented here to demonstrate the ability of the PASIV to sample and correctly identify a wide range of particle forms.

A1: Rain

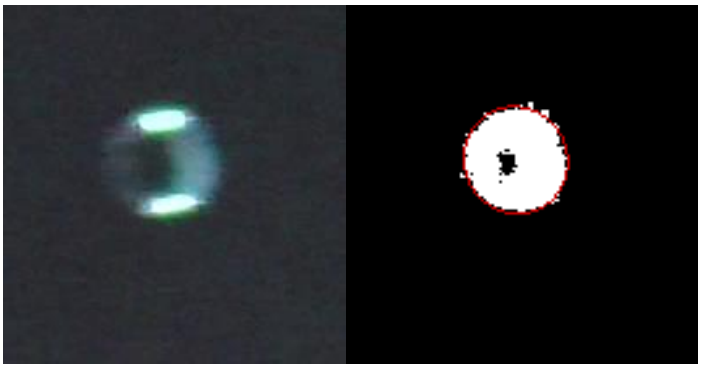

Figure A. 1. Rain drop, 29 May 2012. Diameter = 6.7 mm, Altitude = 363 m, Temperature = 30.7°C. Left raw image, right PA detection with fitted ellipse.

Figure A. 2. Rain drop, 29 May 2012. Diameter = 3.2 mm, Altitude = 384 m, Temperature = 30.6°C. Left raw image, right PA detection with fitted ellipse.

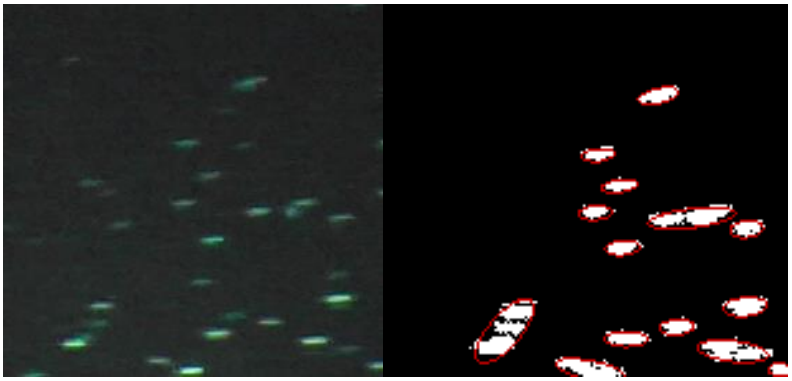

Figure A. 3. Rain drop, 29 May 2012. Diameter = various, Altitude = 391 m, Temperature = 30.5°C. Left raw image, right PA detection with fitted ellipse.

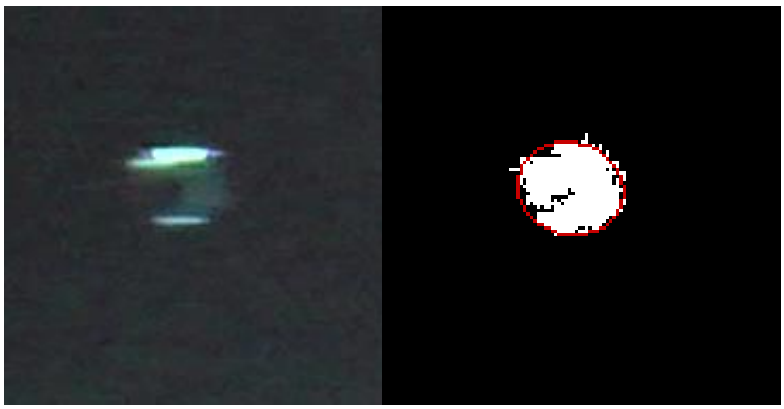

Figure A. 4. Rain drop, 29 May 2012. Diameter = 4.3 mm, Altitude = 1.8 km, Temperature = 19.4°C. Left raw image, right PA detection with fitted ellipse.

Figure A. 5. Rain drop, 29 May 2012. Diameter = 3.1 mm, Altitude = 1.8 km, Temperature = 19.4°C. Left raw image, right PA detection with fitted ellipse.

Figure A. 6. Rain drop, 29 May 2012. Diameter = 3.1 mm, Altitude = 1.8 km, Temperature = 19.1°C. Left raw image, right PA detection with fitted ellipse.

Figure A. 7. Rain drop, 29 May 2012. Diameter = 2.3 mm, Altitude = 2.1 km, Temperature = 17.1°C. Left raw image, right PA detection with fitted ellipse.

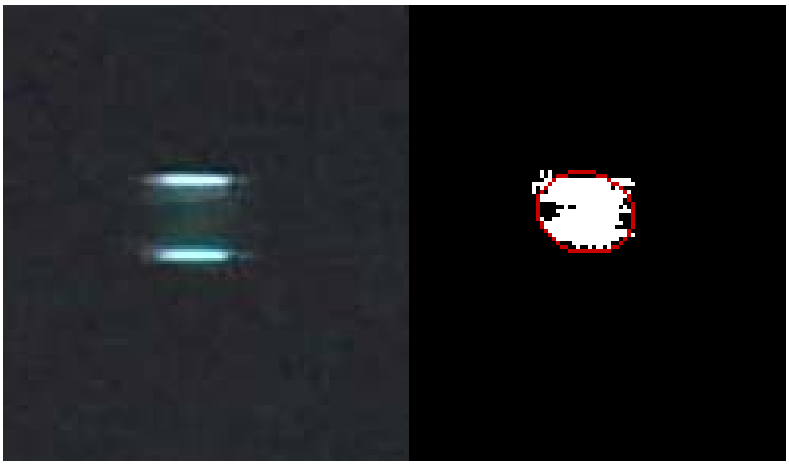

Figure A. 8. Rain drop, 29 May 2012. Diameter = 3.1 mm, Altitude = 2.2 km, Temperature = 16.2°C. Left raw image, right PA detection with fitted ellipse.

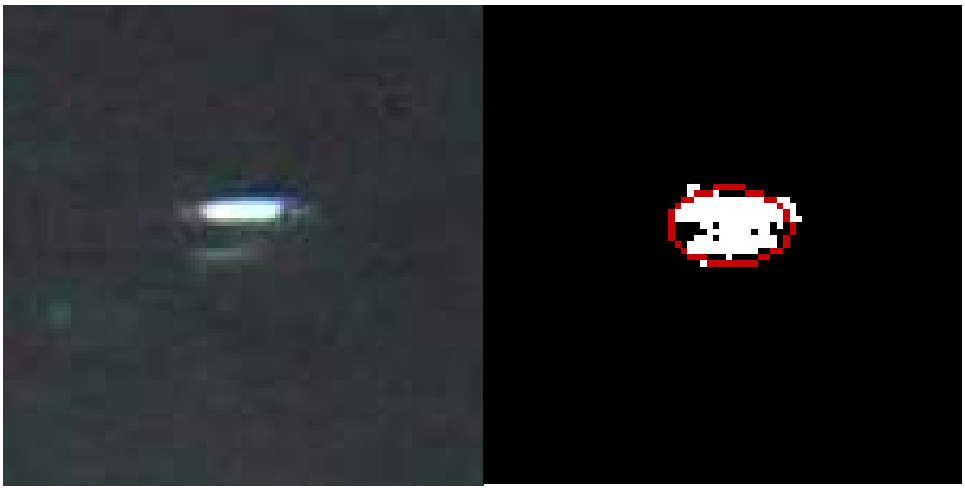

Figure A. 9. Rain drop, 29 May 2012. Diameter = 1.8 mm, Altitude = 2.2 km, Temperature = 16.1°C. Left raw image, right PA detection with fitted ellipse.

Figure A. 10. Rain drop, 29 May 2012. Diameter = 2.34 mm, Altitude = 2.6 km, Temperature = 14.1°C. Same image as Figure A. 16. Left raw image, right PA detection with fitted ellipse.

A2: Graupel/Hail

Figure A. 11. Melting graupel/hail, 29 May 2012. Diameter = 4.9 mm, Altitude = 2.0 km, Temperature = 17.9°C. Left raw image, right PA detection with fitted ellipse.

Figure A. 12. Melting graupel/hail, 29 May 2012. Diameter = 6.3 mm, Altitude = 2.2 km, Temperature = 16.4°C. Left raw image, right PA detection with fitted ellipse.

Figure A. 13. . Melting graupel/hail, 29 May 2012. Diameter = 4.6 mm, Altitude = 2.2 km, Temperature = 16.1°C. Left raw image, right PA detection with fitted ellipse.

Figure A. 14. Melting graupel/hail, 29 May 2012. Diameter = 4.5 mm, Altitude = 2.2 km, Temperature = 16.1°C. Left raw image, right PA detection with fitted ellipse.

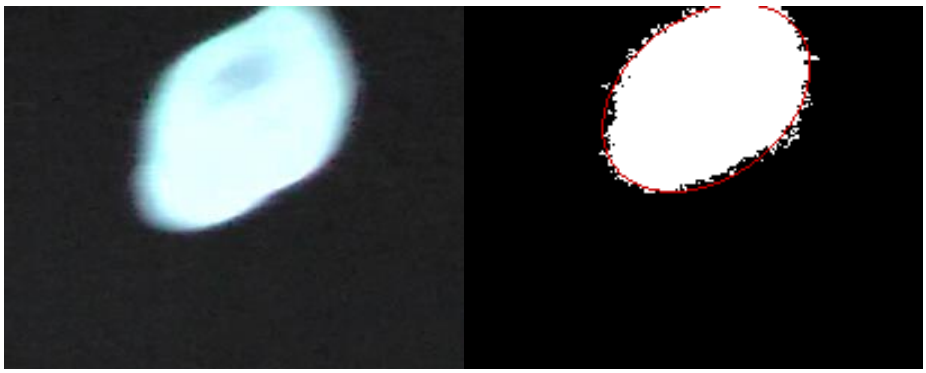

Figure A. 15. Melting hail, 29 May 2012. Diameter = 18.1 mm, Altitude = 2.3 km, Temperature = 15.5°C. Left raw image, right PA detection with fitted ellipse.

Figure A. 16. Melting graupel/hail, 29 May 2012. Diameter = 3.46 mm, Altitude = 2.6 km, Temperature = 14.1°C. Same image as Figure A. 10. Left raw image, right PA detection with fitted ellipse.

Figure A. 17. Melting graupel/hail, 29 May 2012. Diameter = 5.67 mm, Altitude = 3.8 km, Temperature = 4.6°C. Left raw image, right PA detection with fitted ellipse.

Figure A. 18. Conical graupel, 29 May 2012. Diameter = 4.5 mm, Altitude = 5.7 km, Temperature = -11.6°C. Left raw image, right PA detection with fitted ellipse.

Figure A. 19. Conical graupel, 29 May 2012. Diameter = 7.89 mm, Altitude = 5.8 km, Temperature = -12.1°C. Left raw image, right PA detection with fitted ellipse.

Figure A. 20. Conical graupel, 29 May 2012. Diameter = 5.56 mm, Altitude = 6.0 km, Temperature = -13.4°C. Left raw image, right PA detection with fitted ellipse.

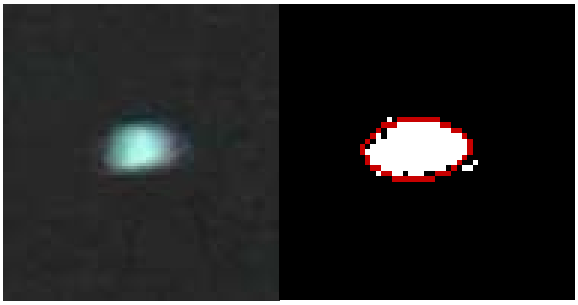

Figure A. 21 Conical graupel, 21 June 2012. Diameter = 1.75 mm, Altitude = 5.4 km, Temperature = -4.6°C. Left raw image, right PA detection with fitted ellipse.

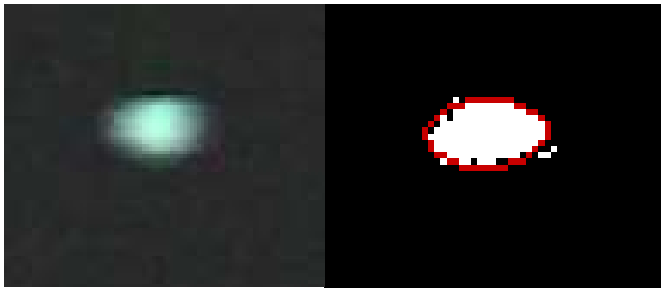

Figure A. 22 Conical graupel, 21 June 2012. Diameter = 1.82 mm, Altitude = 5.4 km, Temperature = -4.9°C. Left raw image, right PA detection with fitted ellipse.

A3: Irregular Ice Crystals

Figure A. 23 Irregular Ice Crystal, 29 May 2012. Diameter = 4.63 mm, Altitude = 6.7 km, Temperature = -20.5°C. Left raw image, right PA detection with fitted ellipse.

Figure A. 24. Irregular Ice Crystal, 21 June 2012. Diameter = 3.72 mm, Altitude = 7.6 km, Temperature = -17.4°C. Left raw image, right PA detection with fitted ellipse.

Figure A. 25 Irregular Ice Crystal, 21 June 2012. Diameter = 4.6 mm, Altitude = 7.6 km, Temperature = -17.4°C. Left raw image, right PA detection with fitted ellipse.

Figure A. 26 Irregular Ice Crystal, 21 June 2012. Diameter = 3.2 mm, Altitude = 8.7 km, Temperature = -24.2°C. Left raw image, right PA detection with fitted ellipse.

Figure A. 27 Irregular Ice Crystal, 29 May 2012. Diameter = 2.7 mm, Altitude = 6.5 km, Temperature = -18.5°C. Left raw image, right PA detection with fitted ellipse.

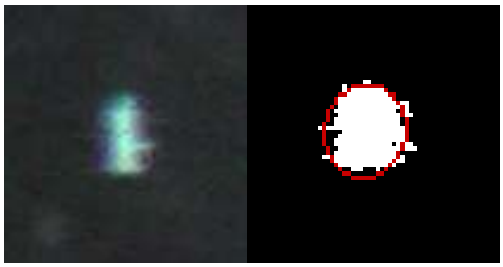

Figure A. 28 Irregular Ice Crystal, 29 May 2012. Diameter = 2.8 mm, Altitude = unknown, Temperature = unknown (radiosonde failure). Left raw image, right PA detection with fitted ellipse.

Figure A. 29 Irregular Ice Crystal, 29 May 2012. Diameter = 2.6 mm, Altitude = unknown, Temperature = unknown (radiosonde failure). Left raw image, right PA detection with fitted ellipse.

A4: Regular Ice Crystals

Figure A. 30 Regular Ice Crystals, 21 June 2012. Diameter = various, Altitude = 8.7 km, Temperature = -24.2°C. Left raw image, right PA detection with fitted ellipse. Full image shown.

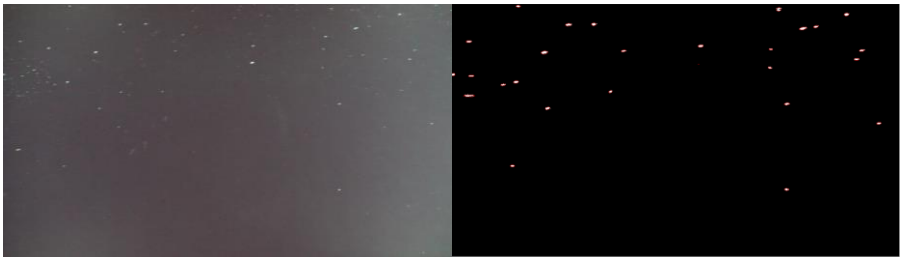

Figure A. 31 Regular Ice Crystals, 21 June 2012. Diameter = various, Altitude = 9.5 km, Temperature = -30.4°C. Left raw image, right PA detection with fitted ellipse. Full image shown.

Figure A. 32 Regular Ice Crystals, 29 May 2012. Diameter = various, Altitude = 6.6 km, Temperature = -19.3°C. Left raw image, right PA detection with fitted ellipse. Full image shown.

Figure A. 33 Regular Ice Crystals, 29 May 2012. Diameter = various, Altitude = unknown, Temperature = unknown (radiosonde failure). Left raw image, right PA detection with fitted ellipse. Full image shown.